Design of Catalyst Structure in Non-Precious Metal Catalysts for Anion Exchange Membrane Fuel Cells and Zinc-Air Batteries

음이온 교환막 연료전지와 아연-공기 전지를 위한 비귀금속 촉매의 구조 연구

2020 년 8 월

서울대학교 대학원

공과대학 화학생물공학부
에너지환경화학융합기술전공
김미주

Design of Catalyst Structure in Non-Precious Metal Catalysts for Anion Exchange Membrane Fuel Cells and Zinc-Air Batteries

음이온 교환막 연료전지와 아연−공기 전지를 위한

비귀금속 촉매의 구조 연구

지도 교수 성 영 은

이 논문을 공학박사 학위논문으로 제출함
2020 년 8 월

서울대학교 대학원
공과대학 화학생물공학부 에너지환경화학기술융합전공
김미주

김미주의 박사 학위논문을 인준함
2020 년 7 월

위 원 장	헌 태환	(인)
부위원장	성 영은	(인)
위 원	김 대형	(인)
위 원	박 원철	(인)
위 원	유 승호	(인)

Abstract

Design of catalyst structure in non-precious metal catalysts for anion exchange membrane fuel cells and zinc-air batteries

Mi-Ju Kim

School of Chemical and Biological Engineering Chemical

Convergence for Energy & Environment

The Graduate School

Seoul National University

Constraining the emission of carbon dioxide due to using fossil fuels promotes the development of clean energy devices including fuel cells and metal-air batteries. Electrochemical oxygen reduction reaction (ORR) is a critical reaction in the energy conversion and storage systems. However, the use of Pt-based catalysts, which is typically required for the sluggish ORR reaction, is undesirable due to their high cost, scarcity, and low sustainability. Hence, a significant amount of research has been dedicated to developing alternatives to Pt catalysts that exhibit high performance and are more economically viable. Non-precious metal based catalysts have captured attention for the viability and sustainability of the devices. Despite the rapid development in non-precious metal based catalysts, the gap between the performance in half-cells and single cells has hardly narrowed, which is a drawback for the mass production of energy devices. Therefore, this study was conducted for designing and synthesizing the efficient non-precious metal catalysts in both half-cell and single-

cell operations.

Chapter 1 introduces ORR and non-precious metal catalysts for ORR. Also, the electrochemical reactions and the advantages of the AEMFCs and ZABs are addressed.

In chapter 2, pore-controlled S, N co-doped carbons (SNBCs) are prepared as ORR electrocatalysts via pyrolysis of bamboo and thiourea. By achieving the controlled mesopore ratio and increased effective active sites, the SNBC presents superior half-wave potentials and stabilities, comparable to commercial Pt/C. As cathode materials for ZABs and AEMFCs, SNBC exhibits excellent performances higher than the reported carbon-based catalysts, based on the sufficient secondary pore structures. This study demonstrates the capability of applying the biomass-based catalysts into practical energy applications.

In chapter 3, Fe-N-C electrocatalysts with Fe coated with a carbon layer (Fe@C) and Fe-N_x site were prepared to control the Fe/C ratio using pyrosynthesis. Increasing carbon content increases the Fe-N_x site density and decreases the size of Fe nanoparticles and the thickness of the carbon coating layer, enhancing ORR activity. Moreover, Fe@C not only catalyze 4-electron ORR but also promotes ORR by stabilization and the reduction of the intermediate. Therefore, controlling the Fe@C/Fe-N_x ratio provides the optimum point that exhibits superior ORR activity. As cathode materials for AEMFCs and ZABs, the FeNC electrocatalysts exhibit excellent performance when compared to the platinum catalysts and the previously reported transition metal-based catalysts. The Fe-N_x site in catalysts proved to be the electrocatalytically efficient Fe-N_4 site from *in situ* XAFS analysis.

Keywords: Oxygen Reduction Reaction, Electrocatalysis, Non-Precious Metal Catalysts, Anion Exchange Membrane Fuel Cells, Zn-air Batteries

Student number: 2014-21584

Contents

List of Tables

Chapter 1

-

Chapter 2

Chapter 3

List of Figures

Chapter 1

Chapter 2

Chapter 3

Chapter 1. Introduction

1.1. Oxygen Reduction Reaction (ORR)

The ORR is one of the electrochemical reactions involved in energy devices including fuel cells and metal-air batteries.[1] The reaction is a pivotal reaction due to its sluggish rate that is the origin of the primary energy lost in the devices. The ORR involves multiple reaction steps including the adsorption/desorption of oxygen species, as shown in the following reaction pathways.[2]

\<Alkaline\>

$$O_2 + 2H_2O + 4e^- \rightarrow OOH^* + H_2O + OH^- + 3e^-$$

$$OOH^* + H_2O + OH^- + 3e^- \rightarrow O^* + H_2O + 2OH^- + 2e^-$$

$$O^* + H_2O + 2OH^- + 2e^- \rightarrow OH^* + 4OH^-$$

$$OH^* + 3OH^- + e^- \rightarrow 4OH^-$$

\<Acidic\>

$$O_2 + 4H^+ + 4e^- \rightarrow OOH^* + 3H^+ + 3e^-$$

$$OOH^* + 3H^+ + 3e^- \rightarrow O^* + H_2O + 2H^+ + 2e^-$$

$$O^* + H_2O + 2H^+ + 2e^- \rightarrow OH^* + H_2O + H^+ + e^-$$

$$OH^* + H_2O + H^+ + e^- \rightarrow 2H_2O$$
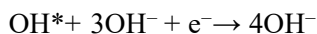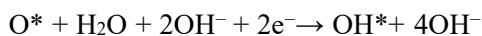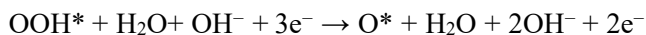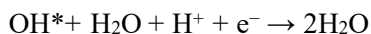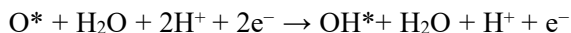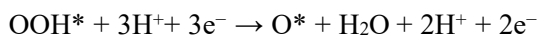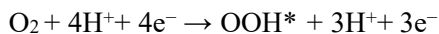
In order to increase the ORR rate, efficient catalysts are required to reduce the energy barrier called activation energy for ORR (Figure 1.1).[2] As shown in the above pathways, the adsorption/desorption of oxygen species are significantly involved in ORR. Therefore, the adsorption energy of oxygen species has been used for a descriptor of the ORR activity of the catalysts.[3] The adsorption of oxygen on

catalysts should be not too strong or too weak for facile activation and desorption, which is the Sabatier principle (Figure 1.2a).[4] Using the principle and density functional theory, Norskov et al. calculated the overpotential of ORR as a function of the OOH* and OH* adsorption energies (Figure 1.2b).[5] Since Pt is located near the peak of the volcano plot, Pt has been considered as the most active catalyst for ORR.

In the ORR kinetics, the relationship between overpotential and current is expressed by Butler-Volmer equation at equilibrium as follow:[6]

$$j = j_0 \left[\exp\left(\frac{\alpha n F \eta}{RT}\right) - \exp\left(-\frac{(1-\alpha)nF\eta}{RT}\right)\right]$$

where j is current, j_0 is the exchange current density at the equilibrium, α is the charge transfer coefficient, n is the electron transfer number, η is the overpotential.

The j_0 can be described by the following equation:[6]

$$j_0 = nF c_R^* f_1 \exp\left(-\frac{\Delta G_1^{\ddagger}}{RT}\right)$$

where c_R^* is the reactant concentration, f_1 is the decay rate to products, $\Delta G_1^{\ddagger}$ is the size of the energy barrier between the reactant and activated states.

The j_0 is aimed to be increased for improving the ORR activity. Increasing j_0 can be achieved by increasing the reactant concentration, decreasing the activation barrier, increasing the temperature, and increasing the number of effective active sites.[3,6]

2

<Alkaline>

Four-electron pathway: $O_2 + 2H_2O + 4e^- \rightarrow 4OH^-$ E^O (V vs SHE) = 0.401 V

Two-electron pathway: $O_2 + H_2O + 2e^- \rightarrow HO_2^- + OH^-$ E^O (V vs SHE) = −0.076 V

$\qquad\qquad\qquad$ $HO_2^- + H_2O + 2e^- \rightarrow 3OH^-$ E^O (V vs SHE) = 0.878 V

<Acidic>

Four-electron pathway: $O_2 + 4H^+ + 4e^- \rightarrow 2H_2O$ E^O (V vs SHE) = 1.229 V

Two-electron pathway: $O_2 + 2H^+ + 2e^- \rightarrow 2H_2O_2$ E^O (V vs SHE) = 0.695 V

$\qquad\qquad\qquad$ $H_2O_2 + 2H^+ + 2e^- \rightarrow 2H_2O$ E^O (V vs SHE) = 1.776 V
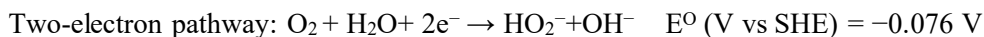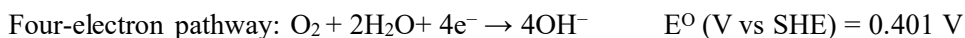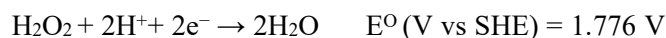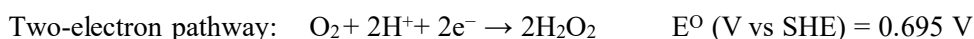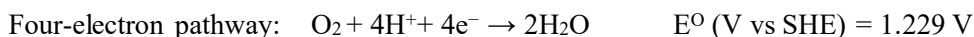
The ORR in an alkaline electrolyte exhibits thermodynamic advantages when compared to that in an acid medium. According to the reduction potentials of ORR in each electrolyte, the electrode potentials decrease from 1.229 V at an alkaline electrolyte to 0.401 V at an acidic electrolyte.[7] The potential shift affects the adsorption strengths of adsorbates and intermediates, which makes the ORR in an alkaline electrolyte easier. Moreover, the difference in pH affects the overpotential for the ORR (Figure 1.3).[8] The different ORR activity of Ag according to pH of electrolyte is explained by using the Nernst equation and the reduction potential of the first electron transfer reaction.[8] These effects enable the existence of ORR activity of various types of catalysts.
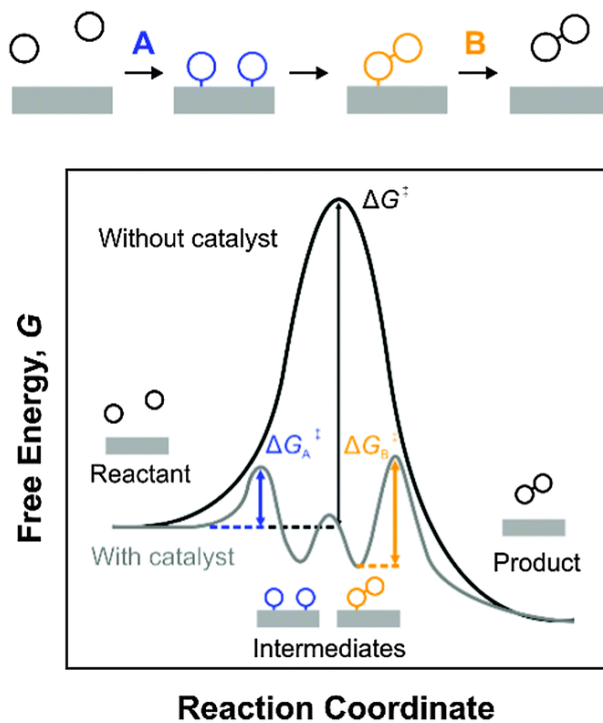
Figure 1.1 Schematic illustrations of a typical reaction mechanism associated with transition state and the role of catalyst. Adapted from reference [2].
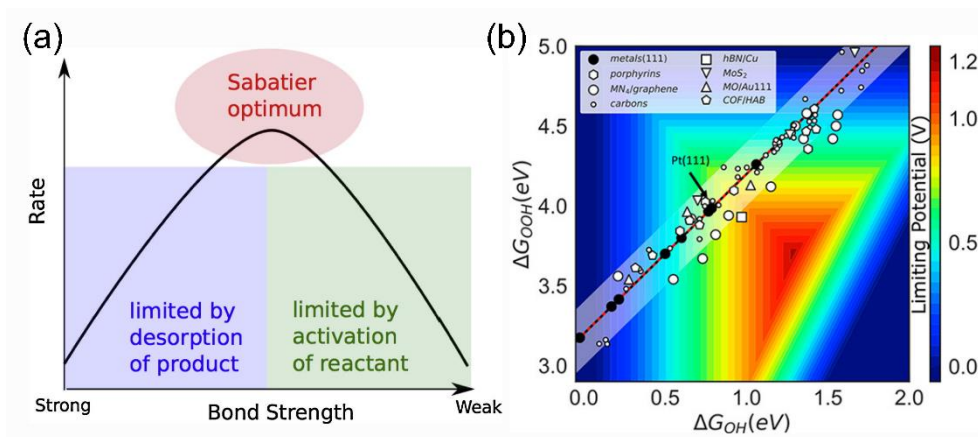
Figure 1.2 (a) Schematic illustration of the Sabatier principle. (b) 2-D volcano plot using the chemisorption energies of *OOH and *OH. Adapted from reference [4] and [5].
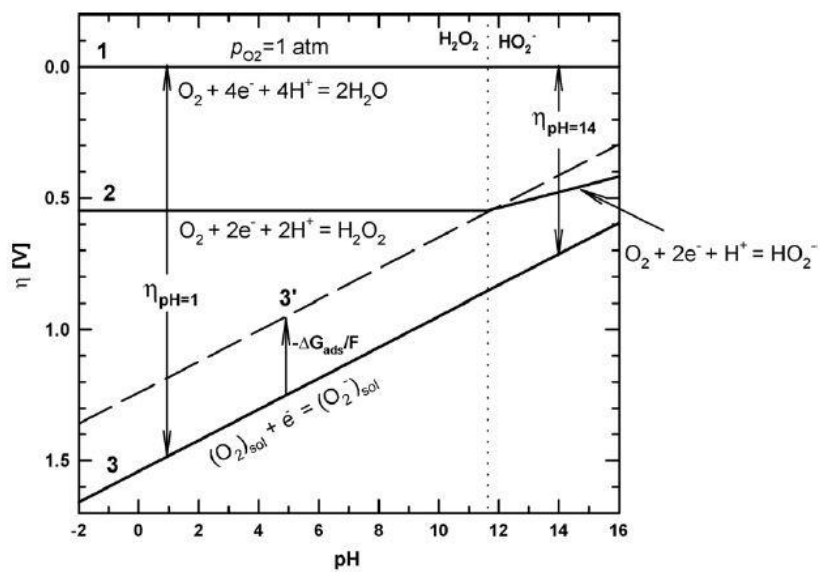
Figure 1.3 Modified form of Pourbaix diagram. Adapted from reference [8].

1.2. Non-Precious Metal ORR Catalysts

Pt-based catalysts have been known for their high catalytic activities and used in the commercialized fuel cell stacks.[5] However, as the scarcity and high cost of Pt reduce the sustainability and the availability of the devices, the non-precious metal catalysts have been extensively studied as the alternative of Pt catalysts. Recently, some non-precious metal catalysts show the excellent ORR activity that approaches that of platinum group metal catalysts.[1,7]

Heteroatom doping (N, B, S, etc.) into carbon is an effective way to tune electrical and catalytic properties due to the difference in electronegativity or spin density between carbon and heteroatom. It results in positively/negatively charged portion, which can reduce the oxygen molecules (Figure 1.4).[9] N atoms modulate the charge distribution in the carbon framework and also act as active sites since the electronegativity of N atom (3.04) and C atom (2.55) notably differ. The π electrons in C are activated through the conjugation with lone-pair electrons from N dopants, resulting in the reduction of O_2 molecules on the positively charged C atoms that neighbor N atoms.[10] Contrary to N, B dopant in the carbon lattice possesses positive charge due to its smaller electronegativity than C.[9] Apart from the electronegativity difference, S dopant in the carbon lattice increases the spin density of C, which induces the adsorption of oxygen.[11] Furthermore, co-doping strategies in which more than one type of heteroatom is incorporated can further enhance catalytic performance due to synergistic effects.[12] For instance, C atoms in the N, S co-doped carbon act as electrocatalytic active sites due to the synergistic effect of the different electronegativity of N and the different spin density of S compared to C.

The non-precious metal catalyst using transition metal, N, and C is considered as the most promising catalysts due to high activity and low cost.[13] Among various transition metal, Fe-based catalysts have exhibited excellent ORR performance when compared to other non-precious metal catalysts.[14] The synthetic

methods for Fe-based catalysts using impregnation, polymer, metal-containing complex, and metal-organic framework, arouse the controversy on the exact active site, since the annealing at high temperature, an essential process for efficient Fe-based catalysts, makes it difficult to control the generation of the specific active site.[15] The most suggested active sites are carbon-coated iron particles (Fe@C) and a single iron atom bonded with nitrogen (Fe-N$_x$).[14] As the use of single-atom catalysts has been spotlighted throughout the recent catalyst research, the synthesis and analysis methods for them have been rapidly developed.[16] The catalysts with Fe-N$_x$ synthesized through the current technology exhibit high performance in a half-cell ORR and a single-cell operation due to its 4-electron pathway mechanism.[17] Meanwhile, Fe@C, an active site that is easily synthesized by high-temperature annealing with a large amount of Fe, is also known for catalyzing ORR efficiently.[18]
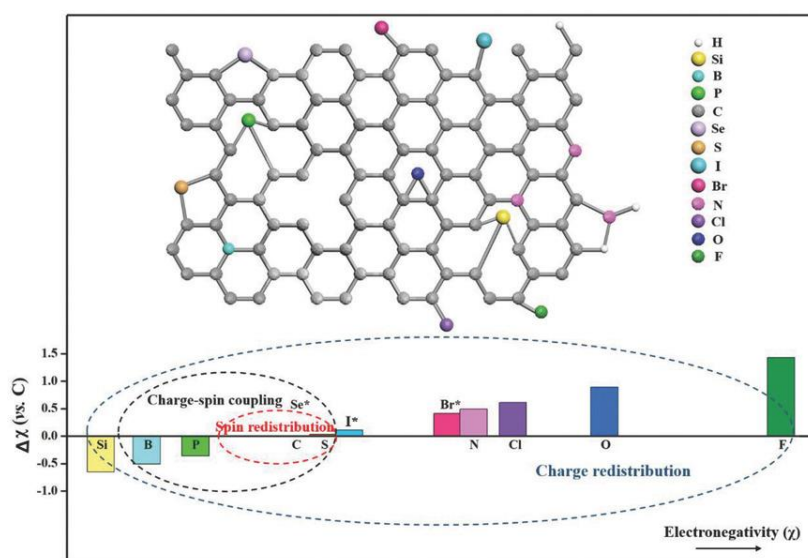
Figure 1.4 Illustration of heteroatom-doped carbon materials. Adapted from reference [9].

1.3.　Anion Exchange Membrane Fuel cells

Fuel cells are electrochemical devices that generate electricity from the chemical reaction using reactants with high-energy bonds and products with low-energy bonds. Fuel cells are sorted by their electrolyte: phosphoric fuel cells, solid oxide fuel cells, molten carbonate fuel cells, polymer electrolyte membrane fuel cells (PEMFCs), and anion exchange membrane fuel cells (AEMFCs).[6] AEMFCs, which employ an anion exchange polymer electrolyte membrane (AEM) (Figure 1.5), have been developed and focused recently due to the recent development of non-precious metal catalysts and anion exchange membrane.[19]

AEMFCs are associated with the following electrochemical reactions.[20] Contrary to PEMFCs where protons migrate from the anode to the cathode, OH^- is generated at the cathode and transmitted to the anode in AEMFCs. The electrons, produced at the anode, are moved to the cathode through the external circuit and used to produce electricity.

Anode:　　　　$H_2 + 2OH^- \rightarrow 2H_2O + 2e^-$　　　E^O (V vs RHE) = 0.000 V

Cathode:　　　$\frac{1}{2}O_2 + H_2O + 2e^- \rightarrow 2OH^-$　　　E^O (V vs RHE) = 1.229 V

Overall:　　　$\frac{1}{2}O_2 + H_2 \rightarrow H_2O$　　　　　　　E_{cell} (V vs RHE) = 1.299 V
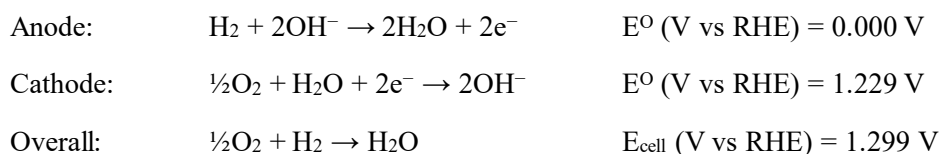
As mentioned, the theoretical open circuit voltage is 1.229 V in 293 K. The voltage output from the operation of single cells, however, is below the theoretical value due to overpotentials. Therefore, the improved cell performance can be obtained after overcoming the overpotentials including activation, ohmic, and concentration overpotentials (Figure 1.6). The activation overpotentials are related to reaction kinetics and intrinsic activity of the catalyst and a predominant factor in the low current density region. Moreover, ohmic overpotentials are related to electron and ion transport. The concentration overpotentials are influenced by the

mass transport of reactants and products to the catalytically active site, which is dominant in the high current density region.[6, 21]

AEMFCs have many advantages when compared to PEMFCs. At first, the reaction kinetics at the cathode in AEMFCs is notably faster than in PEMFCs. It enables the use of non-precious metal catalysts for cathode materials. For the cell components, the alkaline condition of AEMFCs is less corrosive than an acid electrolyte of PEMFCs, which allows for the use of various cell and stack materials. The membrane for AEMFCs can consist of lower-cost polymer than that for PEMFCs.[20, 22]

Despite the above advantages, AEMFCs still have drawbacks to be overcome for the commercialization, including low anionic conductivity and low stability of AEM, poisoning by CO_2, and hard water management.[20] Therefore, in addition to the development of a high conductive and durable AEM, the design of high-performance and low-cost catalyst is required to improve the performance of AEMFCs.[23] In specific, since the research on non-precious metal catalysts applied in the cathode of AEMFCs has just begun, the studies on efficient cathode materials for AEMFCs are still challenging.[22]
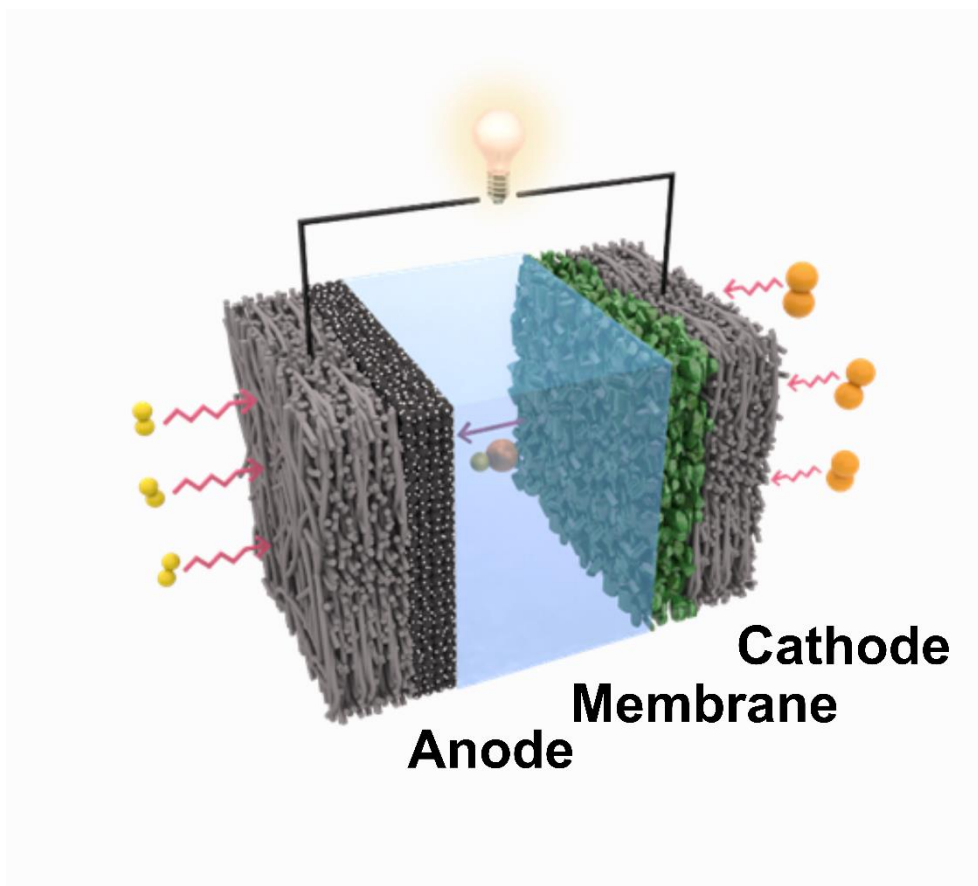
Figure 1.5 Schematic diagram of anion exchange membrane fuel cells (AEMFCs).
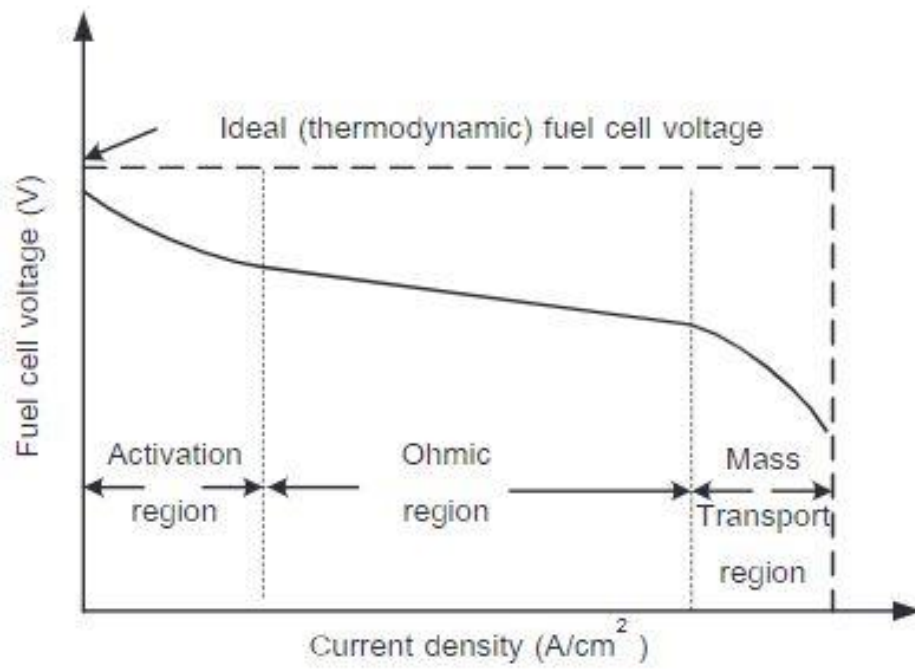
Figure 1.6 Typical I-V curve of fuel cells. Adapted from reference [24].

1.4. Zinc-Air Batteries

Zinc-air batteries (ZABs) with high specific energy (1218 Wh kg^{-1}) and volumetric energy density (6135 Wh L^{-1}) have focused recently as one of the next-generation battery technologies.[25, 26] The battery components are a negative zinc electrode, a positive air electrode, and an aqueous alkaline electrolyte (Figure 1.7). The air electrode in ZABs is similar to that of fuel cells and enables extremely high theoretical energy densities that are 2-10 times higher than those of lithium-ion batteries. Due to the configurations, ZABs are considered as a hybrid system of traditional batteries and fuel cells.[25] ZABs are sorted by their operation: a primary battery and a rechargeable (secondary) battery. A primary battery employs only discharge reaction, catalyzing ORR at air electrodes. In a rechargeable battery, the reverse electrochemical reactions occur at each electrode during charge reaction.[25]

A primary ZAB is associated with the following electrochemical reactions.[26] During discharge, OH^- is generated via ORR at the air electrode and transmitted to the zinc electrode. The electrons, produced at the zinc electrode, are moved to the air electrode through the external circuit and used to produce electricity.

Zinc electrode: $Zn + 4OH^- \rightarrow ZnO + H_2O + 2e^-$ E^O (V vs SHE) $= -1.26$ V

Air electrode: $O_2 + 2H_2O + 4e^- \rightarrow 4OH^-$ E^O (V vs SHE) $= 0.4$ V

Overall: $O_2 + 2Zn \rightarrow 2ZnO$ E_{cell} (V vs SHE) $= 1.66$ V
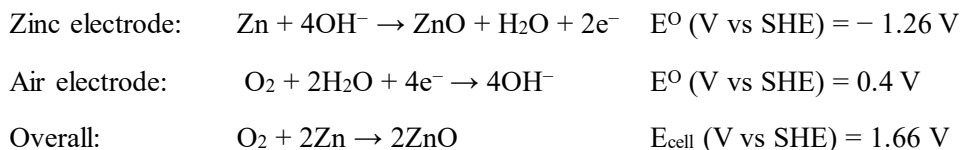
ZABs have many advantages when compared to conventional lithium-ion batteries (LIBs). Firstly, the cost-efficiency of ZABs (160-200 US$ kW h^{-1} at current levels and 70 US$ kW h^{-1} at estimated levels) is greater than that of LIBs (250 US$ kW h^{-1}).[27] Moreover, ZABs exhibits a theoretical energy density of 1086 Wh kg^{-1}, higher than the LIBs ($\approx$400 Wh kg^{-1}).[25-28] Therefore, ZABs is more suitable for long-distance operation of electric vehicles than LIBs (Figure 1.8a).[29] Regarding

safety, the zinc electrode with aqueous electrolyte lowers a fire danger, contrary to the metallic lithium electrode.

As the alternative of the LIBs, metal-air batteries with various metal anodes such as Li, Na, K, Zn, Mg, and Al have been researched. Li-air batteries using aprotic electrolytes have focused because of high theoretical energy density (5928 Wh kg^{-1}) and high cell voltage (2.96 V).[30] However, Li-air batteries cannot avoid the cost problem originated from Li metal. Moreover, when compared to other metals, Zn is suitable materials for low-cost, high-performance, and high safety metal-air batteries (Figure 1.8b).[31] Although Al-air and Mg-air batteries operated in an aqueous system like ZABs exhibits high theoretical capacities than LIBs, their low reduction potentials result in low energy densities.[26]

Despite the above advantages, ZABs still have drawbacks to be overcome for the commercialization, including slow kinetics of oxygen electrocatalysis, poisoning by CO_2, and non-uniform dissolution of the zinc electrode.[26] In specific, their low power output capability compared to high energy densities is originated from the insufficient performance of air electrodes.[25] Therefore, the design of high-performance and low-cost catalysts for oxygen electrolysis is required to improve the performance of ZABs. Moreover, since the non-precious metal catalysts suitable for the air electrode in ZABs can be applied for other metal-air batteries such as aluminum-air battery and magnesium-air batteries, the studies on efficient electrode materials for ZABs are of importance.[28]
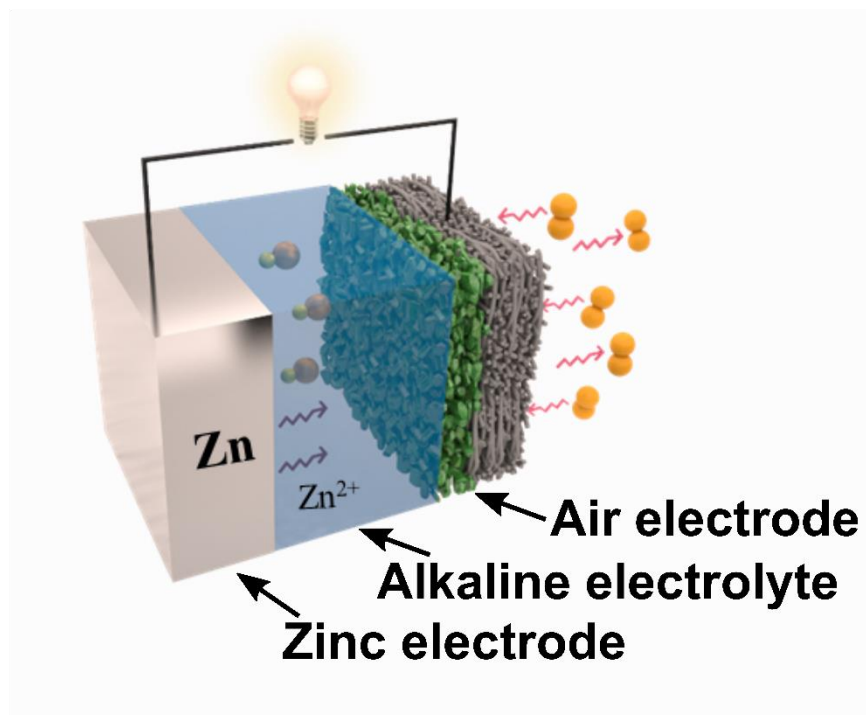
Figure 1.7 Schematic diagram of zinc-air batteries.
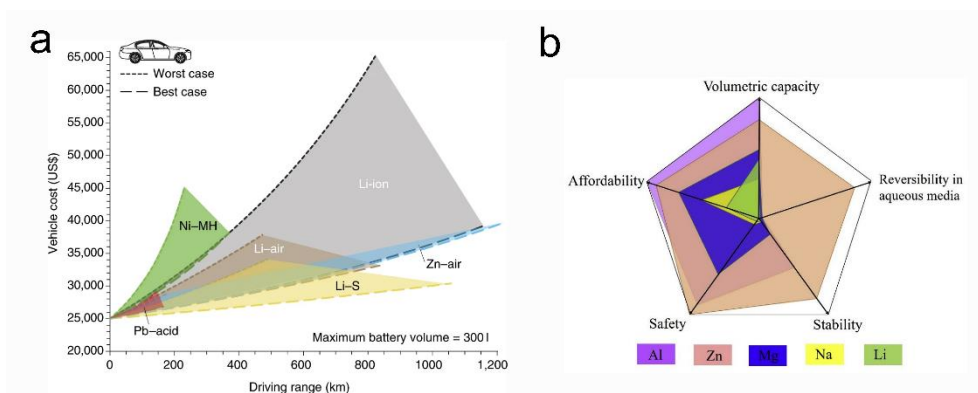
Figure 1.8 (a) Cost and driving distances of electric vehicles using several batteries Adapted from reference [29]. (b) Property regimes of metals that are anode materials in metal-air batteries. Adapted from reference [31].

1.5. Aim of this dissertation

This study was conducted with the goal of designing and synthesizing the efficient non-precious metal catalysts in both half-cell and single-cell operations. For preparing efficient catalysts in both operations, the difference of performance determining properties in the systems should be considered.

In half-cell systems, the three electrodes, working, counter, and reference electrodes are placed in an aqueous electrolyte. The catalysts are loaded onto the working electrode, which is a rotating-disk electrode (RDE). By using RDE, the continuous electrolyte flow and the corresponding mass transfer are induced. Therefore, in half-cell systems, the intrinsic activity of catalysts predominantly determines the ORR performance of the catalysts.

In fuel cells, as an example of single-cell systems, the three types of performance determining loss are known, as shown in chapter 1.3. The overpotentials dominant in the low current density region, the activation overpotentials, is correlated to the intrinsic activity of the catalyst, which can be evaluated by the half-cell test. To reduce the activation overpotentials, the intrinsic activity of catalysts can be enhanced by synthesizing active sites with high redox potential and turn-over frequency. The concentration overpotentials are associated with the performance in the high current density region and determined by the mass transport of reactants and products to the active sites. Contrary to half-cell systems, however, single-cell systems use a stationary electrolyte. Therefore, the design of pore structures within catalyst layers and in the catalysts is of importance to improve the mass transport in the catalyst layer.

In this study, two catalyst systems were designed as the ORR catalysts. For enhancing the ORR catalysts, two strategies are used in this dissertation: (i) increasing the number of active sites and (ii) increasing the intrinsic activity of

catalysts. Increasing the number of active sites is achieved by incorporating a sufficient amount of heteroatom or Fe in the catalysts. In addition, the intrinsic activity of the catalyst is increased by synthesizing the $Fe-N_4$ site with high intrinsic activity in part 4. These controlled catalyst structures were investigated using synchrotron-based analysis and advanced physicochemical and electrochemical techniques.

The catalyst systems were applied to the electrochemical devices, AEMFCs and ZABs. Figure 1.9 shows the comparison of ORR performance obtained in half-cell test and full-cell test (fuel cells) using state-of-art catalysts. Despite using the same catalyst, the enhanced catalytic activities of ORR electrocatalysts in half-cells are not reflected in those in real fuel cells (single-cells).[32] These phenomena are ascribed to the insufficient understanding of the complicated structure of single-cells and phenomena during operating single-cells. For the successful commercialization, the discrepancy between the catalytic activity in half-cells and single-cells should be reduced. Considering that the mass transport in the catalytic layer is a crucial factor determining the performance of single-cells, the catalyst structure favorable for mass transport is used (3D structure of Ketjen black in part 4) or developed (hierarchical pore structure of bamboo carbon in part 3).
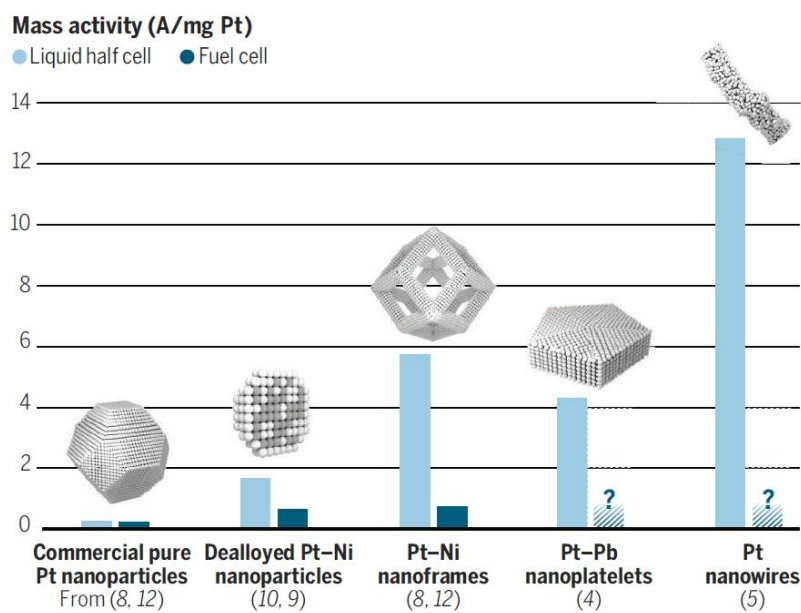
Figure 1.9 Comparison of ORR catalytic activity obtained at liquid electrolyte and practical device of various platinum-based catalysts. Adapted from reference [32].

1.6. References

1. Y. Nie, L. Li and Z. Wei, Recent advancements in Pt and Pt-free catalysts for oxygen reduction reaction, *Chem Soc Rev* 2015, **44**, 2168-2201.

2. W. T. Hong, M. Risch, K. A. Stoerzinger, A. Grimaud, J. Suntivich and Y. Shao-Horn, Toward the rational design of non-precious transition metal oxides for oxygen electrocatalysis, *Energy & Environmental Science* 2015, **8**, 1404-1427.

3. Z. W. Seh, J. Kibsgaard, C. F. Dickens, I. Chorkendorff, J. K. Norskov and T. F. Jaramillo, Combining theory and experiment in electrocatalysis: Insights into materials design, *Science* 2017, **355**.

4. A. J. Medford, A. Vojvodic, J. S. Hummelshøj, J. Voss, F. Abild-Pedersen, F. Studt, T. Bligaard, A. Nilsson and J. K. Nørskov, From the Sabatier principle to a predictive theory of transition-metal heterogeneous catalysis, *Journal of Catalysis* 2015, **328**, 36-42.

5. A. Kulkarni, S. Siahrostami, A. Patel and J. K. Norskov, Understanding Catalytic Activity Trends in the Oxygen Reduction Reaction, *Chem Rev* 2018, **118**, 2302-2312.

6. Ryan P. O'Hayre, Suk-won Cha, Whitney G. Colella and F. B. Prinz, Fuel Cell Fundamentals, Wiley, New York, 2008.

7. X. Ge, A. Sumboja, D. Wuu, T. An, B. Li, F. W. T. Goh, T. S. A. Hor, Y. Zong and Z. Liu, Oxygen Reduction in Alkaline Media: From Mechanisms to Recent Advances of Catalysts, *ACS Catal* 2015, **5**, 4643-4667.

8. B. B. Blizanac, P. N. Ross and N. M. Markovic, Oxygen electroreduction on Ag(111): The pH effect, *Electrochimica Acta* 2007, **52**, 2264-2271.

9.   K. Gao, B. Wang, L. Tao, B. V. Cunning, Z. Zhang, S. Wang, R. S. Ruoff and L. Qu, Efficient Metal-Free Electrocatalysts from N-Doped Carbon Nanomaterials: Mono-Doping and Co-Doping, *Adv Mater* 2019, **31**, e1805121.

10.   W. Ding, Z. Wei, S. Chen, X. Qi, T. Yang, J. Hu, D. Wang, L. J. Wan, S. F. Alvi and L. Li, Space-confinement-induced synthesis of pyridinic- and pyrrolic-nitrogen-doped graphene for the catalysis of oxygen reduction, *Angew Chem Int Ed Engl* 2013, **52**, 11755-11759.

11.   J. Zhang and L. Dai, Heteroatom-Doped Graphitic Carbon Catalysts for Efficient Electrocatalysis of Oxygen Reduction Reaction, *ACS Catal* 2015, **5**, 7244-7253.

12.   J. P. Paraknowitsch and A. Thomas, Doping carbons beyond nitrogen: an overview of advanced heteroatom doped carbons with boron, sulphur and phosphorus for energy applications, *Energy & Environ Sci* 2013, **6**, 2839.

13.   X. Tian, X. F. Lu, B. Y. Xia and X. W. Lou, Advanced Electrocatalysts for the Oxygen Reduction Reaction in Energy Conversion Technologies, *Joule* 2020, **4**, 45-68.

14.   U. Martinez, S. Komini Babu, E. F. Holby, H. T. Chung, X. Yin and P. Zelenay, Progress in the Development of Fe-Based PGM-Free Electrocatalysts for the Oxygen Reduction Reaction, *Adv Mater* 2019, **31**, e1806545.

15.   Q. Jia, N. Ramaswamy, U. Tylus, K. Strickland, J. Li, A. Serov, K. Artyushkova, P. Atanassov, J. Anibal, C. Gumeci, S. C. Barton, M.-T. Sougrati, F. Jaouen, B. Halevi and S. Mukerjee, Spectroscopic insights into

the nature of active sites in iron–nitrogen–carbon electrocatalysts for oxygen reduction in acid, *Nano Energy* 2016, **29**, 65-82.

16. H. T. Chung, D. A. Cullen, D. Higgins, B. T. Sneed, E. F. Holby, K. L. More and P. Zelenay, Direct atomic-level insight into the active sites of a high-performance PGM-free ORR catalyst, *Science* 2017, **357**, 479-484.

17. M. Chen, Y. He, J. S. Spendelow and G. Wu, Atomically Dispersed Metal Catalysts for Oxygen Reduction, *ACS Energy Letters* 2019, **4**, 1619-1633.

18. S. J. Kim, J. Mahmood, C. Kim, G. F. Han, S. W. Kim, S. M. Jung, G. Zhu, J. J. De Yoreo, G. Kim and J. B. Baek, Defect-Free Encapsulation of Fe(0) in 2D Fused Organic Networks as a Durable Oxygen Reduction Electrocatalyst, *J Am Chem Soc* 2018, **140**, 1737-1742.

19. S. Gottesfeld, D. R. Dekel, M. Page, C. Bae, Y. Yan, P. Zelenay and Y. S. Kim, Anion exchange membrane fuel cells: Current status and remaining challenges, *J. Power Sources* 2018, **375**, 170-184.

20. Y. J. Wang, J. Qiao, R. Baker and J. Zhang, Alkaline polymer electrolyte membranes for fuel cell applications, *Chem. Soc. Rev.* 2013, **42**, 5768-5787.

21. M. V. Williams, H. R. Kunz and J. M. Fenton, Analysis of Polarization Curves to Evaluate Polarization Sources in Hydrogen/Air PEM Fuel Cells, *J. Electrochem. Soc.* 2005, **152**, A635.

22. D. R. Dekel, Review of cell performance in anion exchange membrane fuel cells, *J. Power Sources* 2018, **375**, 158-169.

23. A. A. Gewirth, J. A. Varnell and A. M. DiAscro, Nonprecious Metal Catalysts for Oxygen Reduction in Heterogeneous Aqueous Systems, *Chem. Rev.* 2018, **118**, 2313-2339.

24.   W. Chanpeng and Y. Khunatorn, The effect of the input load current changed to a 1.2kW PEMFC performance, *Energy Procedia* 2011,**9**, 3 16-325.

25.   Y. Li and H. Dai, Recent advances in zinc-air batteries, *Chem Soc Rev* 2014, **43**, 5257-5275.

26.   J. Fu, Z. P. Cano, M. G. Park, A. Yu, M. Fowler and Z. Chen, Electrically Rechargeable Zinc-Air Batteries: Progress, Challenges, and Perspectives, *Adv Mater* 2017, **29**, 1604685.

27.   J. Fu, R. Liang, G. Liu, A. Yu, Z. Bai, L. Yang and Z. Chen, Recent Progress in Electrically Rechargeable Zinc-Air Batteries, *Adv Mater* 2019, **31**, e1805230.

28.   J. Mei, T. Liao, J. Liang, Y. Qiao, S. X. Dou and Z. Sun, Toward Promising Cathode Catalysts for Nonlithium Metal–Oxygen Batteries, *Advanced Energy Materials* 2019, **10**, 1901997.

29.   Z. P. Cano, D. Banham, S. Ye, A. Hintennach, J. Lu, M. Fowler and Z. Chen, Batteries and fuel cells for emerging electric vehicle markets, *Nature Energy* 2018, **3**, 279-289.

30.   P. Tan, B. Chen, H. Xu, H. Zhang, W. Cai, M. Ni, M. Liu and Z. Shao, Flexible Zn– and Li–air batteries: recent advances, challenges, and future perspectives, *Energy Environ. Sci.* 2017, **10**, 2056-2080.

31.   H. Li, L. Ma, C. Han, Z. Wang, Z. Liu, Z. Tang and C. Zhi, Advanced rechargeable zinc-based batteries: Recent progress and future perspectives, *Nano Energy* 2019, **62**, 550-587.

32.   I. E. L. Stephens, J. Rossmeisl and I. Chorkendorff, Toward sustainable fuel cells, *Science* 2016, **354**, 1378-1379

Chapter 2. Pore-Controlled S, N-Co-doped Carbon for Anion Exchange Membrane Fuel Cells and Zinc-Air Batteries

2.1. Introduction

Several strategies for tuning the properties of carbon-based catalysts in order to improve their ORR activities have been suggested.[1] Controlling the pore structures of ORR catalysts can change their surface areas and provide improved pathways for reactants and products, which are crucial for facilitating mass transport, thus enhancing catalytic performance. Furthermore, recent studies have shown that mass transport is promoted in materials with hierarchical pore structures, i.e., those comprising pores of different sizes.[2] Significant research effort has been focused on the micropores in hierarchical pore structures, which are typically the locations of the active sites. However, the mesopores therein have not received the level of research attention appropriate to their importance. Increasing the number of mesopores improves reactant and electrolyte accessibility to the active sites in the micropores and facilitates mass transport, enhancing ORR activity.[3]

Biomass materials are considered to be promising precursors for carbon-based catalysts as, considering their sustainability, low cost, and abundance, they avoid the economic problems associated with the large-scale production of precious-metal catalysts.[4] A diverse range of potential biomass materials has been applied to the production of carbon catalysts, including cattail,[5] seaweed,[6] pomelo peel,[7] egg,[8] cotton,[9] and mushroom.[10] However, many studies on biomass-based catalysts have

focused only on achieving certain catalytic activity rather than on finding scientific insight in them. Bamboo is a grass that is grown widely in Asia and South America. Furthermore, it grows very rapidly, resulting in its easy availability and low cost.[11] Moreover, charcoal from bamboo is already utilized in pollutant adsorbents due to its well-developed porous structure and high electrical conductivity.[12] Thus, the qualities of bamboo make it an appropriate biomass material on which to base ORR catalysts.

Herein, we present a green approach to the production of promising biomass-based ORR electrocatalysts. Specifically, bamboo stems are activated with steam under high temperatures (steam activation), which is an eco-friendly process when compared to previous activation methods using hazardous or unsustainable agents including ammonia and carbon dioxide. Subsequent doping with thiourea not only incorporates S and N into the carbon structure but also modifies the pore structure of the bamboo-based carbon. Thus, this strategy transforms bamboo into efficient carbon-based ORR electrocatalysts. This is evidenced by their high half-wave potentials, which are comparable to those of commercial Pt/C catalysts. Furthermore, this is achieved without the addition of metals. In the current study, the bamboo-based catalysts are applied to Zn-air batteries and anion exchange membrane fuel cells (AEMFCs), which are based on alkaline media. This is the first report of biomass-based catalysts being applied in the cathodes of AEMFCs. In both devices, the S, N co-doped bamboo-based carbon catalysts (SNBCs) exhibits performances that are higher than those of previously reported carbon-based catalysts and comparable to that of Pt/C catalysts. Thus, we successfully demonstrate the viability of applying biomass-based catalysts to practical devices.

2.2. Experimental section

2.2.1. Preparation of SNBCs

The bamboo stems were collected on a hill in South Korea. The collected stems were cut into small pieces less than 1.5 mm in length with a knife mill. The carbonization process was conducted under continuous N_2 flow at 200 cm^3 STP min^{-1} and maintained at 600 °C for 2 h with a heating rate of 10 °C min^{-1}. The carbonized bamboo stems were activated with steam at a flow rate of 2 mL-H_2O g-$char^{-1}$ h^{-1} with an N_2 flow of 300 cm^3 STP min^{-1}. The activated carbon was pulverized and mixed with thiourea (Sigma-Aldrich Chem. Co., USA) at different ratios using a PULVERISETTE7 high-energy ball mill (Fritsch, Germany). The mixed powder was pyrolyzed at different temperatures (700, 800, or 900 °C) for 1 h at a heating rate of 5 °C min^{-1} under an Ar atmosphere.

2.2.2. Physical characterization of SNBCs

The morphologies of the SNBCs were observed using a field-emission scanning electron microscope (FE-SEM; SUPRA 55VP, Carl Zeiss, Germany). The transmission electron microscopy (TEM) and scanning TEM energy-dispersive X-ray spectroscopy (STEM-EDS) images were acquired using a JEM-2100F (JEOL Ltd., Japan) at an operation voltage of 200 kV. X-ray diffraction (XRD) spectra were obtained using an X-ray diffractometer (D/MAX-2500/PC, Rigaku Co., Japan) with a Cu Kα (λ = 0.15418 nm) source. The elemental composition of the SNBCs was evaluated using X-ray photon spectroscopy (XPS, K-alpha, SIGMA PROBE, Thermo Fisher Scientific, UK) and photoemission spectroscopy at the 8A1 beamline in the Pohang Accelerator Laboratory (Pohang, Republic of Korea). The N_2 sorption isotherms of the catalysts were measured using a Brunauer–Emmett–Teller (BET) surface area analyzer (3Flex, Micromeritics, USA). The Raman spectra of the prepared catalysts were obtained with a Raman spectrometer (LabRAM HV

Evolution, Horiba, Japan) using a 532 nm laser. To ascertain the S and N contents of the catalysts, an elemental analyzer (Flash1112, Thermo Fisher Scientific, Germany) installed at the National Center for Inter-university Research Facilities (NCIRF) at Seoul National University was used. The pore distribution of the catalyst layers was measured using a mercury porosimeter (PM33GT, Quantachrome Co., USA).

2.2.3. Electrochemical characterization

The half-cell experiments were conducted with an Autolab potentiostat using a three-electrode cell in 0.1 M KOH and 0.1 M HClO$_4$ solution. We used potassium hydroxide (semiconductor grade, 99.99% trace metals basis, Sigma-Aldrich) and deionized water (18.2 mΩ·cm) to prepare the alkaline electrolyte. Before experiments, we cleaned the electrochemical cell components by using a nitric acid solution and deionized water. A glassy carbon electrode and a 3.5 M Ag/AgCl electrode were used as the counter and reference electrodes, respectively. The glassy carbon electrode was polished with alumina to a mirror finish. The potentials were converted to those for a reversible hydrogen electrode (RHE) using the hydrogen oxidation reaction. For linear scan voltammetry of the ORR, the electrode was rotated at 1600 rpm and scanned at 10 mV s^{-1} with *iR*-correction using impedance measurements. The results of the rotating ring-disk electrode (RRDE) studies were calculated using a collection efficiency of 0.37 to obtain the electron transfer numbers. We conducted long-term stability tests by chronoamperometry at 0.7 V versus RHE.

2.2.4. Fabrication and single-cell test of AEMFCs

The membrane electrode assembly (MEA) was fabricated using a catalyst-coated membrane (CCM) method. The anion exchange membrane used in this study was Fumapem FAA-3-50 (FuMA-Tech Inc., Germany). The membrane was

pretreated with 1.0 M KOH solution for 1 h to exchange Br ions to OH ions. The anode catalyst was 60 wt% Pt/C (Johnson Matthey Co., UK) with a loading of 0.5 mg_{Pt} cm^{-2}. The SNBC11, SNBC12, SNBC13, 20 wt% Pt/C (Johnson Matthey Co., UK), and 20 wt% Ag/C were used as the cathode catalyst. The loading of SNBCs, 20 wt% Pt/C, and 20 wt% Ag/C was 2.0 $mg_{SNBC, Pt\ or\ Ag}$ cm^{-2}. The catalyst ink was prepared with the catalyst, Fumion ionomer (FAA-3-Br, FuMA-Tech Inc., Germany), isopropyl alcohol, and deionized water. The content of Fumion ionomer was 20 wt%. The ink was sprayed onto both sides of the membrane. After its fabrication, the MEA was immersed in 1.0 M KOH solution for 30 min in order to exchange Cl ions in Fumion ionomer to OH ions and distilled water for 20 s. JNTG-A3-30 (JNTG, Korea) was used as a gas diffusion layer. The single-cell test of AEMFC was conducted under the H_2/O_2 condition at 60 °C. The relative humidity of anode and cathode was 80 and 90%, respectively. The flow rates of H_2 and O_2 were 800 and 1000 ml min^{-1}, respectively. The active area was 5 cm^2.

2.2.5. Fabrication and single-cell test of primary Zn-air battery

A home-made Zn-air single cell was constructed to evaluate the Zn-air battery test.[13] The Zn plate with a thickness of 250 μm (Alfa aesar Co. USA) was used as an anode. The air electrode using SNBC and 40 wt% Pt/C were prepared using the catalyst-coated substrate (CCS) method. The ink was prepared with the catalyst, Nafion ionomer (Aldrich Chem. Co., USA), isopropyl alcohol, and deionized water. The prepared ink was sprayed onto the gas diffusion layer (JNTG-A3-30 (JNTG, Korea)). The catalyst loading of SNBCs and Pt black was 4.0 mg cm^{-2}. 6 M KOH aqueous solution was used as the alkaline electrolyte.

Single-cell test of the primary Zn-air battery was carried out using two methods; current sweep method and constant current method. The cell temperature was 25 °C. Using the current sweep method, two polarization curves were obtained

to compare the power density of the Zn-air battery. Also, the specific density and energy density were measured by using the constant current method at 20 mA cm^{-2}. The electrochemical impedance spectra data (IM-6, ZAHNER-elektrik GmbH & Co. KG, Germany) were obtained at a constant voltage of 1.1 V to characterize the ohmic and charge transfer resistance of two catalysts. The frequency ranged from 100 mHz to 100 kHz during the measurement.

2.3. Results and Discussion

2.3.1. Synthesis and physical characterization of SNBC

Figure 2.1 summarizes the synthesis of SNBC. Activated bamboo-derived carbon (BC) is prepared by pyrolyzing carbonized bamboo stems in steam flow, resulting in the formation of a pore structure. High-energy ball milling crushes the BC into a microscale powder, which increases the surface area of the carbon and produces particles of various sizes, providing efficient mass transport pathways. Then, doping is performed to increase the number of active sites by pyrolysis of the BC mixed with thiourea, a source of S and N. Different S, N co-doped carbon materials are produced by controlling the BC/thiourea ratio. The different materials produced are labeled SNBCab, where 'ab' represents the BC/thiourea ratio, i.e., a/b. Through these procedures, the bamboo stems are transformed into green, high-performance electrocatalysts based on (i) the efficient mass transport endowed by their pore structures, and (ii) the increased number of active sites attributed to the S and N co-doping.

Figure 2.2a shows an SEM image of SNBC12. The particles have an irregular shape and are several micrometers in size, which is similar to the morphology of BC (Figure 2.3a–b). TEM images confirm the pore structure of SNBC12 (Figure 2.2b–c). It has nanometer-sized pores on the surface, indicating an abundance of micro/mesopores. STEM-EDS was used for elemental analysis of the catalysts (Figure 2.2d–f). S and N are uniformly distributed on the basal carbon structure of SNBC12. This is in contrast with the EDS results for bare bamboo-derived carbon, which comprises carbon and a trace amount of oxygen (Figure 2.3c–e).

The catalysts were investigated using XPS to ascertain the concentrations and chemical statuses of the elements and confirm the existence of electrocatalytically active sites (Figure 2.4). The XPS survey scans present several elements dominant in the SNBCs, including C, N, O, and S. Since the levels of S detected in the samples

31

Figure 2.1 Preparation and application of SNBC.
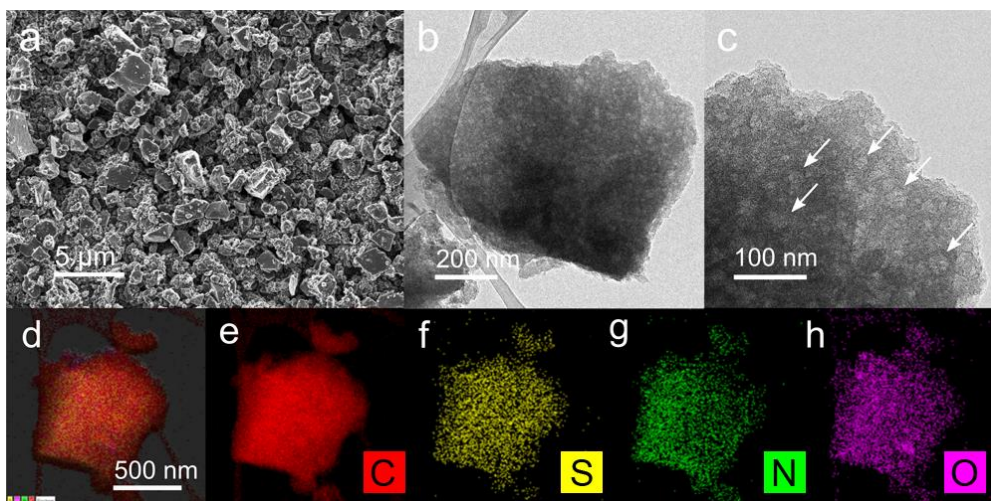
Figure 2.2 Morphology of SNBC12. (a) SEM image. (b, c) TEM images. EDS mapping images of (d) merged, (e) C, (f) S, (g) N, and (h) O elements.
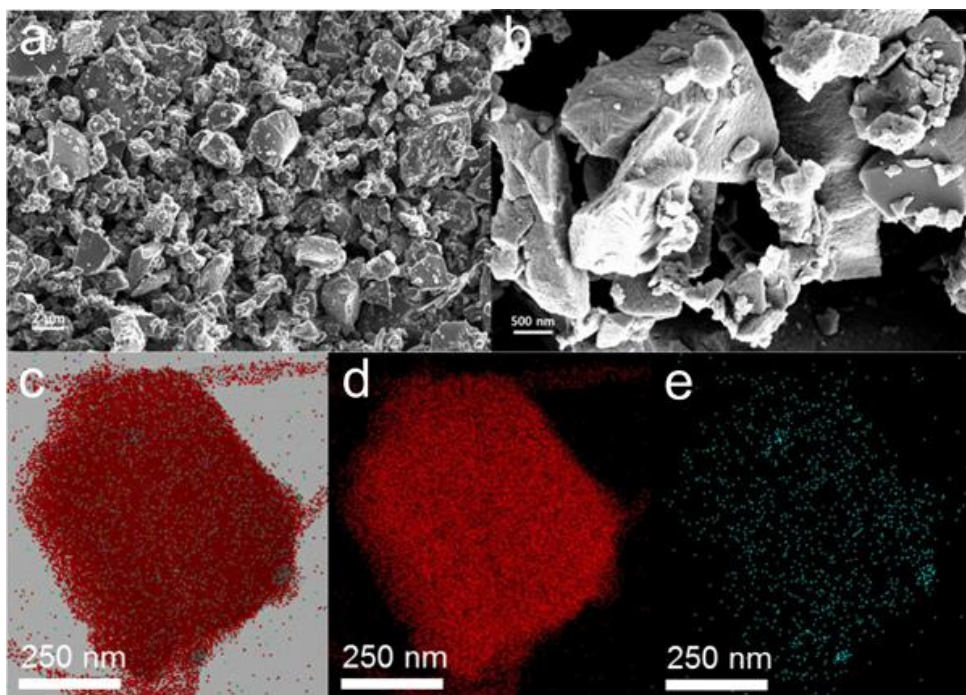
Figure 2.3 Morphology of BC. (a-b) SEM image. EDS mapping images of (c) the merged, (d) C, (e) O elements.
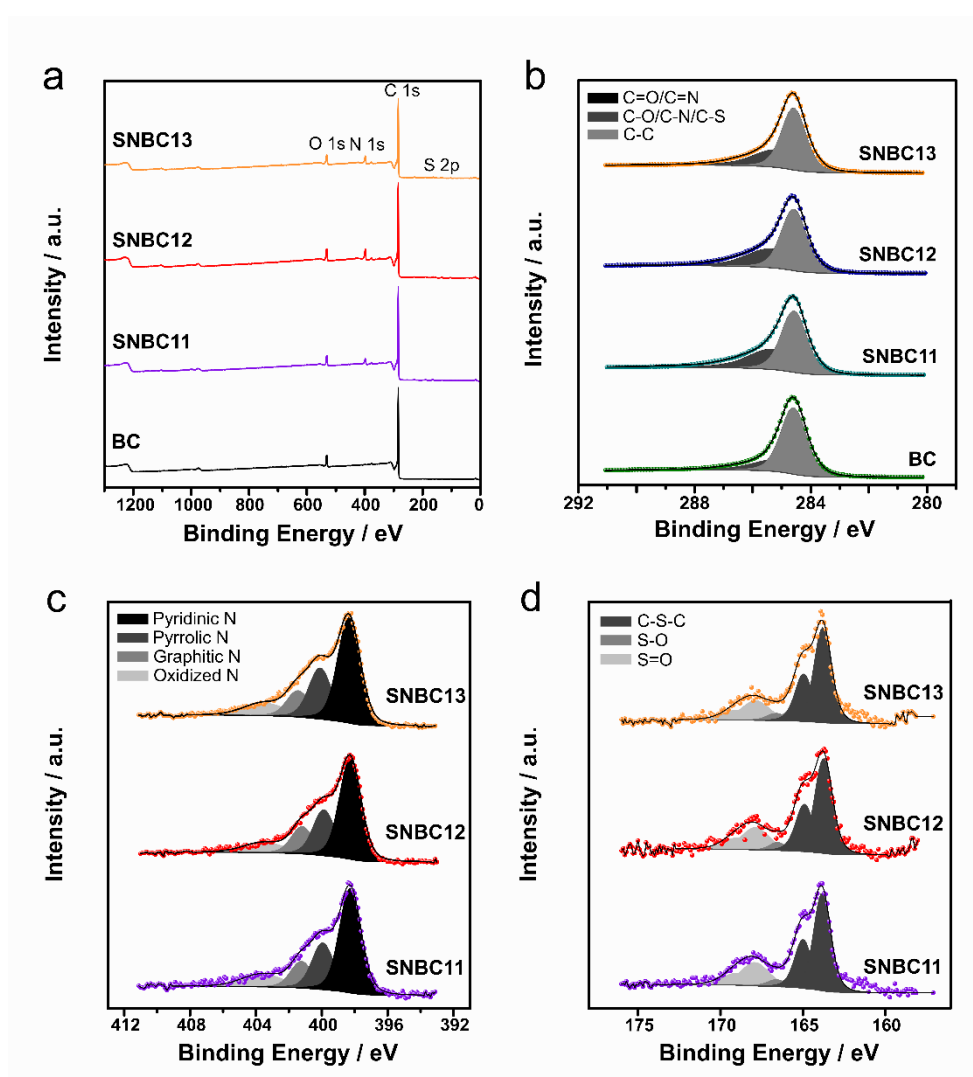
Figure 2.4 (a) Survey, (b) C 1s, (c) N 1s, and (d) S 2p XPS spectra of the SNBCs.

are low (0.71–1.14 at%), the corresponding peaks in the survey scans are small. With an increase in thiourea doping, the S and N contents increase, as shown by the elemental analysis results (Table 2.1). SNBC13 has the highest N content at 5.39 at%, while SNBC11 and SNBC12 have N contents of 3.49 and a 5.33 at%, respectively. The S content is slightly increased from 0.71 at% for SNBC11 to 1.14 at% for SNBC13. Because thiourea contains more N than S, the N contents of the materials are higher than those of S. Trace amounts of K (less than 0.6 at%) are also detected in all of the samples (at 284 eV in the survey scans) because it is a constituent of the plant cells in bamboo trees.[14] During the doping process, the heteroatom dopant creates bonds with the carbon after breaking sp^2 C-C bonds. Therefore, we investigated the C 1s spectra (Figure 2.4b) to confirm whether the doping process was successful. We deconvoluted the C 1s spectra into three bonding configurations; C-C (284.6 eV), C-O/C-N/C-S (285.1-285.3 eV), and C=O/C=N (286.7-287 eV).[15] Upon doping, the sp^2 C-C bond content is reduced from 70.09 at% for BC to 56.55 at% for SNBC13. Concurrently, the intensities of the other peaks derived from dopant incorporation increase. The increase in the peak intensity related to C-O/C-N/C-S is particularly notable, indicating that mainly single bonds with carbon are generated during doping.

The N bonding components were also thoroughly explored via the N 1s spectra, allowing us to consider the types of bonds that affect the catalytic activity. Since an increased doping amount does not lead to more active N species, identifying the appropriate amount of dopant source is essential for improved catalytic properties. The N 1s spectra can be used to distinguish four N configurations (Figure 2.4c). The peak at 398.3 eV corresponds to pyridinic N, and the peak at 400 eV is related to pyrrolic species. Graphitic N results in the peak at 401.3 eV, and the broad peak at 403.5 eV represents oxidized N.[16] The N contents of the SNBCs are dominated by pyridinic N (51–51.85 at%), followed by pyrrolic N (23.08–24.80 at%), graphitic N

Table 2.1 Elemental contents of BC and SNBCs from elemental analysis.

Sample	Carbon	Nitrogen	Sulfur	Oxygen
BC	86.5434	n.d.	n.d.	2.5491
SNBC11	80.6231	3.9183	1.6096	2.9331
SNBC12	79.3071	6.3258	1.2626	3.3352
SNBC13	80.6894	6.0962	1.6867	3.2179

(12.82–14.14 at%), and oxidized N (10.18–12.22 at%) (Table 2.2). With the increase in doping from SNBC11 to SNBC12, the pyridinic and graphitic N contents increase while the oxidized N content decreases. Compared to SNBC12, however, SNBC13 contains less pyridinic and graphitic N. Instead, the pyrrolic N content gradually increases when the amount of doping precursors increases from 23.08 at% for SNBC11 to 24.80 at% for SNBC13. Since the pyridinic and graphitic N are known to be the electrocatalytically active sites,[17,18] improved catalytic activity for SNBC12 is predicted. The high-resolution S 2p spectra showed six contributions, i.e., peaks for C-S-C at 163.7 eV and 164.9 eV, peaks for S-O at 165.4 eV and 166.6 eV, and peaks for S=O at 167.9 eV and 196 eV (Figure 2.4d).[19] The successful S doping leads to the largest peak for the bonding between S and C (Table 2.2). Moreover, when the amount of doping source is increased, the percentage of C-S-C is increased while the bonding between S and O is decreased.

The XRD of the samples (Figure 2.5a) confirms the graphitization of the prepared carbon materials. The peaks at 23° and 44° are indexed to the (002) and (101) planes of graphitic carbon (JCPDS 75-2078). Raman spectroscopy reveals peaks at 1330-1350 cm^{-1} (D band) and 1590-1600 cm^{-1} (G band), which are typical characteristics of carbon materials (Figure 2.5b).[20] The G band is associated with the degree of graphitization based on sp^2 C-C bonding, while the D band correlates with structural disorder and defects. Doping carbon materials with heteroatoms can enhance their structural disorder and thus increases the intensity of the D band.[21] Therefore, the I_D/I_G values of doped samples are higher than that of bare carbon samples, as previously reported in papers on S, N-doped carbon materials.[22,23]

Nitrogen sorption isotherms were obtained to assess the pore structures of the samples. The samples present typical type-IV isotherm curves (Figure 2.6a). The rapid increase at $P/P_O > 0.9$ indicates the development of secondary pores in the SNBCs.[24] The isotherm for BC determines a relatively high BET surface area (753.4

Table 2.2 Atomic ratio of N and S configurations of BC and SNBC materials from XPS analysis.

Nitrogen	Pyrrolic N	Pyridinic N	Graphitic N	Oxidized N
SNBC11	22.9	51.32	13.44	12.33
SNBC12	22.84	50.69	14.93	11.54
SNBC13	22.94	49.38	14.01	13.67
Sulfur	C-S-C	S-O		S=O
SNBC11	64.4	10.1		25.3
SNBC12	65.8	10.2		24
SNBC13	67.0	11.0		22.0
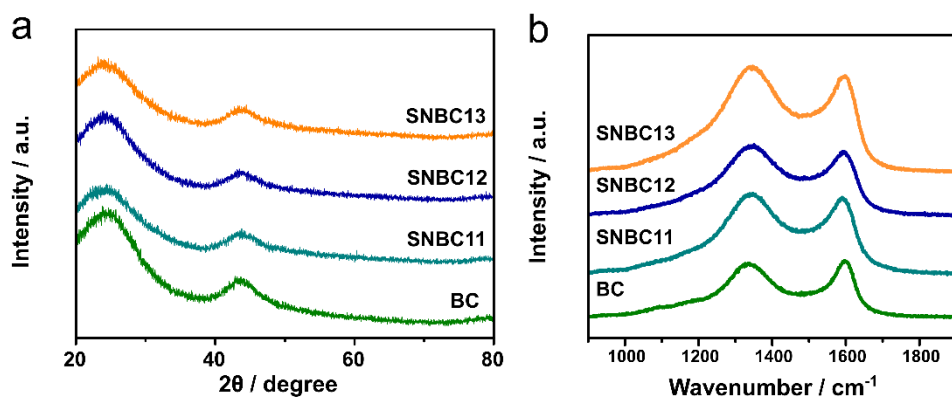
Figure 2.5 (a) XRD and (b) Raman spectra of BC and SNBCs.
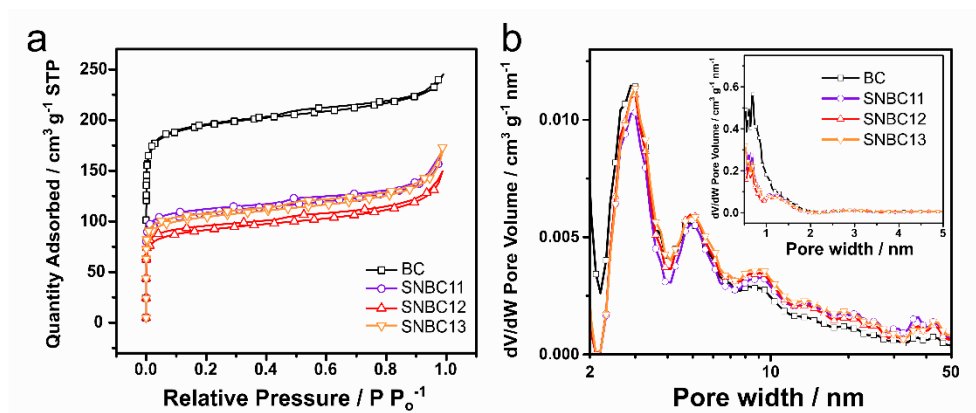
Figure 2.6 (a) N$_2$ adsorption/desorption isotherms and (b) pore size distributions based on NLDFT calculation.

$m^2\ g^{-1}$). For the SNBC samples, the BET surface areas and volumes are decreased through the doping process (Table 2.3). Figure 2.6b shows the pore-size distributions derived using non-local density functional theory (NLDFT) models. The volume of the micropores, where a micropore is defined as a pore with a diameter less than 2 nm, in SNBCs reduces as a result of doping with thiourea.[25] Doping heteroatoms using thiourea causes the collapse and coalescence of micropores, increasing the mesopore (pore size between 2–50 nm) volume of the SNBCs. SNBC12 shows the highest mesopore volume to micro/mesopore volume ratio (39.9%) as compared to 20.5% for BC (Table 2.3). Therefore, doping with thiourea controls the ratio of micro- to mesoporosity, enabling effective mass transport through the hierarchical pore structure.

2.3.2. Electrochemical characterization of SNBC

The electrochemical catalytic activities of the SNBCs were evaluated in a 0.1 M KOH electrolyte using an RDE in a three-electrode cell. As shown in Figure 2.7, BC exhibits a relatively low limiting current. However, the SNBCs show notably enhanced performances, i.e., increased limiting currents and half-wave potentials. The half-wave potentials for SNBC11 and SNBC13 are 0.79 V and 0.81 V, with the limiting currents of -3.85 mA cm^{-2} and -3.49 mA cm^{-2}, respectively. In particular, SNBC12 displays an extremely high half-wave potential (0.85 V), which is similar to those of commercial Pt/C catalysts (Figure 2.8) and unprecedented for biomass-based ORR catalysts and even carbon-based catalysts (Table 2.4 and 2.5). Furthermore, the limiting current for SNBC12 is the highest (-4.14 mA cm^{-2}), as compared to -3.85 mA cm^{-2} for SNBC11 and -3.49 mA cm^{-2} for SNBC13. The kinetic current density at 0.85 V for SNBC12 is also the highest (-3.68 mA cm^{-2}), as compared to -0.186 mA cm^{-2} for SNBC11 and -0.301 mA cm^{-2} for SNBC13. The

Table 2.3 Pore structure properties from BET analysis using non-local density functional theory (NLDFT) models of BC and SNBCs.

Sample	BC	SNBC11	SNBC12	SNBC13
BET surface area (m^2 g^{-1})	753.4	416.8	349.1	405.4
Mesopore volume from NLDFT (cm^3 g^{-1})	0.0710	0.0904	0.0861	0.0932
Micro/mesopore volume from NLDFT (cm^3 g^{-1})	0.347	0.245	0.216	0.248
Mesopore volume ratio (%)	20.5	36.9	39.9	37.6
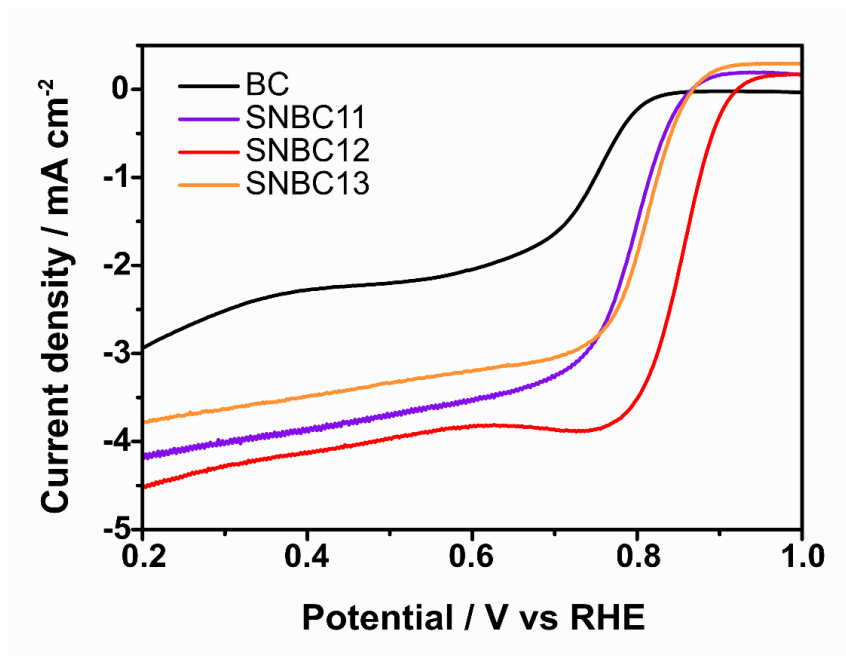
Figure 2.7 Linear sweep voltammogram curves at a scanning rate of 10 mV s^{-1} in O_2-saturated 0.1 M KOH solution with *iR* correction.
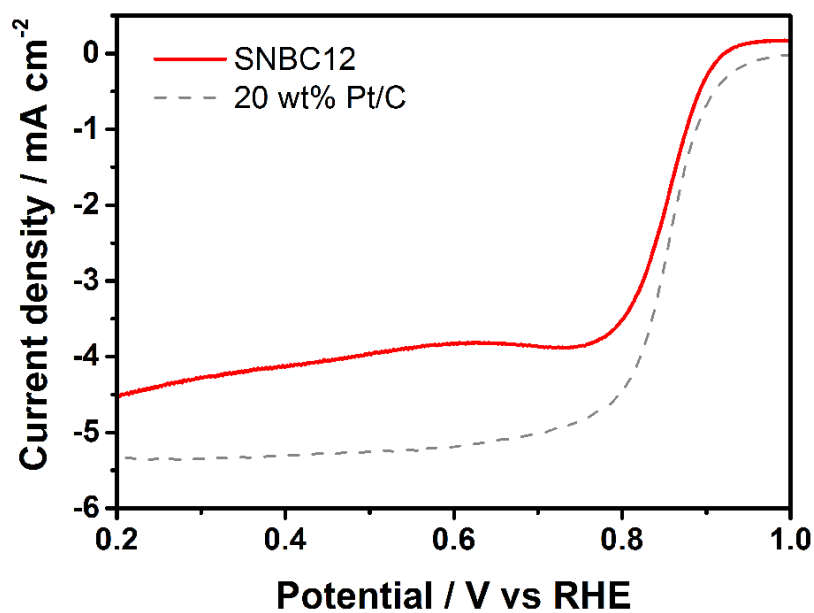
Figure 2.8 Linear sweep voltammogram curves of SNBC12 and 20wt% Pt/C at a scanning rate of 10 mV s^{-1} in O$_2$-saturated 0.1 M KOH solution with iR correction.

Table 2.4 Comparison of biomass-based ORR catalysts in 0.1 M KOH alkaline electrolyte.

Catalyst	Half-wave potential (V)	Limiting current (mA cm^{-2} at -0.8 V vs Ag/AgCl)	reference
Seaweed biomass derived (Ni,Co)/CNT nanoaerogels	0.74 (vs RHE)	5	*J. Mater. Chem. A* 2016, 4, 6376-6384
Chitosan-Derived N-Doped Carbons	~0.69 (vs RHE)	6.7	*Adv. Funct. Mater.* 2018, 28, 1707284
NiCo nanoparticles anchored on porous fibrous carbon aerogels	0.79 (vs RHE)	-	*Nano Lett.* 2016, 16, 6516-6522
Nitrogen-doped nanoporous carbon nanosheets derived from plant biomass	0.75 (vs RHE)	4.8	Energy Environ. Sci. 2014, 7, 4095-4103
Biomass lysine-derived nitrogen-doped carbon hollow cubes	0.80 (vs RHE)	6.17	*Nanoscale* 2017, 9, 1059-1067
Egg-derived mesoporous carbon microsphere	0.84 (vs RHE)	4.36	*Adv. Energy Mater.* 2016, 6, 1600794
Nitrogen-enriched carbon from bamboo fungus	-0.07 (vs Ag/AgCl)	3.55	*J. Mater. Chem. A* 2014, 2, 18263-18270
SNBC12	0.85 (vs RHE) -0.11 (vs Ag/AgCl)	5.23	**This study**

Table 2.5 Comparison of carbon-based ORR catalysts in 0.1 M KOH alkaline electrolyte.

Catalyst	Half-wave potential (V)	Limiting current (mA·cm^{-2})	reference
N, P-doped mesoporous carbon	0.85 (vs RHE)	4.3	*Nature Nanotech.* 2015, 10, 444-452
N-doped porous carbon	0.88 (vs RHE)	5.5	*Adv. Energy Mater.* 2016, 6, 1502389
N-doped porous carbon nanosheets	0.77 (vs RHE)	5.79	*Adv. Mater.* 2016, 28, 5080-5086
N, S-doped carbon nanosheets	0.77 (vs RHE)	4.3	*Nano Energy* 2016, 19, 373-381
N-doped porous carbon fiber	0.82 (vs RHE)	4.7	*Adv. Mater.* 2016, 28, 3000-3006
N, S-doped porous carbon	0.85 (vs RHE)	5.8	*Energy Environ. Sci.* 2017, 10, 742-749
2D COF-derived carbon	-0.11 (vs 3 M Ag/AgCl)	7.2	*Adv. Mater.* 2018, 30, 1706330
SNBC12	0.85 (vs RHE) -0.11 (vs 3.5 M Ag/AgCl)	5.23	**This study**

high activity of SNBC12 demonstrates its potentially excellent performance in practical devices.

In RRDE studies, the reactions at the BC electrode have peroxide yields of over 40% in the range 0.1-0.75 V (Figure 2.9). Moreover, the corresponding electron transfer numbers are less than 3, demonstrating that the mechanism for BC involves a 2-electron pathway rather than a 4-electron pathway. Doping with heteroatoms improves catalytic ability in terms of the reaction mechanism, as revealed by the RRDE results. SNBCs exhibit decreased peroxide yields and increased electron transfer numbers (> 3). The electron numbers increase in the order SNBC11 < SNBC13 < SNBC12, which corresponds to the order of their limiting current densities. Figure 2.10a shows the linear sweep voltammetry curves for SNBC12 at different RDE rotation speeds. Moreover, the electron transfer number for SNBC12 was 3.56 at 0.8 V calculated using Koutecky-Levich analysis (Figure 2.10b).

For the investigation of the electrocatalytically active sites, cyclic voltammetry at various scan rates was conducted in order to assess the electric double-layer capacitances (EDLCs) of the materials (Figure 2.11). The EDLC is proportional to the electrochemically active surface area (ECSA) of the solid-liquid interfaces.[26] The EDLC of SNBC12 is the highest (40.1 mF cm^{-2}) as compared to 36.34 mF cm^{-2} for BC, 27.04 mF cm^{-2} for SNBC11, and 26.52 mF cm^{-2} for SNBC13 (Figure 2.12). The largest ECSA for SNBC12 indicates the easy accessibility to the active sites therein.[26] The pore structure in catalysts provides a path for cations and anions of electrolyte, and it is known that ion migration is more difficult in smaller pores.[27] Therefore, mass transport is easier when the micro/mesopore ratio is more appropriate than when the micropores mainly compose the pore structure in catalysts.[28,29] As a result, the electrochemically accessible surface area can be increased in the hierarchical pore structure. Moreover, this can explain that high BET area resulting from more micropore does not lead to high ECSA in our catalysts.

48
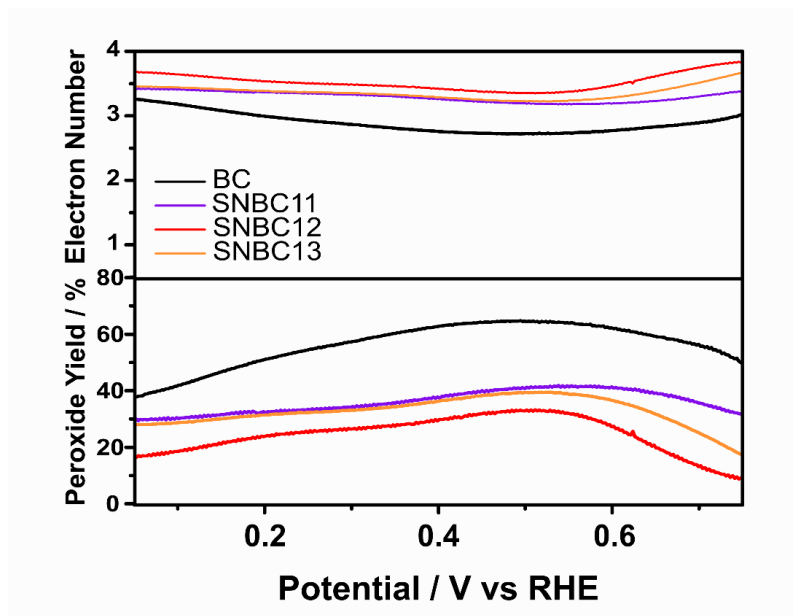
Figure 2.9 Electron-transfer numbers and peroxide yields ascertained from RRDE ring currents.
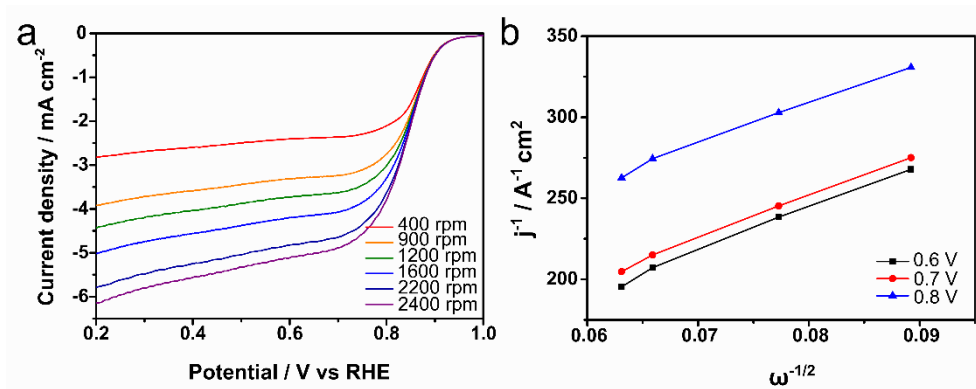
Figure 2.10 (a) Linear sweep voltammogram curves of SNBC12 at different rotation speeds. (b) Koutecky-Levich plots of SNBC12 obtained from (a).
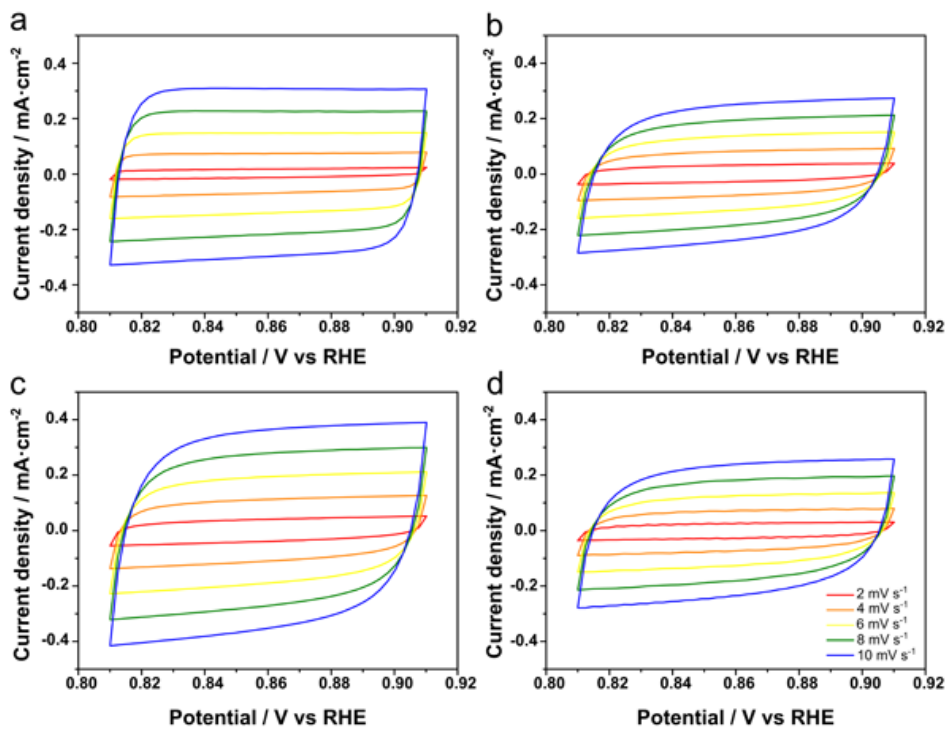
Figure 2.11 Cycling voltammogram curves at different scan rates of (a) BC, (b) SNBC11, (c) SNBC12, and (d) SNBC13.
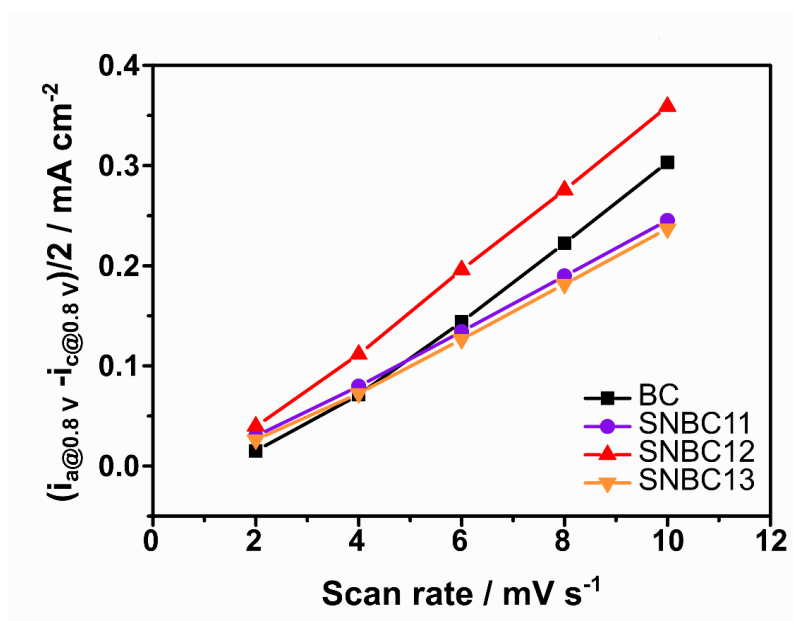
Figure 2.12 Differences in the current density variation at a potential of 0.8 V vs RHE for the calculation of EDLCs.

Moreover, an additional capacitance experiment was conducted to demonstrate the facile mass transport of our catalysts attributed to their hierarchical structure. The impedance complex-plane plots were obtained in a 0.1 M KOH solution at OCV to analyze the complex capacitance (Figure 2.13). The complex capacitance can be expressed with the real part, $C'(\omega)$, and the imaginary part, $C''(\omega)$, values, as follows:

$$C(\omega) = C'(\omega) - jC''(\omega); \quad C''(\omega) = \frac{Z''(\omega)}{\omega \ |Z(\omega)|^2}$$

Herein, the value of $C''(\omega)$ correlates with the energy dissipation of the capacitor resulting from the IR-drop and the irreversible faradaic charge transfer. In the plot of $C''(\omega)$, the maximum frequency value corresponds to relaxation frequency f_R and is related to the relaxation time constant ($\tau_R = (2\pi f_R)^{-1}$). The lower τ_R indicates a better kinetic performance of the capacitor.[29,30] From Figure 2.13 and Table 2.6, SNBC12 shows the lowest constant, 0.5 s as compared to the 0.8 s of BC. The high kinetic performance of SNBC12 results from a facile mass transport of the reactants and electrons. Moreover, the τ_R trends correspond to those of the calculated EDLCs, which shows the relation between the SNBCs' electrochemically active structure and the kinetic properties from the capacitance experiments.[31]

Impedance analysis was employed to measure the electrical conductivity of the samples (Figure 2.14). The impedances of the samples were recorded in the O_2-saturated electrolyte at 0.75 V. The results confirmed that the doping process effectively increases the electrical conductivity of the samples, as the semi-circles in the Nyquist plots for the SNBCs are distinctly diminished.[32] The Nyquist plot for SNBC12 presents the smallest semi-circle, indicating that SNBC12 exhibits the lowest charge-transfer resistance (97.9 Ω) under the operating conditions used. Thus, according to the ECSAs and resistances of the materials, the excellent electrocatalytic performance of SNBC12 results from controlling its pore structure
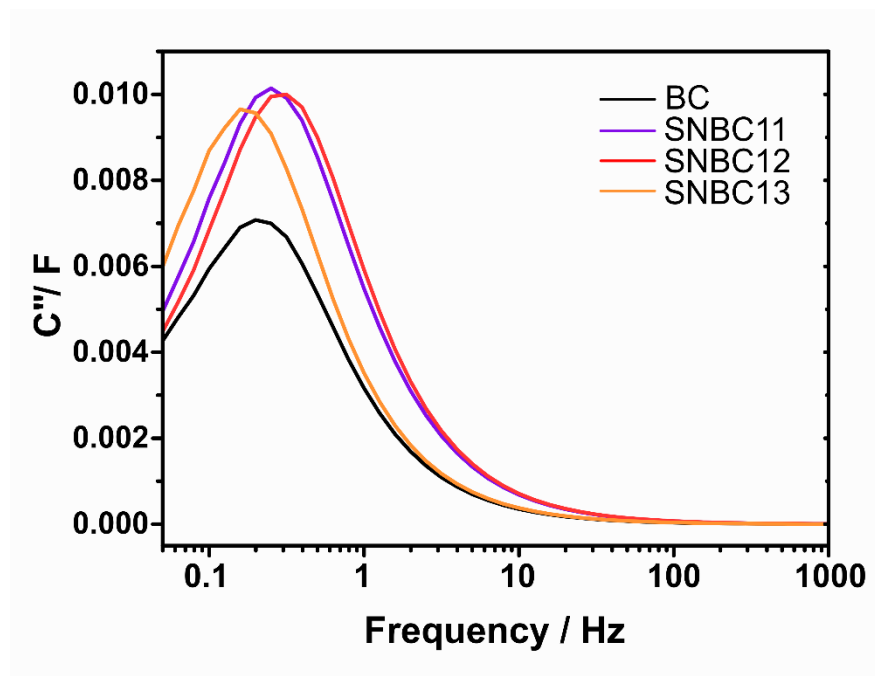
Figure 2.13 Imaginary capacitance plots.

Table 2.6 Relaxation time constant from capacitance plot of SNBCs.

Sample	BC	SNBC11	SNBC12	SNBC13
τ_R / s	0.80	0.63	0.50	1.0
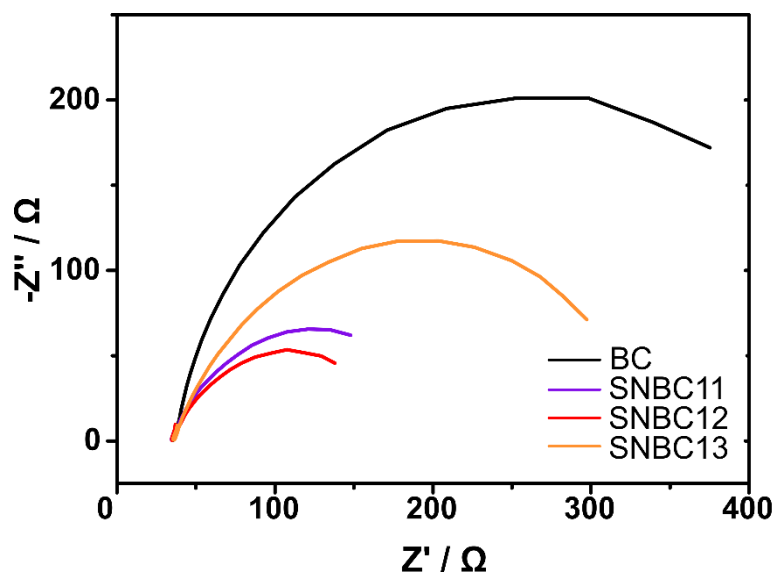
Figure 2.14 Electrochemical impedance spectroscopy of BC and the SNBCs.

and increasing the number of its active sites.

The optimal temperature used for the doping process was determined through additional experiments conducted using doping temperatures of 700, 800, and 900 °C. As shown in Figure 2.15, the activity of the SNBC doped at 800 °C is the highest. An increase in doping temperature results in the production of more catalytically active N configurations (especially graphitic N) and simultaneously a decrease in dopant content, as confirmed by XPS analysis (Figure 2.16 and Table 2.7). This leads to the SNBC doped at 800 °C having the highest activity. Additionally, the function of the doped S was examined by comparison experiments by doping BC with N but not S. The BC doped with melamine, comprising only C and N, exhibits lower limiting currents and high half-wave potential than those of the SNBC (Figure 2.17). S and N co-doping has been known to enhance ORR activity by creating an asymmetrical spin/charge density.[33]

The role of steam activation was investigated using samples that did not undergo steam activation. The steam activation notably increased the porosity of the carbonized bamboo (CB) (Figure 2.18). Compared to the low activity of CB, the S, N-co-doped carbonized bamboo (SNCB12) also exhibited greatly enhanced performance after the S, N-co-doping but relatively decreased activity compared to those of the SNBCs (Figure 2.19). The lower catalytic activity of SNCB12 shows the importance of the steam-activation process, and also, the sequence of each synthesis step. Without steam activation, the pyrolysis with thiourea is not properly performed, and the micropores in the carbon structure are insufficient, making it difficult to obtain a proper hierarchical pore structure.

The electrochemical catalytic activity of SNBC12 was also evaluated in a 0.1 M $HClO_4$ electrolyte (Figure 2.20). The half-wave potential of SNBC12 is 0.47 V, and the activity is comparable to those of the reported metal-free catalysts.[5,34,35] A methanol tolerance test using chronoamperometry was employed to confirm the
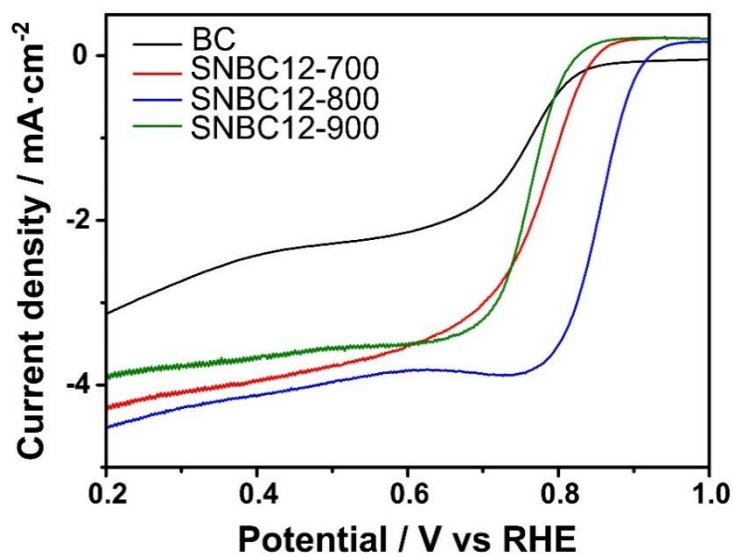
Figure 2.15 Linear sweep voltammogram curves of BC and SNBC12-T (T: doping temperature) materials at a scanning rate of 10 mV s^{-1} in O_2-saturated 0.1 M KOH solution with *iR* correction.
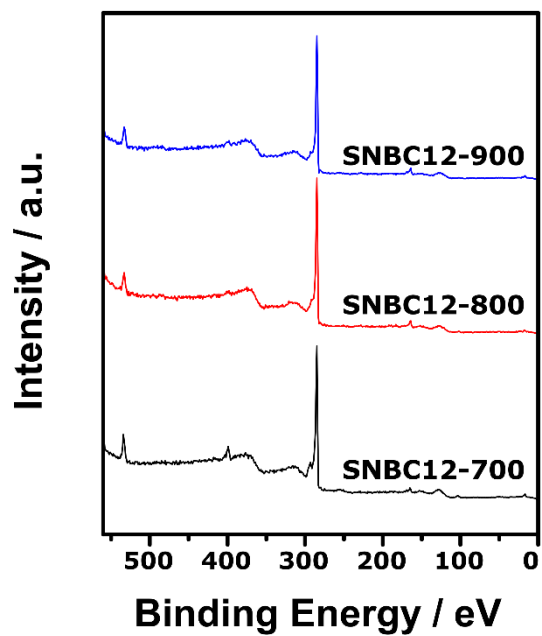
Figure 2.16 Survey XPS spectra of SNBC12-T materials.

59

Table 2.7 Atomic ratio of configurations of N of SNBC-T materials from XPS analysis.

Sample	Pyridinic N	Graphitic N	Pyrrolic N	Oxidized N
SNBC12-700	50.90	8.31	29.8	10.99
SNBC12-800	51.85	14.14	23.82	10.18
SNBC12-900	44.11	18.52	28.34	9.03
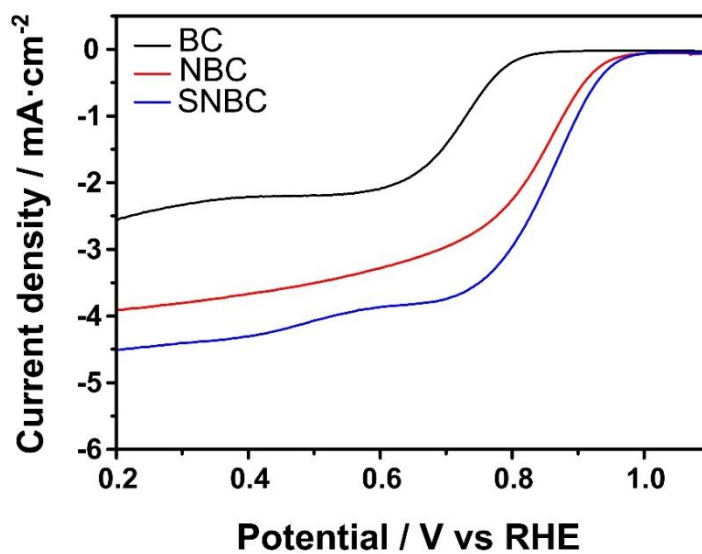
Figure 2.17 Linear sweep voltammogram curves of BC, NBC (nitrogen-doped bamboo carbon using melamine), and SNBC at a scanning rate of 10 mV s^{-1} in O$_2$-saturated 0.1 M KOH solution with *iR* correction.
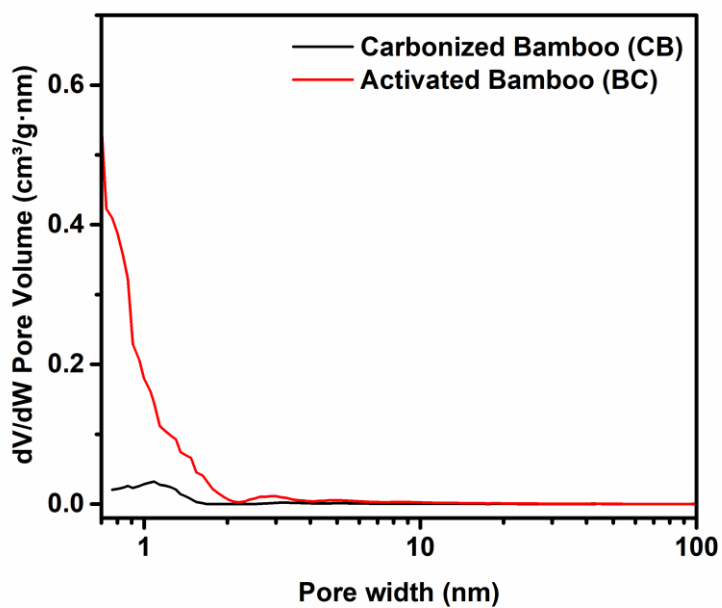
Figure 2.18 Pore size distributions of carbonized bamboo carbon and activated bamboo carbon based on NLDFT calculation.
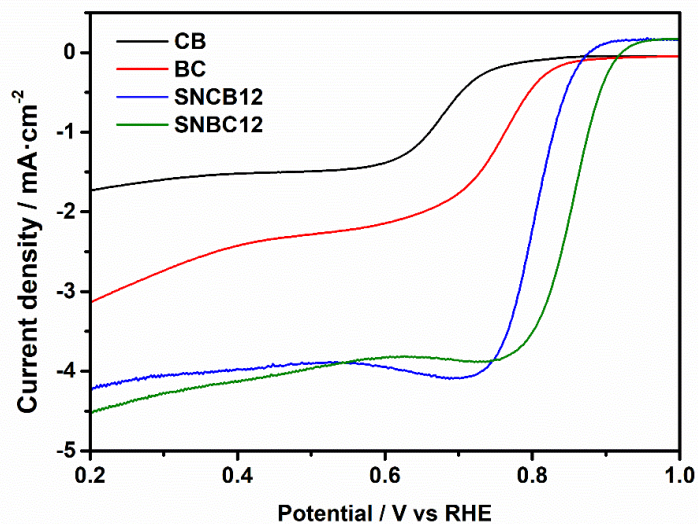
Figure 2.19 Linear sweep voltammogram curves of carbonized and S,N codoped carbonized materials compared to activated materials at a scanning rate of 10 mV s^{-1} in O$_2$-saturated 0.1 M KOH solution.
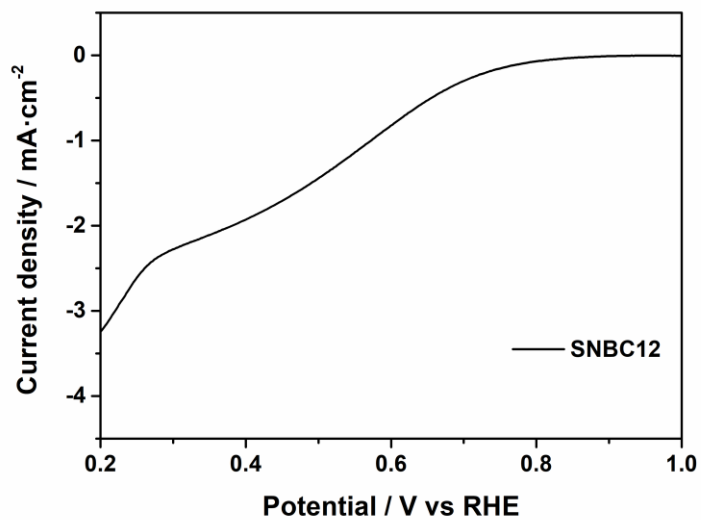
Figure 2.20 Linear sweep voltammogram curve of SNBC12 at a scanning rate of 10 mV s^{-1} in O$_2$-saturated 0.1 M HClO$_4$ solution.

applicability of SNBC12 to direct methanol fuel cells (Figure 2.21a). SNBC12 exhibits no current change upon the addition of methanol, indicating its excellent tolerance to methanol, while the current of the commercial Pt/C catalyst reduces significantly upon the addition of methanol. The durability of catalysts is of vital importance for their application in practical energy devices. Figure 2.21b shows the results of chronoamperometry analysis at 0.7 V, clearly demonstrating the superior durability of SNBC12 compared to that of Pt/C catalyst.

Figure 2.22 represents the relationships between ORR activity and different catalyst properties. With an increase in the amount of doping precursor, the ratio of mesopores in the pore structure is modified, and the N and S contents increase. Remarkably, these two factors are entirely correlated with the half-wave potential trends for the SNBCs. Thus, we can produce highly efficient catalysts from low-cost biomass materials for the following reasons: SNBC12 has a suitable micro- to mesopore ratio, which is attributed to appropriate doping with thiourea. This enables the utilization of the active sites in the micropores and also facilitates reactant and product mass transport. Secondly, the S, N co-doping greatly enhances the catalytic activity of SNBC12 based on the coexistence of S and the high content of pyridinic and graphitic N.

2.3.3. Single-cell test of AEMFC and primary Zn-air battery

To examine the practical ORR catalytic activity of SNBC, an AEMFC and a primary Zn-air battery were prepared using SNBC12 as the ORR catalyst in the cathode. The SNBC12 was applied in the cathode of a single-cell of AEMFC. Figure 2.23 shows the AEMFC performance of SNBC11, SNBC12, and SNBC13 as the ORR catalyst. The maximum power densities of SNBCs were 85.4, 217, and 119 mW cm^{-2}, respectively. Among SNBCs catalysts, SNBC12 exhibits the highest performance, which is a consistent result with the RDE test. Also, the AEMFC
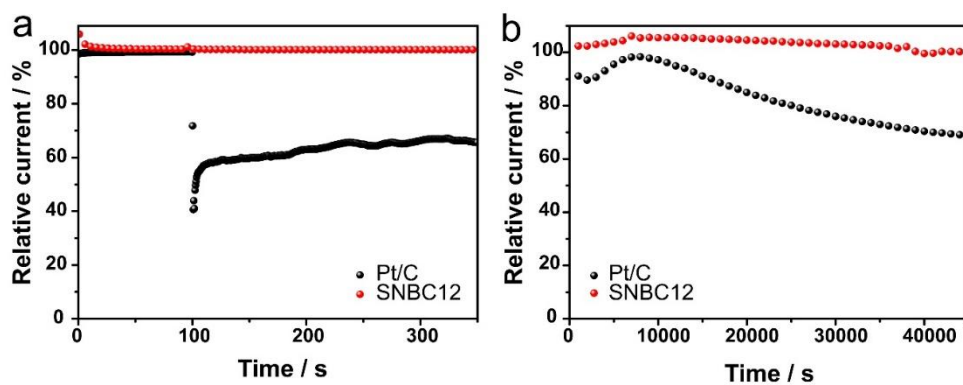
Figure 2.21 Chronoamperometric responses of Pt/C and SNBC12 (a) on the addition of methanol after 100 s, and (b) at a voltage of 0.7 V in an O_2-saturated 0.1 m KOH solution at a rotation rate of 1600 rpm.
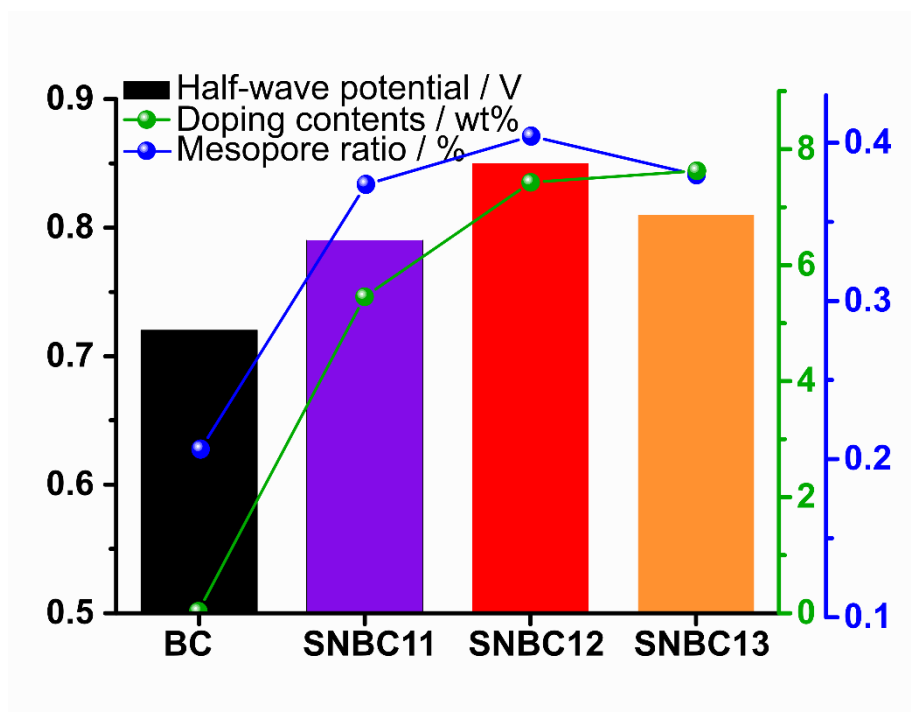
Figure 2.22 Relationships between electrocatalytic performances and material properties.
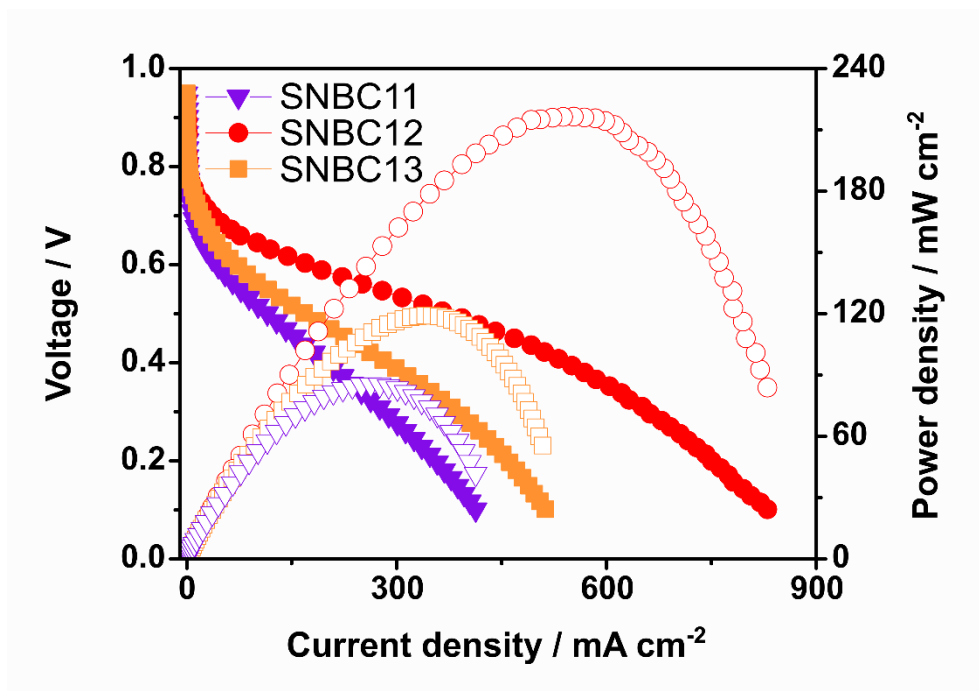
Figure 2.23 Polarization curves of AEMFCs. The catalyst loading is 2.0 mg cm^{-2}.

shows the same tendency to their catalytic activities evaluated using half-cell test (SNBC12 (-3.68 mA cm^{-2}) > SNBC13 (-0.301 mA cm^{-2}) > SNBC11 (-0.186 mA cm^{-2})). These results indicate that the ratio of mesopores and the doping contents in SNBC also influence the performance when the SNBC is applied in the practical device. Moreover, the performance of SNBC12 is comparable to or higher than those reported in the literature for other carbon-based catalysts (Figure 2.24 and Table 2.8).[36-42] Figure 2.25 shows the polarization curves for the AEMFC containing SNBC12 (2.0 mg cm^{-2}) and 20 wt% Pt/C (1.0 mg cm^{-2}) in H$_2$/O$_2$ conditions. The performance of SNBC12 is approximately 81% of that with 20 wt% Pt/C (268 mW cm^{-2}). While the performance of the AEMFC with the SNBC12 cathode in the low-current-density region is lower than that of Pt/C, it is comparable with that of Pt/C in the high-current-density region. This is attributed to the enhanced mass transport in the catalyst layer.

Figure 2.26 presents the SEM images of the catalyst layers in the membrane electrode assemblies of AEMFCs prepared with SNBC12 and 20 wt% Pt/C cathodes. The secondary pores, which are the pores formed between agglomerates and range in size from 100 to 1000 nm,[43,44] in the SNBC12 catalyst layer are larger than those in Pt/C catalyst, which results from the larger particle size (Figure 2.26ab). In addition, although the SNBC12 catalyst loading the AEMFC with the SNBC12 has a thinner catalyst layer is the same as 20 wt% Pt/C that consists of carbon support with the content of 80% (2.0 mg cm^{-2}) (Figure 2.26cd). Furthermore, the mercury porosimetry result shows that the secondary pores in the catalyst layer with SNBC12 are larger (100–3000 nm) and more numerous than Pt black (10 and 100–500 nm), as shown in Figure 2.27. Overall, the enhanced mass transport derived from the well-developed secondary pores, and intrinsic pore structure of SNBC results in the high practical cell performance of the AEMFC, demonstrating that SNBCs are promising catalysts for both the ORR and AEMFCs.
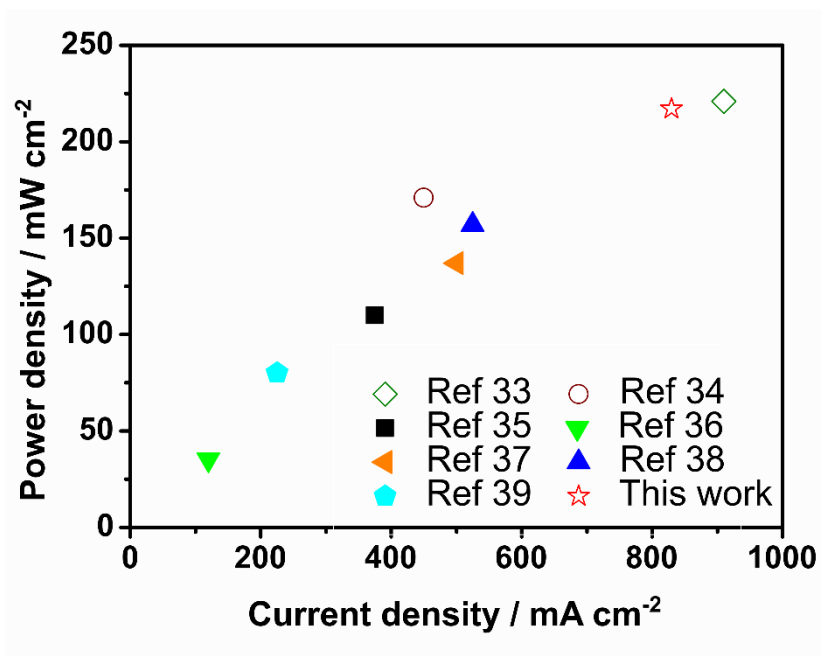
Figure 2.24 The comparison of AEMFC performances with non-noble metal catalysts reported in literature and SNBC12 (filled symbols, non-noble metal catalyst; open symbols, metal-free catalyst).

Table 2.8 Comparison of AEMFC performances using a non-noble metal catalyst.

Catalyst	Loading (mg·cm^{-2})	Total current density (mA·cm^{-2})	Peak power density (mW·cm^{-2})	Reference
Carbon nanotubes/heteroatom-doped carbon	2.0	910	221	*Angew. Chem. Int. Ed. Engl.* 2014, 126, 4102-4106
Graphitic carbon nitride-carbon nanofiber	2.0	450	171	*Sci. Rep.* 2015, 5, 8376
Fe-N doped carbon capsule	0.2	375	110	*ACS nano* 2016, 10, 5922-5932
CoMn alloy supported n-doped porous graphene	2.0	120	35.2	*ACS Catal.* 2017, 7, 6700-6710
Fe-N-S supported carbon	4.0	500	137	*J. Mater. Chem. A* 2017, 5, 19790-19799
Fe-N-C	2.0	525	157	*Sci. Rep.* 2017, 7, 5396
Fe-N-doped carbide-derived carbon	1.5	225	80	*J. Power Source* 2018, 375, 233-243
SNBC12	2.0	830	217	**This study**
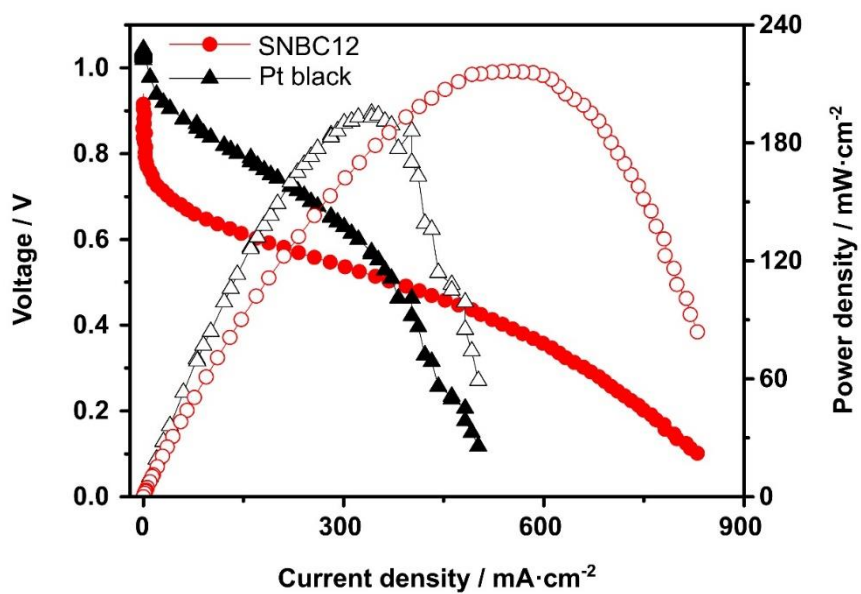
Figure 2.25 Polarization curves of AEMFCs prepared with SNBC12 (2.0 mg cm^{-2}) and Pt black (2.0 mg cm^{-2}).
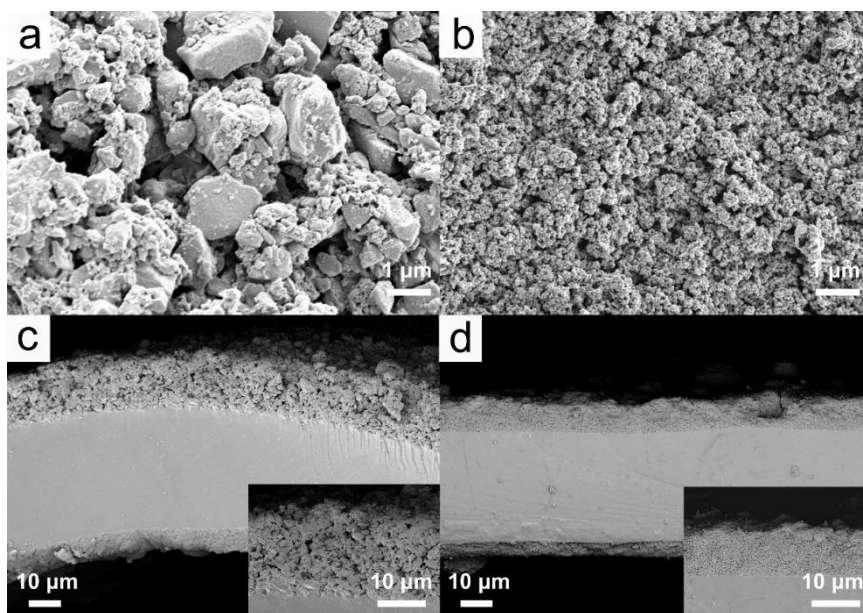
Figure 2.26 SEM images of MEA in AEMFCs: Top view of catalyst layer of (a) SNBC12 and (b) Pt black. Cross-section view of MEA with (c) SNBC12 and (d) Pt black.
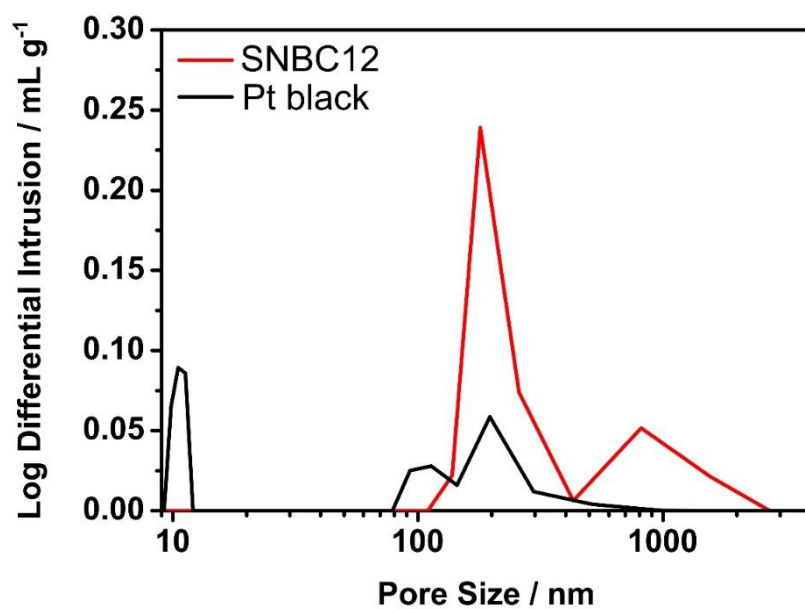
Figure 2.27 Pore size distribution of catalyst layers including SNBC12 and Pt black measured by the mercury porosimeter.

A primary Zn-air battery was constructed with the SNBCs to evaluate the practical ORR activity of SNBC. In addition to AEMFCs, primary Zn-air batteries are a good application for ORR electrocatalysts as the ORR occurs in the cathode during discharge.[44-47] Figure 2.28 shows the polarization curves of the primary battery, prepared with SNBC11, SNBC12, and SNBC13 as air electrodes. The Zn-air battery shows a tendency similar to the results of the RDE and AEMFC tests: SNBC11 < SNBC13 < SNBC12. The maximum power density and total current density of the single-cell prepared with SNBC12 are 156 mW cm^{-2} and 830 mA cm^{-2}, respectively. As shown in Figure 2.29 and Table 2.9, the primary battery exhibits superior performance compared to other biomass-based oxygen reduction catalysts.[48-53] Figure 2.30a presents the comparison of cell performance between SNBC12 and 20 wt% Pt/C. Despite them having the same catalyst loading (4 mg cm^{-2}), the maximum power density of Zn-air battery with SNBC was 156 mW cm^{-2}, which is 86% that prepared with 20 wt% Pt/C (181 mW cm^{-2}). Furthermore, the specific capacity and energy density of SNBC12 are 348 mAh cm^{-2} and 360 mWh cm^{-2}, respectively, which are much higher than those of Pt/C (244 mAh cm^{-2} and 267 mWh cm^{-2}) (Figure 2.30b and c). To investigate the resistance of the primary battery, electronic impedance spectra were obtained at 1.1 V (Figure 2.31). The Nyquist plot shows that SNBC12 exhibits a higher charge-transfer resistance and lower ohmic resistance than those of 20 wt% Pt/C. As the two catalysts were applied with the same loading of 4.0 mg cm^{-2}, SNBC exhibited lower catalytic activity than that of 20 wt% Pt/C, leading to the higher charge-transfer resistance in the SNBC. However, the catalyst layer prepared with SNBC12 had a smaller thickness, resulting in a smaller ohmic resistance. This is due to the enhanced utilization of SNBC12, caused by its hierarchical pore structure as well as well-developed secondary pore structure. Thus, SNBC is also a good candidate for a primary Zn-air battery catalyst.
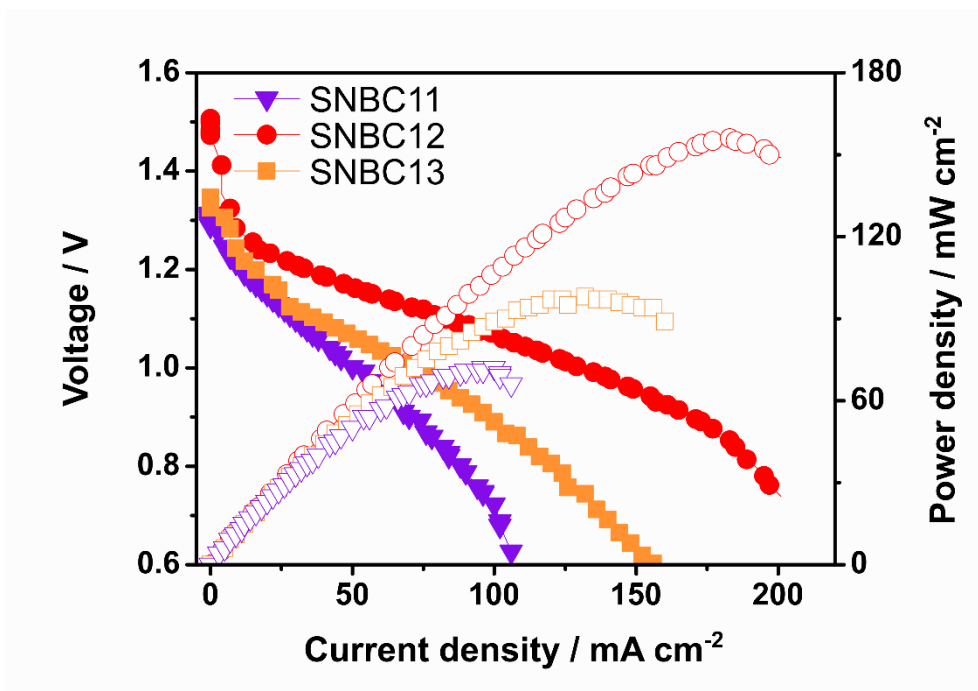
Figure 2.28 Performance of primary Zn−air batteries. The catalyst loading is 4.0 mg cm^{-2}.
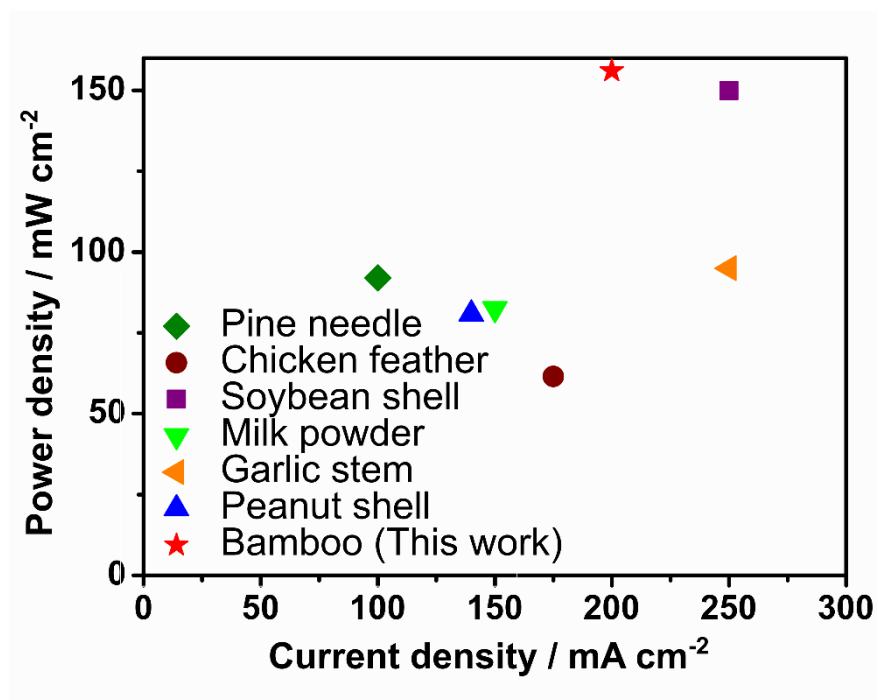
Figure 2.29 Comparison of Zn–air battery performances with biomass-based catalysts reported in literature and SNBC12.

Table 2.9 Comparison of primary Zn-air battery performances using biomass-based materials.

Source of catalyst	Loading (mg·cm^{-2})	Total current density (mA·cm^{-2})	Peak power density (mW·cm^{-2})	Reference
Waste pine needle	-	100	92	*Electrochim. Acta* 2017, 250, 384-392
Chicken feather	1.0	175	61.5	*Small* 2018, 14, 1800563
Soybean shell	2.0	250	149.9	*Chem. Eng. J.* 2017, 334, 1270-1280
Milk powder	2.0	150	82.5	*Energy Storage Mat.* 2018, 11, 134-143
Garlic stem	1.5	250	95	*Energy* 2018, 15, 43-55
Peanut shell	1.0	140	80.8	*Energy Storage Mat.* 2018, 12, 277-283
Bamboo	4.0	200	156	**This study**
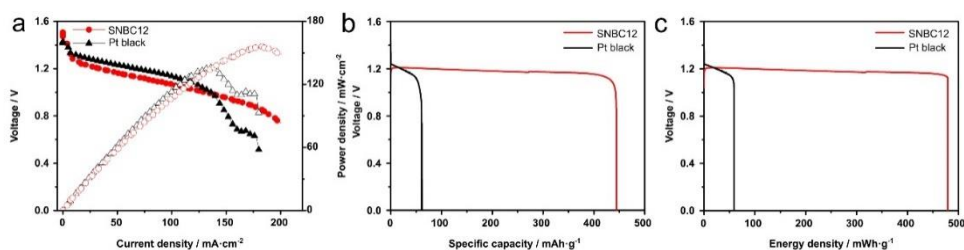
Figure 2.30 (a) Performance of primary Zn-air batteries prepared with SNBC12 (4.0 mg cm^{-2}) and Pt black (4.0 mg cm^{-2}). (b) Typical discharge curves of primary Zn-air batteries containing SNBC12 and Pt black electrodes recorded at a constant current density of 10 mA cm^{-2}. (c) Energy density plot of primary Zn-air batteries containing SNBC12 and Pt black electrodes recorded at 10 mA cm^{-2}.
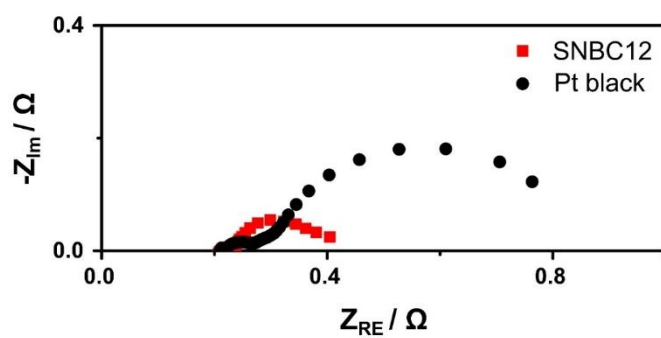
Figure 2.31 Nyquist plots of primary Zn-air batteries with SNBC12 and 20wt% Pt/C electrocatalyst obtained at 1.1 V.

2.4. Conclusions

Bamboo-derived porous SNBCs were synthesized via steam activation and pyrolysis of bamboo stem and thiourea, a source of S and N. Interestingly, the modification of bamboo using thiourea was found to be a method for developing hierarchical pore structure as well as for S and N co-doping. SNBC12 exhibits superior ORR performance with a half-wave potential of 0.85 V, which is higher than those of other biomass-based and carbon-based materials. In the cathodes of an AEMFC and a primary Zn-air battery, SNBC12 showed high cell performances of 217 mW cm^{-2} and 156 mW cm^{-2}, respectively. Additionally, this represents the first application of a biomass-based catalyst in a practical AEMFC. Thus, this work provides a green strategy for the design of high-performance and sustainable ORR catalysts for practical applications.

Most of the contents of this chapter were published in the article, "Biomass-Derived Air Cathode Materials: Pore-Controlled S,N-Codoped Carbon for Fuel Cells and Metal−Air Batteries" (*ACS Catalysis* **2019, *9*, 3389-3398)

2.5. References

1.   J. Tang, J. Liu, N. L. Torad, T. Kimura, Y. Yamauchi, Tailored Design of Functional Nanoporous Carbon Materials toward Fuel Cell Applications. *Nano Today* 2014, **9**, 305-323.

2.   H.-W. Liang, X. Zhuang, S. Brüller, X. Feng, K. Müllen, Hierarchically Porous Carbons with Optimized Nitrogen Doping as Highly Active Electrocatalysts for Oxygen Reduction. *Nat. Commun.* 2014, **5**, 4973.

3.   G. A. Ferrero, K. Preuss, A. B. Fuertes, M. Sevilla, M. M. Titirici, The Influence of Pore Size Distribution on the Oxygen Reduction Reaction Performance in Nitrogen Doped Carbon Microspheres. *J. Mater. Chem. A* 2016, **4**, 2581-2589.

4.   M. Borghei, J. Lehtonen, L. Liu, O. J. Rojas, Advanced Biomass-derived Electrocatalysts for the Oxygen Reduction Reaction. *Adv. Mater.* 2018, **30**, 1703691.

5.   P. Chen, L.-K. Wang, G. Wang, M.-R. Gao, J. Ge, W.-J. Yuan, Y.-H. Shen, A.-J. Xie, S.-H. Yu Nitrogen-doped Nanoporous Carbon Nanosheets Derived from Plant Biomass: an Efficient Catalyst for Oxygen Reduction Reaction. *Energy Environ. Sci*. 2014, **7**, 4095-4103.

6.   N. Ma, Y. Jia, X. Yang, X. She, L. Zhang, Z. Peng, X. Yao, D. Yang, Seaweed Biomass Derived (Ni,Co)/CNT Nanoaerogels: Efficient Bifunctional Electrocatalysts for Oxygen Evolution and Reduction Reactions. *J. Mater. Chem. A* 2016, **4**, 6376-6384.

7.   M. Ma, S. You, W. Wang, G. Liu, D. Qi, X. Chen, J. Qu, N. Ren, Biomass-derived Porous Fe_3C/tungsten carbide/graphitic Carbon Nanocomposite for Efficient Electrocatalysis of Oxygen Reduction. *ACS Appl. Mater. Interfaces* 2016, **8**, 32307-32316.

8. H. Wu, J. Geng, H. Ge, Z. Guo, Y. Wang, G. Zheng, Egg-derived Mesoporous Carbon Microspheres as Bifunctional Oxygen Evolution and Oxygen Reduction Electrocatalysts. *Adv. Energy Mater.* 2016, **6**, 1600794.

9. C. Guo, W. Liao, Z. Li, L. Sun, C. Chen, Easy Conversion of Protein-rich Enoki Mushroom Biomass to a Nitrogen-doped Carbon Nanomaterial as a Promising Metal-free Catalyst for Oxygen Reduction Reaction. *Nanoscale* 2015, **7**, 15990-15998.

10. J.-C. Li, P.-X. Hou, S.-H. Zhao, C. Liu, D.-M. Tang, M. Cheng, F. Zhang, H.-M. Cheng, A 3D Bi-functional Porous N-doped Carbon Microtube Sponge Electrocatalyst for Oxygen Reduction and Oxygen Evolution Reactions. *Energy Environ. Sci.* 2016, **9**, 3079-3084.

11. K. H. P. S. Abdul, I. U. H. Bhat, M. Jawaid, A. Zaidon, D. Hermawan, Y. S. Hadi Bamboo Fibre Reinforced Biocomposites: A Review. *Mater. Des.* 2012, **42**, 353-368.

12. F. Y. Wang, H. Wang, J. W. Ma, Adsorption of Cadmium (II) Ions from Aqueous Solution by a New Low-cost Adsorbent—Bamboo Charcoal. *J. Hazard. Mater.* 2010, **177**, 300-306.

13. J. E. Park, M. S. Lim, J. K. Kim, H. J. Choi, Y.-E. Sung, Y.-H. Cho, Optimization of Cell Components and Operating Conditions in Primary and Rechargeable Zinc-air Battery. *J. Ind. Eng. Chem.* 2019, **69**, 161-170.

14. B. Zhu, K. Qiu, Z. Shang, Z. Guo, Naturally Derived Porous Carbon with Selective Metal- and/or Nitrogen-doping for Efficient CO_2 Capture and Oxygen Reduction. *J. Mater. Chem. A* 2015, **3**, 5212-5222.

15. J. Encalada, K. Savaram, N. A. Travlou, W. Li, Q. Li, C. Delgado-Sánchez, V. Fierro, A. Celzard, H. He, T. J. Bandosz, Combined Effect of Porosity and Surface Chemistry on the Electrochemical Reduction of Oxygen on Cellular Vitreous Carbon Foam Catalyst. *ACS Catal.* 2017, **7**, 7466-7478.

16. D. C. Higgins, M. A. Hoque, F. Hassan, J.-Y. Choi, B. Kim, Z. Chen, Oxygen Reduction on Graphene–carbon Nanotube Composites Doped Sequentially with Nitrogen and Sulfur. *ACS Catal*. 2014, **4**, 2734-2740.

17. L. Lai, J. R. Potts, D. Zhan, L. Wang, C. K. Poh, C. Tang, H. Gong, Z. Shen, J. Lin, R. S. Ruoff, Exploration of the Active Center Structure of Nitrogen-doped Graphene-based Catalysts for Oxygen Reduction Reaction. *Energy Environ. Sci*. 2012, **5**, 7936-7942.

18. J. Zhu, H. Zhou, C. Zhang, J. Zhang, S. Mu, Dual Active Nitrogen Doped Hierarchical Porous Hollow Carbon Nanospheres as an Oxygen Reduction Electrocatalyst for Zinc–air Batteries. *Nanoscale* 2017, **9**, 13257-13263.

19. P. Bhattacharya, M. I. Nandasiri, D. Lv, A. M. Schwarz, J. T. Darsell, W. A. Henderson, D. A. Tomalia, J. Liu, J.-G. Zhang, J. Xiao, Polyamidoamine Dendrimer-based Binders for High-loading Lithium–sulfur Battery Cathodes. *Nano Energy* 2016, **19**, 176-186.

20. A. C. Ferrari, J. C. Meyer, V. Scardaci, C. Casiraghi, M. Lazzeri, F. Mauri, S. Piscanec, D. Jiang, K. S. Novoselov, S. Roth and A. K. Geim, Raman Spectrum of Graphene and Graphene Layers, *Physical Review Letters* 2006, **97**, 187401.

21. S. Feng, M. C. dos Santos, B. R. Carvalho, R. Lv, Q. Li, K.Fujisawa, A. L. Elías, Y. Lei, N. Perea-López, M. Endo, M. Pan, M. A. Pimenta, M. Terrones, Ultrasensitive Molecular Sensor Using N-doped Graphene through Enhanced Raman Scattering. *Sci. Adv.* 2016, **2**, e1600322.

22. Z.-H. Sheng, L. Shao, J.-J. Chen, W.-J. Bao, F.-B. Wang, X.-H. Xia, Catalyst-free Synthesis of Nitrogen-doped Graphene via Thermal Annealing Graphite Oxide with Melamine and Its Excellent Electrocatalysis. *ACS Nano* 2011, **5**, 4350-4358.

23. A. M. El-Sawy, I. M. Mosa, D. Su, C. J. Guild, S. Khalid, R. Joesten, J. F. Rusling, S. L. Suib, Controlling the Active Sites of Sulfur-doped Carbon Nanotube–graphene Nanolobes for Highly Efficient Oxygen Evolution and Reduction Catalysis. *Adv. Energy Mater*. 2016, **6**, 1501966.

24. C. Hu, L. Dai, Multifunctional Carbon-based Metal-free Electrocatalysts for Simultaneous Oxygen Reduction, Oxygen Evolution, and Hydrogen Evolution. *Adv. Mater*. 2017, **29**, 1604942.

25. Z. Liu, H. Nie, Z. Yang, J. Zhang, Z. Jin, Y. Lu, Z. Xiao, S. Huang, Sulfur–nitrogen Co-doped Three-dimensional Carbon Foams with Hierarchical Pore Structures as Efficient Metal-free Electrocatalysts for Oxygen Reduction Reactions. *Nanoscale* 2013, **5**, 3283-3288.

26. Y. Liu, H. Wang, D. Lin, J. Zhao, C. Liu, J. Xie, Y. Cui, A Prussian Blue Route to Nitrogen-doped Graphene Aerogels as Efficient Electrocatalysts for Oxygen Reduction with Enhanced Active Site Accessibility. *Nano Res*. 2017, **10**, 1213-1222.

27. D. Qu, H. Shi, Studies of Activated Carbons Used in Double-layer Capacitors. *J. Power Soc*. 1998, **74**, 99-107.

28. C. Z. Yuan, B. Gao, L. F. Shen, S. D. Yang, L. Hao, X. J. Lu, F. Zhang, L. J. Zhang, X. G. Zhang, Hierarchically Structured Carbon-based Composites: Design, Synthesis and Their Application in Electrochemical Capacitors. *Nanoscale* 2011, **3**, 529-545.

29. T. Thomberg, A. Janes, E. Lust, Energy and Power Performance of Electrochemical Double-layer Capacitors Based on Molybdenum Carbide Derived Carbon. *Electrochim. Acta* 2010, **55**, 3138-3143.

30. D. Y. Chung, K. J. Lee, S.-H. Yu, M. Kim, S. Y. Lee, O.-H. Kim, H.-J. Park, Y.-E. Sung, Alveoli-inspired Facile Transport Structure of N-doped Porous

Carbon for Electrochemical Energy Applications. *Adv. Energy Mater*. 2015, **5**, 1401309.

31. S. H. Lee, J. Kim, D. Y. Chung, J. M. Yoo, H. S. Lee, M. J. Kim, B. S. Mun, S. G. Kwon, Y.-E. Sung, T. Hyeon, Design Principle of Fe–N–C Electrocatalysts: How to Optimize Multimodal Porous Structures?, *J. Am. Chem. Soc*. 2019, **141**, 2035-2045.

32. Z. Pei, H. Li, Y. Huang, Q. Xue, Y. Huang, M. Zhu, Z. Wang, C. Zhi, Texturing In Situ: N,S-enriched Hierarchically Porous Carbon as a Highly Active Reversible Oxygen Electrocatalyst. *Energy Environ. Sci*. 2017, **10**, 742-749.

33. L. Ji, J. Yan, J. Mietek, Q. S. Zhang, Sulfur and Nitrogen Dual-doped Mesoporous Graphene Electrocatalyst for Oxygen Reduction with Synergistically Enhanced Performance. *Angew. Chem. Int. Ed*. 2002, **51**, 11496-11500.

34. C. Tang, H.-F. Wang, X. Chen, B.-Q. Li, T.-Z. Hou, B. Zhang, Q. Zhang, M.-M. Titirici, F. Wei, Topological Defects in Metal-free Nanocarbon for Oxygen Electrocatalysis. *Adv. Mater*. 2016, **28**, 6845-6851.

35. W. Yang, T.-P. Fellinger, M. Antonietti, Efficient Metal-free Oxygen Reduction in Alkaline Medium on High-surface-area Mesoporous Nitrogen-doped Carbons Made from Ionic Liquids and Nucleobases. *J. Am. Chem. Soc*. 2011, **133**, 206-209.

36. Y. J. Sa, C. Park, C. Jeong, S. H. Park, Z. Lee, K. T. Kim, G. G. Park, S. H. Joo, Carbon Nanotubes/heteroatom-doped Carbon Core–sheath Nanostructures as Highly Active, Metal-free Oxygen Reduction Electrocatalysts for Alkaline Fuel Cells. *Angew. Chem. Int. Ed*. 2014, **53**, 4102-4106.

37.   O.-H. Kim, Y.-H. Cho, D. Y. Chung, M. J. Kim, M. J. Yoo, M. J. Park, M. J. Choe, Y.-E. Sung, Facile and Gram-scale Synthesis of Metal-free Catalysts: toward Realistic Applications for Fuel Cells. *Sci. Rep.* 2015, **5**, 8376.

38.   G. A. Ferrero, K. Preuss, A. Marinovic, A.B. Jorge, N. Mansor, D. J. Brett, A. B. Fuertes, M. Sevilla, M. M. Titirici, Fe–N-doped Carbon Capsules with Outstanding Electrochemical Performance and Stability for the Oxygen Reduction Reaction in Both Acid and Alkaline Conditions. *ACS Nano* 2016, **10**, 5922-5932.

39.   H.-C. Huang, Y.-C. Lin, S.-T. Chang, C.-C. Liu, K.-C. Wang, H.-P. Jhong, J.-F. Lee, C.-H. Wang, Effect of a Sulfur and Nitrogen Dual-doped Fe–N–S Electrocatalyst for the Oxygen Reduction Reaction. *J. Mater. Chem. A* 2017, **5**, 19790-19799.

40.   H. Lee, M. J. Kim, T. Lim, Y. E. Sung, Y. E. Kim, H. N. Lee, O. J. Kwon, Y. H. Cho, A Facile Synthetic Strategy for Iron, Aniline-based Non-precious Metal Catalysts for Polymer Electrolyte Membrane Fuel Cells. *Sci. Rep.* 2017, **7**, 5396.

41.   S. K. Singh, V. Kashyap, N. Manna, S. N. Bhange, R. Soni, R. Boukherroub, S. Szunerits, S. Kurungot, Efficient and Durable Oxygen Reduction Electrocatalyst Based on CoMn Alloy Oxide Nanoparticles Supported Over N-Doped Porous Graphene. *ACS Catal.* 2017, **7**, 6700-6710.

42.   S. Ratso, I. Kruusenberg, M. Käärik, M. Kook, L. Puust, R. Saar, J. Leis, K. Tammeveski, Highly Efficient Transition Metal and Nitrogen Co-doped Carbide-derived Carbon Electrocatalysts for Anion Exchange Membrane Fuel Cells. *J. Power Sources* 2018, **375**, 233-243.

43.   Z. Yu, R. Carter, Measurements of Effective Oxygen Diffusivity, Pore Size Distribution, and Porosity in PEM Fuel Cell Electrodes. *ECS Trans.* 2009, **19**, 1-15.

44. R. Wu, Q. Liao, X. Zhu, H. Wang, Pore Network Modeling of Cathode Catalyst Layer of Proton Exchange Membrane Fuel Cell. *Int. J. Hydrogen Energy* 2012, **37**, 11255-11267.

45. J. S. Lee, G. S. Park, G. S. Lee, S. T. Kim, R. Cao, M. Liu, J. Cho, Ketjenblack Carbon Supported Amorphous Manganese Oxides Nanowires as Highly Efficient Electrocatalyst for Oxygen Reduction Reaction in Alkaline Solutions. *Nano Lett*. 2011, **11**, 5362-5366.

46. L.-L. Tian, J. Yang, M.-Y. Weng, R. Tan, J.-X. Zheng, H.-B. Chen, H.-B. Zhuang, L.-M. Dai, F. Pan, Fast Diffusion of O_2 on Nitrogen-doped Graphene to Enhance Oxygen Reduction and Its Application for High-rate Zn–air Batteries. *ACS Appl. Mater. Interfaces* 2017, **9**, 7125-7130.

47. J. Yang, J. Hu, M. Weng, R. Tan, R. Tian, J. Yang, J. Amine, J. Zheng, H. Chen, F. Pan, Fe-cluster Pushing Electrons to N-doped Graphitic Layers with $Fe_3C(Fe)$ Hybrid Nanostructure to Enhance O_2 Reduction Catalysis of Zn-air Batteries. *ACS Appl. Mater. Interfaces* 2017, **9**, 4587-4596.

48. J. E. Park, M.-J. Kim, M. S. Lim, S. Y. Kang, J. K. Kim, S.-H. Oh, M. Her, Y.-H. Cho, Y.-E. Sung, Graphitic Carbon Nitride-carbon Nanofiber as Oxygen Catalyst in Anion-Exchange Membrane Water Electrolyzer and Rechargeable Metal–air Cells. *Appl. Catal. B.* 2018, **237**, 140-148.

49. M. Wang, X. Lei, L. Hu, P. Zhang, H. Hu, J. Fang, High-performance Waste Biomass-derived Microporous Carbon Electrocatalyst with a Towel-like Surface for Alkaline Metal/air Batteries. *Electrochim. Acta* 2017, **250**, 384-392.

50. X. Chen, L. Wei, L. Wang, L. Zhai, Z. Chen, Z. Tan, Z. Zhou, A. K. Ng, X. Liao, X. Chen, Milk Powder-derived Bifunctional Oxygen Electrocatalysts for Rechargeable Zn-air Battery. *Energy Storage Mater*. 2018, **11**, 134-143.

51.   Z. Jiawei, L. Wenqiang, L. Shuaihu, Z. Jian, Z. Huang, Z. Chengtian, Z. Jianan, M. Shichun, Defective N/S-codoped 3D Cheese-like Porous Carbon Nanomaterial toward Efficient Oxygen Reduction and Zn–air Batteries. *Small* 2018, **14**, 1800563.

52.   Z. Ma, K. Wang, Y. Qiu, X. Liu, C. Cao, Y. Feng, P. Hu, Nitrogen and Sulfur co-doped Porous Carbon Derived from Bio-waste as a Promising Electrocatalyst for Zinc-air Battery. *Energy* 2018, **143**, 43-55.

53.   L. Yang, X. Zeng, D. Wang, D. Cao, Biomass-derived FeNi Alloy and Nitrogen-codoped Porous Carbons as Highly Efficient Oxygen Reduction and Evolution Bifunctional Electrocatalysts for Rechargeable Zn-air Battery. *Energy Storage Mater.* 2018, **12**, 277-283.

54.   C. Zhao, G. Liu, N. Sun, X. Zhang, G. Wang, Y. Zhang, H. Zhang, H. Zhao, Biomass-derived N-doped Porous Carbon as Electrode Materials for Zn-air Battery Powered Capacitive Deionization. *Chem. Eng. J.* 2018, **334**, 1270-1280.

Chapter 3. Controlling Active Sites of Fe-N-C Electrocatalysts for Anion Exchange Membrane Fuel Cells and Zinc-Air Batteries

3.1. Introduction

Fe-based catalysts have exhibited excellent ORR performance when compared to other non-precious metal catalysts.[1] The synthetic methods for Fe-based catalysts using impregnation, polymer, metal-containing complex, and metal-organic framework, arouse the controversy on the exact active site, since the annealing at high temperature, an essential process for efficient Fe-based catalysts, makes it difficult to control the generation of the specific active site.[1] The most suggested active sites are carbon-coated iron particles (Fe@C) and a single iron atom bonded with nitrogen (Fe-N_x).[2] As the use of single-atom catalysts has been spotlighted throughout the recent catalyst research, the synthesis and analysis methods for them have been rapidly developed.[3] The catalysts with Fe-N_x synthesized through the current technology exhibit high performance in a half-cell ORR and a single-cell operation due to its 4-electron pathway mechanism.[4] Meanwhile, Fe@C, an active site that is easily synthesized by high-temperature annealing with a large amount of Fe, is also known for catalyzing ORR efficiently.[5,6] Some researchers represent phenomena that improve ORR activities when the two active sites coexist.[7,8] However, it is hard to find research that achieves notable performance through designing the model system with two active sites.

Herein, we propose a strategy to develop the model system for ORR catalysts with both Fe@C and Fe-N_x active sites and demonstrate high performance. In specific, we introduce a synthetic method, named as pyro-synthesis, which has been

used for producing a highly crystalline metal oxide in a fast and large-scale method.[9] Pyro-synthesis transforms some of the Fe-N complexes to iron oxide that is further reduced to Fe@C via heat-treatment except for the remained Fe-N bonding in the form of Fe-N_x sites. We control the Fe@C/Fe-N_x ratio by different ratios between the amount of Fe-N complex and carbon source. Controlling the Fe@C/Fe-N_x ratio provides the optimum point that exhibits the notable ORR activity. The excellent performance is attributed to the sufficient density and condition of active sites that lowers oxygen binding energy of Fe. As the cathode of anion exchange membrane fuel cells and Zn-air batteries, the activity of catalyst surpasses that of commercial Pt catalysts and other ORR catalysts. Through *in situ* XAFS study, we investigated the ORR mechanism of catalysts mixed with Fe@C and Fe-N_x and found the condition of the highly active catalyst when it comes to catalysts with both sites. Therefore, we demonstrate the design of active non-precious metal ORR catalysts by utilizing active sites efficiently.

3.2. Experimental section

3.2.1. Preparation of FeNCs

The FeNC catalysts were synthesized by pyro-synthesis using iron(II) acetate $(FeC_4O_4H_6$, Sigma Aldrich), 1-10 phenanthroline $(C_{12}H_8N_2)$ as precursors and tetraethylene glycol (TTEG) as a solvent, carbon source, and fuel of pyro-reaction, respectively. In the first step, starting precursors (iron acetate and 1-10 phenanthroline) were dissolved in 48 ml of TTEG solvent in the molar ratio 1 : 4 (Fe : N) for 24 h. After obtaining a homogenous solution, Ketjen black (KB) powder for each amount (600, 2000, 4000, and 10000 mg) was uniformly dispersed in the solution. The homogenous mixture was ignited by a torch, causing a self-combustion reaction. After that, the subsequent heat-treatment was performed at 800 °C in an N_2 atmosphere for 1h. The heated powders were stirred in diluted sulfuric acid for 24 h and dried in a vacuum oven at 120 °C. In the final step, the dried powder was heated again at 800 °C in Ar atmosphere for 1h.

3.2.2. Physicochemical characterization of FeNCs

The morphology and elemental distribution of FeNCs were observed using transmission electron microscopy (TEM), cs-corrected scanning TEM (cs-STEM), and STEM energy-dispersive X-ray spectroscopy (STEM-EDS) via a JEM-2100F (JEOL Ltd., Japan) and Titan 80-300 (FEI, USA). An X-ray diffractometer (D/MAX-2500/PC, Rigaku Co., Japan) with a Cu Kα (λ = 0.15418 nm) source was used to obtain X-ray diffraction (XRD) spectra. The Raman spectra of the FeNCs were collected with a Raman spectrometer (LabRAM HV Evolution, Horiba, Japan) using a 532 nm laser. Near-edge X-ray absorption fine structure (NEXAFS) of C K-edge were performed at the beamline 4D of Pohang Light Source (PLS-II) (Pohang, Republic of Korea). The chemical statues of the element in FeNCs were examined using X-ray photon spectroscopy (XPS, K-alpha, SIGMA PROBE, Thermo Fisher

Scientific, UK) and photoemission spectroscopy at the beamline 10D in the Pohang Light Source (PLS-II) (Pohang, Republic of Korea). An elemental analyzer (Flash1112, Thermo Fisher Scientific, Germany) and inductively coupled plasma - mass spectrometry (ICP-MS, NexION 350D, Perkin-Elmer, USA) installed at the National Center for Inter-university Research Facilities (NCIRF) at Seoul National University was used to investigate the element contents.

3.2.3. Electrochemical characterization

A three-electrode cell was used to conduct half-cell experiments with an Autolab potentiostat and 0.1 M KOH and 0.5 M H_2SO_4 solution. Before experiments, the electrochemical cell components were cleaned by using a nitric acid solution and deionized water. A glassy carbon electrode was used as the counter electrode, and a 3.5 M Ag/AgCl electrode and a saturated calomel electrode were used as the reference electrodes. The glassy carbon electrode (electrode area: 0.196 cm^2) was polished with alumina to a mirror finish. The hydrogen oxidation reaction was conducted to convert the potentials to those for a reversible hydrogen electrode (RHE). For linear scan voltammetry of the ORR, the electrode was rotated at 1600 rpm and scanned at 10 mV s^{-1} with iR-correction using impedance measurements. The FeNCs and commercial Pt/C 20 wt% catalysts (Johnson Mattey Co., UK) were loaded at 700 and 400 μg cm^{-2}, respectively. The results of the rotating ring-disk electrode (RRDE) studies were calculated using a collection efficiency of 0.37 to obtain the electron transfer numbers. The H_2O_2 reduction reaction (PRR) activities were measured in Ar-saturated 0.1 M KOH electrolyte with 10 mM H_2O_2. The nitrite stripping experiment was performed in Ar-saturated 0.5 M acetate buffer with a pH of 5.2 in a scan rate of 10 mV s^{-1}.[10] We conducted long-term stability tests by cyclic voltammetry 0.6 V-1.0 V versus RHE for 10000 cycles.

3.2.4 Fabrication and single-cell test of AEMFCs and primary Zn-air battery

The membrane electrode assembly (MEA) of 5 cm^2 was fabricated using a catalyst, FAA-3-Br ionomer (FuMA-Tech Inc., Germany), isopropyl alcohol, and deionized water sprayed on an FAA-3-50 membrane (FuMA-Tech Inc., Germany). The membrane was pretreated with 1.0 M KOH solution for 1 h to exchange Br ions to OH ions. 60 wt% Pt/C (Johnson Matthey Co., UK) was used as the anode catalyst with a loading of 0.5 mg$_{Pt}$ cm^{-2}. As the cathode catalyst, the loading of FeNC-4000 and 20 wt% Pt/C was 1.0 mg$_{FeNC-4000}$ cm^{-2} and 0.5 mg$_{Pt}$ cm^{-2}, respectively. JNTG30-A3 (JNTG Co., Republic of Korea) was used as a gas diffusion layer. The single-cell test of AEMFC was conducted under a humidified H$_2$/O$_2$ condition at 60 °C with ambient pressure or 1.5 bar backpressure. The relative humidity of anode and cathode was 80 and 90%, respectively. The flow rates of H$_2$ and O$_2$ were 800 and 1000 ml min^{-1}, respectively.

A home-made Zn-air single cell was constructed using the Zn plate (250 μm, Alfa Aesar Co. USA) and the slurry with the catalyst, Nafion ionomer (Aldrich Chem. Co., USA), isopropyl alcohol, and deionized water. The prepared catalyst slurry was sprayed onto the gas diffusion layer (JNTG30-A3 (JNTG Co., Republic of Korea)) to achieve a loading of 4.0 mg cm^{-2}. 6 M KOH aqueous solution was used as the alkaline electrolyte. The single-cell test of the primary Zn-air battery was conducted at an operating temperature of 25 °C. The electrochemical impedance spectra (IM-6, ZAHNER-elektrik GmbH & Co. KG, Germany) were measured at a constant voltage of 1.1 V, ranged from 100 mHz to 100 kHz.

3.2.5 XAFS analysis

X-ray absorption fine structure (XAFS) was measured at 8C nano-probe XAFS beamline (BL8C) of Pohang Light Source (PLS-II) in the 3.0 GeV storage ring, with a ring current of 300 mA. The radiation source of BL8C is a tapered in-

vacuum-undulator. The X-ray beam was monochromated by a Si(111) double crystal, where the beam intensity was reduced by 30% to eliminate the higher-order harmonics. The X-ray beam was then delivered to a secondary source aperture, where the beam size was adjusted to be 0.5 mm (v) × 1 mm (h). XAFS spectra were collected in both transmission and fluorescence modes. The obtained spectra were processed using Demeter software. Extended X-ray absorption fine structure (EXAFS) spectra were fitted in a Fourier-transform range of 2-12 Å^{-1} with a Hanning window applied between 1 Å and 3 Å. The amplitude reduction factor (S_o^2) was set to be 0.8 during the fitting.

For *in situ* studies, a three-electrode cell with a carbon rod electrode and an Ag/AgCl electrode were constructed using a specifically designed *in situ* cell filled with N2-saturated 0.1 M KOH solution. After applying voltage, the *in situ* spectra were collected when the current is saturated.

3.3. Results and Discussion

3.3.1. Synthesis and physical characterization

The composite of Fe@C and Fe-N$_x$ site as the synergetic active site on carbon materials are designed and synthesized, as shown in Figure 3.1a. In the first step, the mixture of KB, polyol solvent, and Fe-phenanthroline complex were ignited. During combustion, polyol and oxygen from air act as a reducing and an oxidizing agent, respectively. Simultaneously, Fe-N moieties were influenced by both the reductive atmosphere due to locally decreased oxygen and the inflow of the oxidizing agent from the air.[9] Therefore, some Fe-N moieties were maintained on the carbon matrix, and the others formed iron oxide coated with carbon after pyro-reaction. The subsequent heat-treatment leads to phase change of iron oxide to iron nanoparticles.[11] After the first heat-treatment, acid-treatment was performed in diluted sulfuric acid to remove impurities, which was followed by second heat-treatment in Ar atmosphere. As the pyrosynthesis can be performed on a large scale, the FeNCs is obtained in a gram-scale, which is advantageous for mass production (Figure 3.2).

The samples collected after each process were investigated to validate the effect of the processes. The XRD spectra (Figure 3.3) and Fe 2p XPS spectra (Figure 3.4a) confirms that the sample after the pyro-synthesis was mainly composed of Fe$_3$O$_4$.[12] The pyrolysis process conducted on an open-air condition broke the Fe-N bonding in some Fe-Phen complex and oxidized Fe ions into iron oxides. The iron oxides produced from pyro-synthesis have a relatively uniform and small size, as shown in Figure 3.5. The high thermal energy from the combustion of polyol provokes burst nucleation that is critical for the synthesis of uniform and small-sized nanoparticles.[13] The iron oxides coated with a thin carbon shell, which comes from the carbon source, TTEG and phenanthroline. Since the short process time and the trade-off effects prevent the Fe-N complex from combustion reaction, the rest of Fe

96
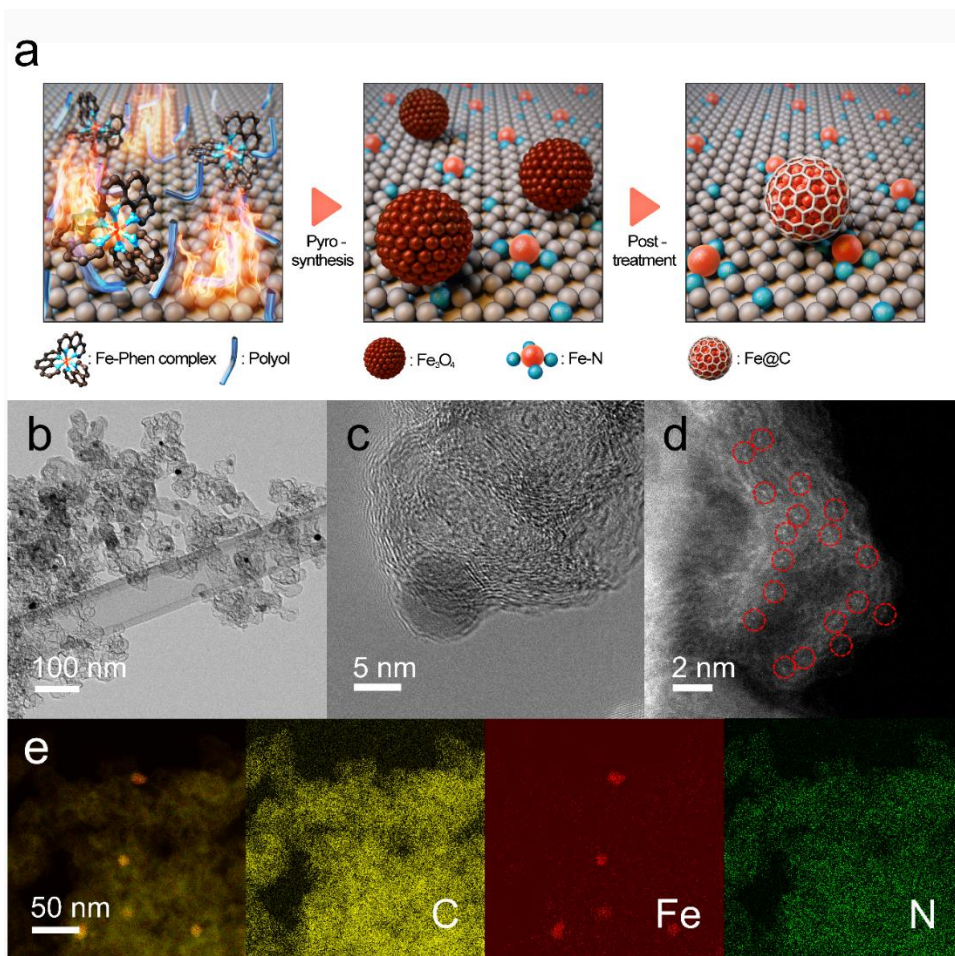
Figure 3.1. (a) Preparation of FeNCs. (b-c) TEM images of FeNC-4000. (d) STEM image of FeNC-10000. EDS mapping images of (d) the merged, (e) C (yellow), Fe (red), and N (green) elements of FeNC-4000.

Figure 3.2. Gram-scale weight after synthesis of FeNC-4000.
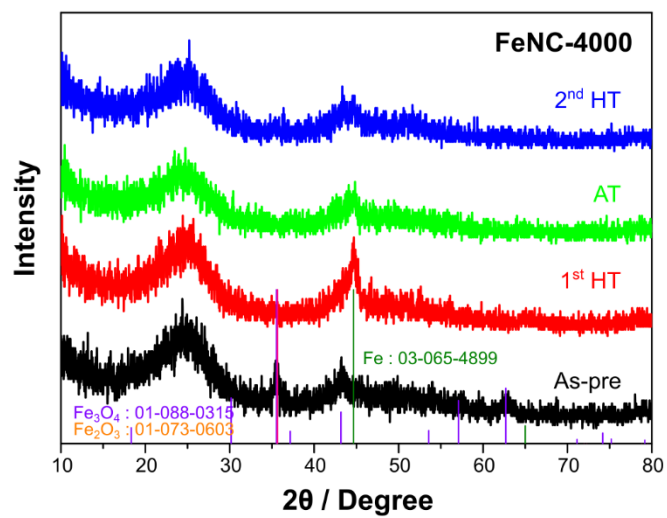
Figure 3.3. XRD patterns of FeNC-4000 after each process.
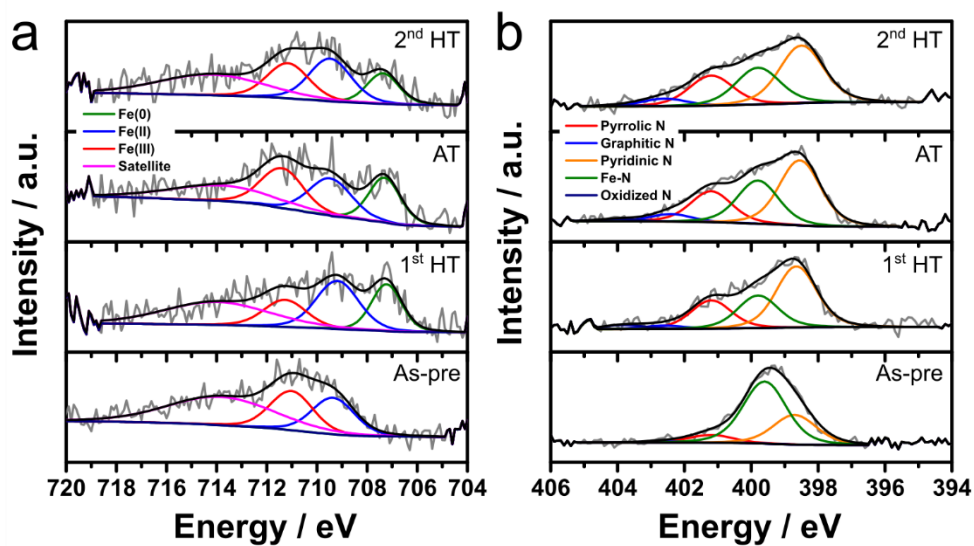
Figure 3.4. (a) Fe 2p and (b) N 1s XPS spectra of FeNC-4000 after each process.
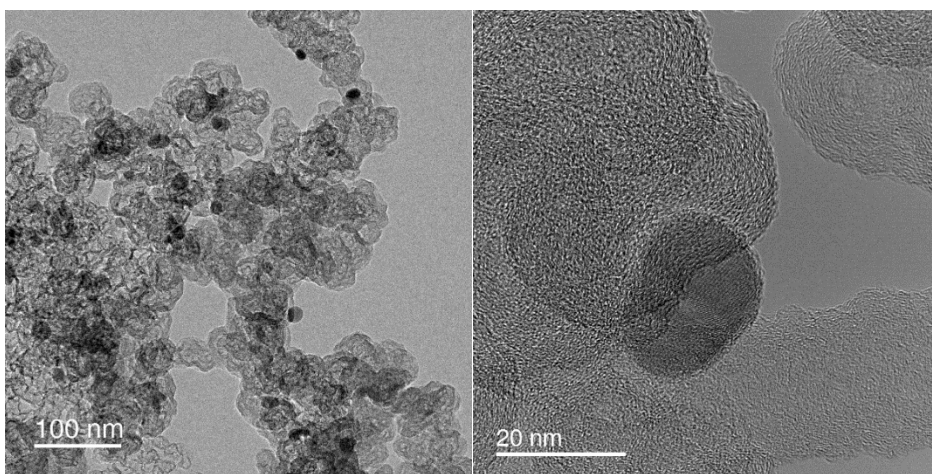
Figure 3.5. TEM images of FeNC-4000 after pyrosynthesis.

sources maintains Fe-N bonding according to N 1s XPS spectra (Figure 3.4b).[14,15] During the first heat treatment under an inert atmosphere, the iron oxides are reduced to iron nanoparticles due to oxidization of surrounding carbon that removes an oxygen anion of iron oxide and offers extra electron to Fe ion.[16] It is proved by the newly generated peak in the XRD spectra (Figure 3.3) and peak at 707 eV in Fe 2p XPS spectra (Figure 3.4a), which represents the existence of Fe metallic phase.[12] After acid treatment, the dominant Fe peak at 44 ° decreased in the XRD spectra, which indicates that the uncoated or partially coated Fe particles are eliminated. The oxidized carbon surface was reduced by second heat treatment without further production of iron particles, shown in the XRD spectra. Even after a series of post-treatments, further agglomeration of Fe particles is not detected, as shown in Figure 3.1b. It is regarded that the carbon shell on the nanoparticles synthesized during pyro-synthesis acts as a stabilizer of nanoparticles and impedes the agglomeration or Ostwald ripening.[17]

The FeNC-NoPyro was prepared by omitting the pyro-synthesis step to investigate the effect of pyro-reaction on catalyst structures. In TEM images of FeNC-NoPyro (Figure 3.6a-b), nanoparticles in the size of 5-30 nm were detected, which indicates the irregular and excessive agglomeration during annealing. Moreover, when compared to the pyro-synthesized sample, the nanoparticles of FeNC-NoPyro are indexed to two phases, iron carbide and iron in the XRD spectra (Figure 3.6c), resulting from the strong reduction atmosphere and excessive carbon source. These different properties are attributed to lower ORR activity of FeNC-NoPyro than that of samples synthesized through pyro-synthesis (Figure 3.6d). It is worth mentioning that the combustion of polyol during pyro-synthesis provides enough energy to nucleate iron oxides, and the short process time of pyro-synthesis limits further growth and phase transition of iron oxides. Moreover, the carbon shell synthesized from pyro-synthesis prevents nanoparticles from further growth and
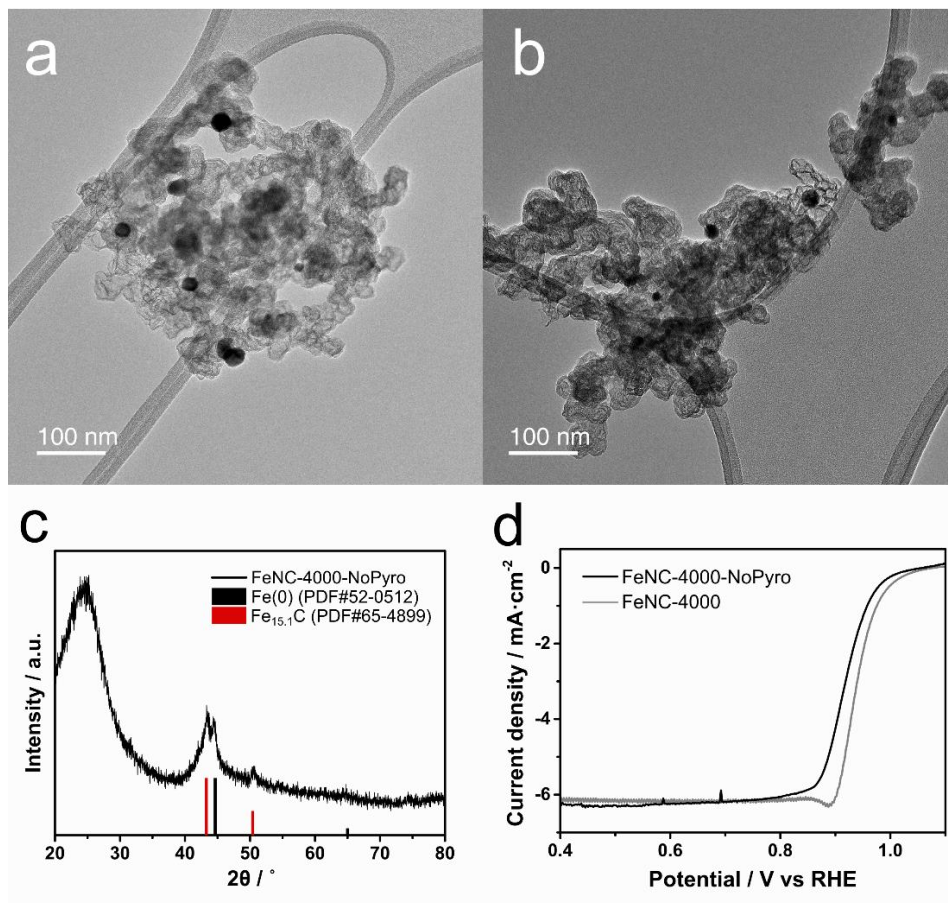
Figure 3.6. (a-b) TEM images and (c) XRD spectra of FeNC-NoPyro.

Ostwald ripening. Therefore, the pyro-synthesis is an effective strategy for synthesizing uniform and small-sized nanoparticles, which gives a large area to catalyze the reactant.

To optimize the ratio between single atom $Fe-N_x$ sites and carbon-shell-coated iron nanoparticles, we prepared the sample set with the same amount of Fe and N precursor, but a different amount of KB. The materials are named by the weight of KB (unit: mg) used in the synthesis. The morphology of the materials synthesized with different amounts of KB was observed using TEM, as shown in Figure S6. The carbon layer in the nanometer-size is synthesized, encapsulating the iron nanoparticles (Figure 3.1c). The EDS images confirm that the nanoparticles consisted of iron and the evenly distributed nitrogen on the carbon matrix (Figure 3.1e). The amount of KB controls the size and distribution of carbon-shell-coated iron nanoparticles (Figure 3.7). In particular, the mean size of Fe nanoparticles in FeNC-600, FeNC-2000, and FeNC-4000 is 18.9 nm, 14.1 nm, and 11.0 nm, respectively. The increase of KB amount provides the larger area for a nucleation site of iron nanoparticles, and thus, results in the decrease of particle sizes. In specific, nanoparticles are rarely detected in FeNC-10000. Instead, cs-STEM images of FeNC-10000 in Figure 3.1d and 3.8c exhibit the presence of single iron atoms.[18] It proves that the spare density of the Fe-N complex in FeNC-10000 with a large KB amount prevents the generation of Fe nanoparticles secures Fe-N bonding on the carbon matrix. Moreover, the co-existence of single iron atom sites and carbon-shell-coated iron nanoparticles is confirmed by the cs-STEM image of FeNC-4000 (Figure 3.8a,b).

The composition and phase of the materials are investigated using XRD (Figure 3.9a). FeNC-600 and FeNC-2000 show the dominant peak at 44 ° indexed to the iron (0) (JCPDS 03-065-4899) and also peaks indexed to the iron nitride (JCPDS 01-078-2127). FeNC-4000 and FeNC-10000, however, do not exhibit any
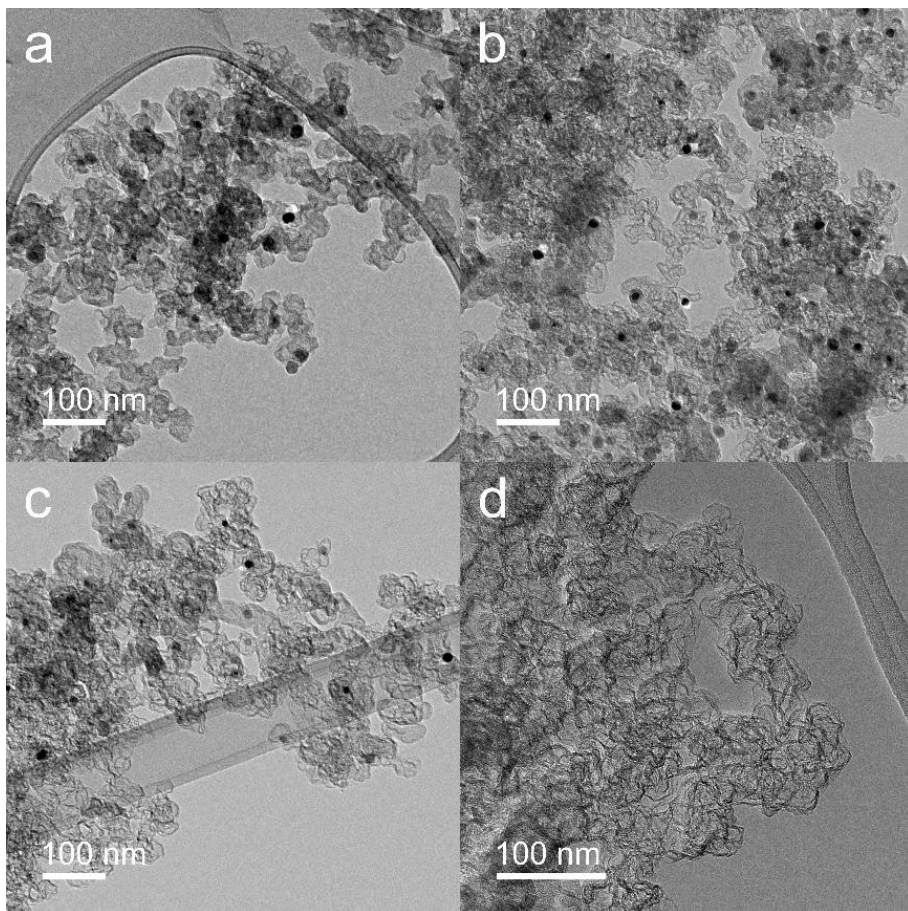
Figure 3.7. TEM images of (a) FeNC-600, (b) FeNC-2000, (c) FeNC-4000, and (d) FeNC-10000.
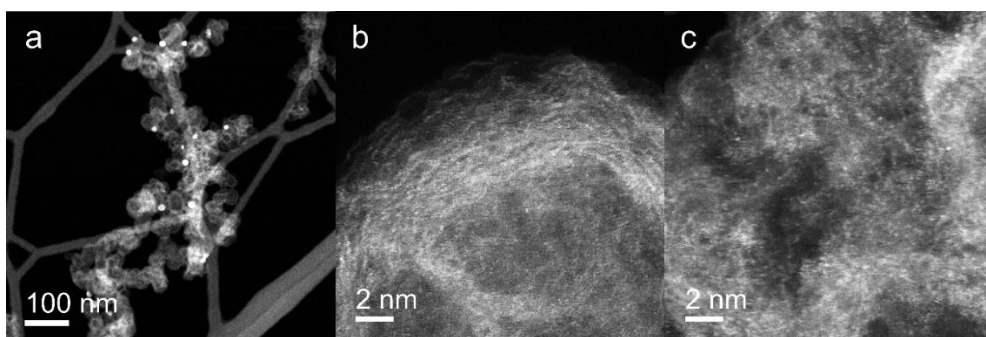
Figure 3.8. STEM images of (a,b) FeNC-4000 and (c) FeNC-10000.
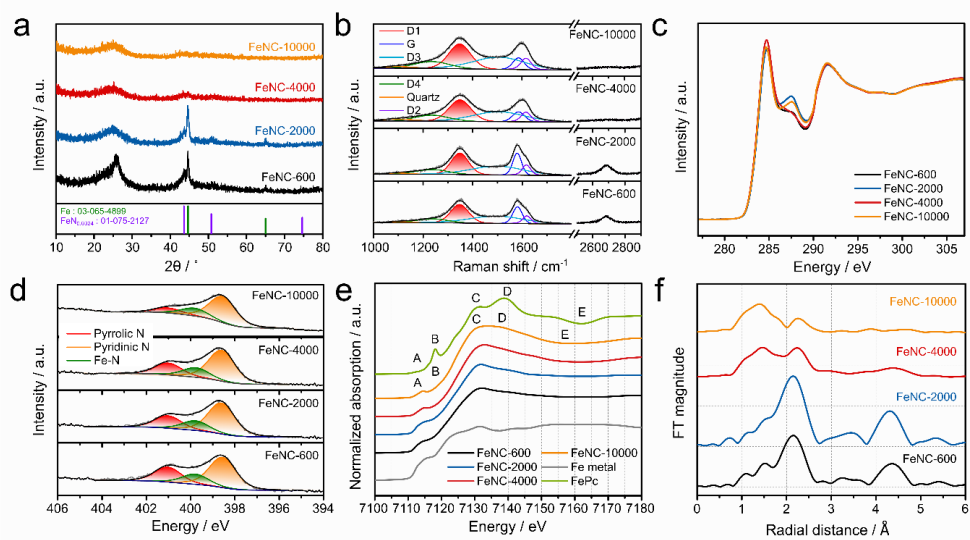
Figure 3.9. Structural information for FeNCs. a) XRD, b) Raman, c) C K-edge NEXAFS, and d) N 1s PES spectra of the FeNCs. e) XANES and f) FT-EXAFS spectra of the FeNCs.

evident peak associated with Fe. It is ascertained that the amount of Fe in FeNCs is reduced with the increase of KB amount by the ICP and EA analysis (Table 3.1 and 3.2).

The peak at ~25 ° associated with carbon consists of peaks for the amorphous structure (γ-band) and the crystallite carbon ((002) band) (Figure 3.10), which provides the average lattice parameters of graphitic carbon calculated from the Bragg's and Scherrer equation.[19] Since Fe is well-known as a catalyst graphitizing carbon materials,[5] the different amounts and sizes of Fe nanoparticles can influence the properties of carbon differently in each sample. In practice, the sample with high Fe content exhibits high carbon crystallite height and a large number of carbon layers per crystallite (Table 3.3).[19] It corresponds to the thickness of the carbon coating layer on Fe nanoparticles, as shown in the TEM image of FeNC-600, FeNC-2000, and FeNC-4000 (Figure 3.11 and Figure 3.1c). The larger diameter of Fe particles induces the generation of more carbon layers over them during the encapsulation of Fe particles by carbon.[20] The increase in the thickness of carbon coating hinders the electron tunneling from Fe. It offsets the effect of Fe that reduces the dissociative adsorption energy of oxygen.[21] Therefore, the FeNC with the thinner carbon coating, FeNC-4000, is expected to exhibit high electrocatalytic activity.

Raman spectroscopy is also used to investigate the characteristic of carbon in the materials (Figure 3.9b). With increasing Fe content in the materials, the peaks for the G band at ~1580 cm^{-1} are enhanced, which exhibits a high degree of graphitization.[22] In particular, the area of the deconvoluted G-band of FeNC-600 and FeNC-2000 is larger than that of FeNC-4000 and FeNC-10000, and even that of KB (Table 3.4). Moreover, the peak for a 2D band at 2700 cm^{-1} exists only at the spectrum of FeNC-600 and FeNC-2000. It indicates that high Fe content results in The excessive graphitization of carbon during synthesis, associated with a high

Table 3.1. Elemental content of iron in KB and FeNCs from ICP.

Sample	Iron (wt%)
KB	0.01
FeNC-600	6.64
FeNC-2000	5.68
FeNC-4000	3.70
FeNC-10000	1.53

Table 3.2. Elemental contents in FeNCs from elemental analysis. (unit: wt%)

Sample	Carbon	Nitrogen	Hydrogen
FeNC-600	83.8	2.76	0.400
FeNC-2000	86.3	2.54	0.431
FeNC-4000	88.4	3.14	0.433
FeNC-10000	91.8	2.45	0.413
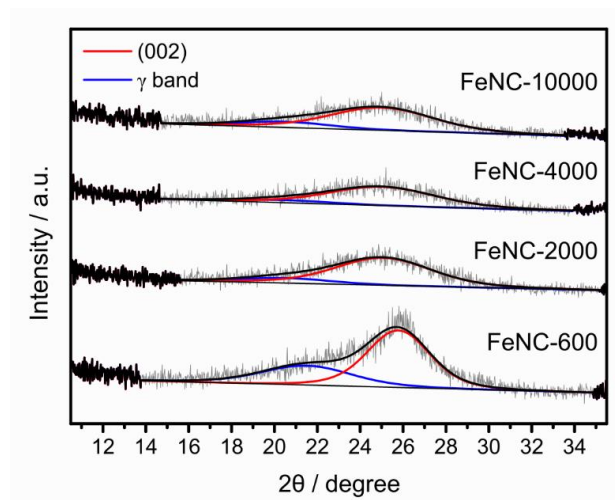
Figure 3.10. Deconvoluted XRD spectra of FeNCs.

Table 3.3. Deconvoluted peak of XRD spectra for FeNCs.

Sample	2theta / °	FWHM / nm	crystalline height / nm	Interlayer spacing between aromatic layers / nm	Number of aromatic layer per carbon crystalline (N)
600	25.78	3.45	2.33	0.345	7.76
2000	25.07	5.30	1.52	0.355	5.28
4000	25	5.85	1.38	0.356	4.87
10000	25	5.67	1.42	0.356	4.99
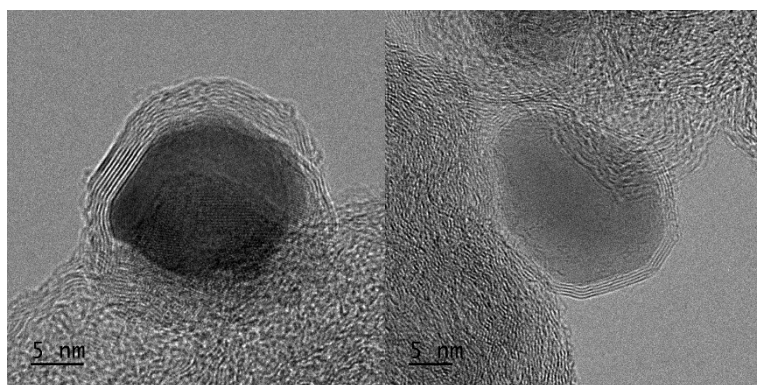
Figure 3.11. TEM images of carbon coated Fe nanoparticles in (a) FeNC-600 and (b) FeNC-2000.

Table 3.4. Deconvoluted peak area of FeNCs from Raman spectra. (unit: %)

Sample	D1	G	D2	D3	D4	Quartz	FWHM of D1
KB	30.7	9.9	4.3	34.7	17.2	3.2	96.1
FeNC-600	30.6	14.4	6.2	35.6	11.3	1.9	85.4
FeNC-2000	28.7	14.7	7.1	35.6	11.8	2.0	82.7
FeNC-4000	32.4	8.1	6.9	34.9	13.4	4.4	105
FeNC-10000	31.8	7.8	7.3	36.7	13.6	2.8	104

height of carbon crystallite in FeNC-600 and FeNC-2000.

The electronic properties of carbon in FeNCs are investigated using the C K-edge spectra of NEXAFS (Figure 3.9c). The predominant peak at ~285 eV represents the transition of an electron from C 1s to π^* states, and the spectrum of FeNC-4000 only exhibits the increased intensity of the peak. The increased π^* signals can result from the incorporation of heteroatom into C and close contact at the interface of metal and C due to the electronic interaction between C and other elements.[23,24] From the DFT calculation, the electronic interaction between C and metal is enhanced when the carbon coating on the metal is thinner, which results in the increased π^* signals and promotes the adsorption of oxygen, and thus, ORR.[23a] Therefore, the highest intensity of π^* signals in FeNC-4000 exhibits the enhanced interaction between thin carbon coating and Fe nanoparticles, which can enhance ORR activity.

The difference in the ratio between the Fe-N complex and KB affects the chemical stats of the final products. Figure 3.9d shows the N 1s photoemission spectroscopy (PES) spectrum at 600 eV of FeNCs using synchrotron radiation sources. The spectra are used to identify three N configurations, corresponding to pyridinic N (398.6 eV), N in Fe-N bonding (399.8 eV), and pyrrolic N (401 eV).[14,15] As the KB increases, the content of pyridinic N also increases, while that of pyrrolic N decrease (Table 3.5). In specific, the content of pyridinic and N in Fe-N bonding on FeNC-10000 are notably higher than other FeNCs. More dispersed Fe-N complexes enable to maintain their structure during synthetic processes, which leads to a high proportion of pyridinic N and N for Fe-N bonding in samples with the high content of KB. Thus, controlling the ratio between KB and Fe-N complex is attributed to the unique properties of each sample.

The structure and local geometry of Fe sites in FeNCs were investigated by obtaining synchrotron-based X-ray absorption fine structure (XAFS). The X-ray

115

Table 3.5. Atomic ratio of N configurations of FeNCs from PES analysis. (unit: %)

Nitrogen	Pyrrolic N	Pyridinic N	Fe-N
FeNC-600	26.8	54.8	18.4
FeNC-2000	23.3	58.5	18.2
FeNC-4000	22.6	59.0	18.4
FeNC-10000	12.9	67.0	20.1

absorption near edge structure (XANES) spectra represents the characteristic features generated from materials with Fe-centered macrocycles when compared to iron phthalocyanine (FePc) with a square planar Fe-N$_4$ structure.[25] In Figure 3.9e, pre-edge peak (feature A, 1s $\rightarrow$ 3d dipole forbidden transition) increases with decrease in the amount of KB while feature B, 1s $\rightarrow$ 4p$_z$ shakedown transition which is a fingerprint of square-planar Fe-N$_4$ structure, disappears in all FeNCs indicating that the square-planar Fe-N$_4$ structure of FeNCs is severely distorted and metallic Fe character dominates as the amount of KB decreases. Features C, D, and E are responsible for 1s to 4p$_{x,y}$ transition, multiple scattering, beginning of first shell scattering, respectively. For FeNC-10000, the intensity ratio of features C and D (Ic/Id) increases, and the position of feature E shifts to lower energy compared to FePc indicates that Fe-N bond distance increases.[25] The corresponding Fourier transformed (FT) extended X-ray absorption fine structure (EXAFS) spectra provide more intuitive data regarding the local structure of Fe in FeNCs (Figure 3.9f). The peaks at ~2.2 Å and ~4.3 Å for the Fe-Fe bonding are dominant in the spectra for FeNC-600 and FeNC-2000. Meanwhile, Fe-N/O bonding at ~1.5 Å and Fe-C bonding at ~2.3 Å are noticeable as the number of KB increases.[26] as expected. Both XANES and EXAFS spectra for FeNC-4000 shows that the amounts of Fe metallic phase and Fe-N bonding are comparable in FeNC-4000. From the above analysis, the physicochemical analysis for FeNCs proves that the Fe@C/Fe-N$_x$ ratio is successfully controlled in our system.

3.3.2. Electrochemical characterization

The electrocatalytic activities of the materials are evaluated using a three-electrode system. The different ratio of Fe and KB clearly affects the FeNC's performance, as shown in Figure 3.12a. Based on the ORR curves in an alkaline electrolyte, the half-wave potentials for FeNC-600, FeNC-2000, and FeNC-4000 are

0.868 V, 0.917 V, and 0.941 V, respectively (Figure 3.12b). From FeNC-600 to FeNC-4000, the activities increase with the increase of KB content. However, FeNC-10000 ($E_{1/2}$: 0.910 V) shows less activity than that of FeNC-4000. In particular, FeNC-4000 exhibits superior activities among the prepared catalysts and even compared to the previously reported non-precious metal catalysts so far (Table 3.6). Moreover, the kinetic current densities of FeNCs are notably higher than the previous reports, indicating the superiorities of the catalyst system that is designed to contain both Fe-N$_x$ and Fe@C as the synergetic active site.

The electron transfer numbers of FeNC-4000 were calculated by the Koutecky-Levich equation using linear sweep voltammetry curves at different rotating rates. The numbers are over 3.9 at 0.6, 0.7, 0.8, and 0.85 V, which indicates the high selectivity of FeNC-4000 toward 4-electron pathway ORR (Figure 3.13). In OER activities, the samples show identical trends with the ORR activities of materials (Figure 3.14). Therefore, the oxygen activities calculated using half-wave potentials in ORR curves and the potentials at 10 mA·cm^{-2} in OER curves also exhibit the same trends. In an acid electrolyte, FeNC-4000 exhibits the highest ORR performance among FeNCs, which is also superior to the reported non-precious metal catalysts (Figure 3.15 and Table 3.7). FeNC-10000 shows enhanced performance than that of an alkaline electrolyte when compared to other FeNCs since the Fe-N$_x$ sites have a higher selectivity for catalyzing 4-electron ORR than Fe@C in an acid electrolyte.[27] The durability of FeNC-4000 is examined by comparison between ORR curves before and after 10000 cycles of CV. While commercial Pt/C catalysts exhibit a decrease in the half-wave potential of 24 mV, FeNC-4000 shows that of 12 mV, indicating its high durability (Figure 3.16).

As the quantitative analysis for Fe-N$_x$ sites on each sample, the electrochemical experiments using nitrite anion (NO$_2^-$), the strong adsorbates on the Fe^{2+}-N site, were performed (Figure 3.17).[28] Since the site-specific adsorption of the
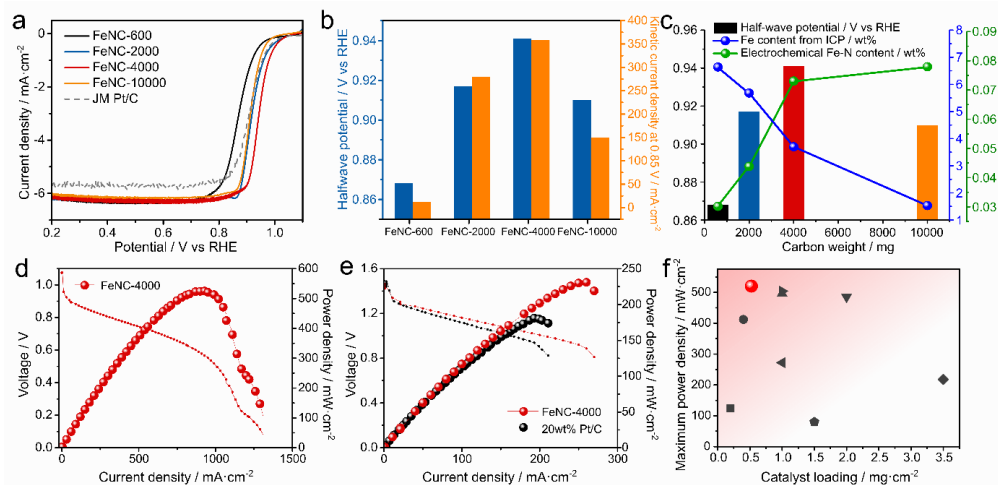
Figure 3.12. Electrochemical analysis of FeNCs. a) Linear sweep voltammogram curves at a scanning rate of 10 mV s^{-1} in O$_2$-saturated 0.1 m KOH solution with *iR* correction. b) Half-wave potential and kinetic current density at 0.85 V from ORR curves of FeNCs. c) Relationships between electrocatalytic performances and material properties. d) Polarization curves of AEMFCs prepared with FeNC-4000 (0.5 mg cm^{-2}) as cathode materials. e) Performance of primary Zn-air batteries prepared with FeNC-4000 and Pt/C (4.0 mg cm^{-2}) as cathode materials. f) The comparison of AEMFC performances with non-precious metal catalysts reported in literature (gray figures) and in this work (red circle).

119

Table 3.6. Comparison of non-platinum group ORR catalysts in 0.1 M KOH alkaline electrolyte.

Catalyst	Half-wave potential (V vs RHE)	Kinetic current density at 0.85 V (mA·cm^{-2})	reference
Fe/N/C	0.930	-	ACS Catal. 2017, 7, 10, 6485
FeCl1N4/CNS	0.921	41.11	Energy Environ. Sci., 2018, 11, 2348
Fe-SAs/NPS-HC	0.912	71.9	Nat. Comm. 2018, 9, 5422
Fe-ISA/SNC	0.896	100.7	Adv. Mater. 2018, 30, 1800588
*pf*SAC-Fe-0.2	0.91	25.86	Sci. Adv., 2019, 5, eaaw2322
Fe-N-C-900	0.927	28	Adv. Energy Mater. 2018, 8, 1801956
Fe SAs/MC(950)	0.902	8.2	ACS Energy Lett. 2018, 3, 10, 2383
Cu-SA/SNC	0.893	22.0	Energy Environ. Sci., 2019,12, 3508
Fe-N/CNT-2	0.938	-	Adv. Funct. Mater. 2019, 29, 1906174
Fe-N/P-C-700	0.867	24.49	J. Am. Chem. Soc. 2020, 142, 5, 2404
FeNC-4000	**0.941**	**358**	**This study**
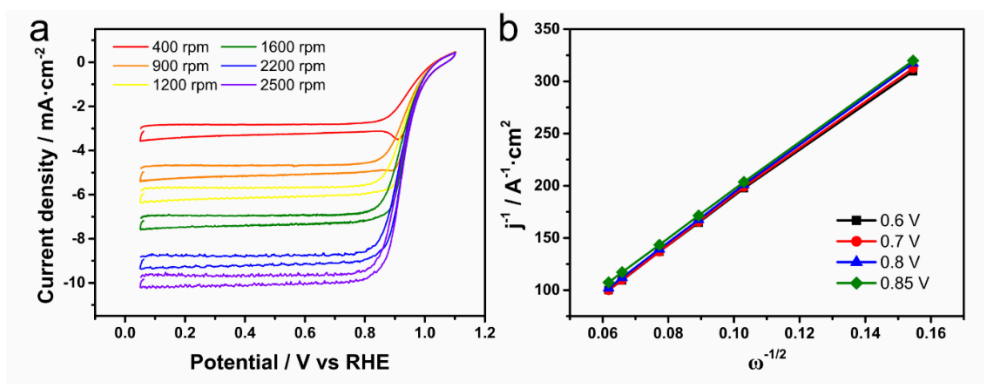
Figure 3.13. (a) Linear sweep voltammogram curves of FeNC-4000 at different rotation speeds and (B) Koutecky-Levich plots obtained from (a) at different potentials.

Figure 3.14. Linear sweep voltammogram curves of FeNCs at a scanning rate of 10 mV s^{-1} in O$_2$-saturated 0.1 M KOH solution with iR correction.
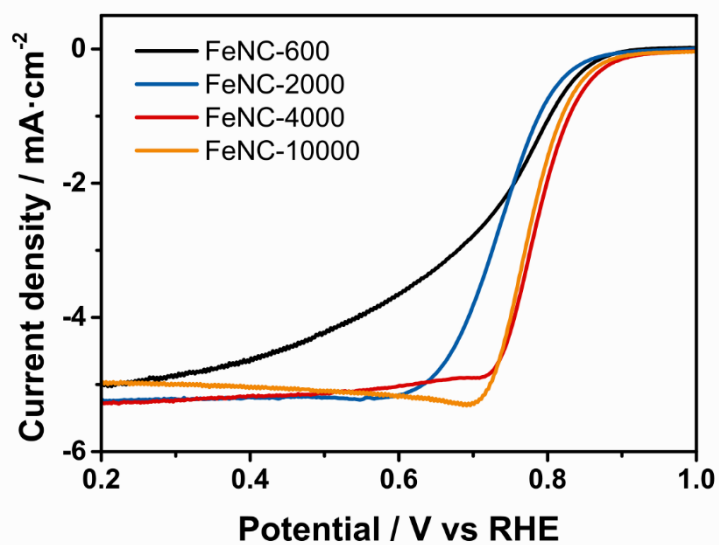
Figure 3.15. Linear sweep voltammogram curves of FeNCs at a scanning rate of 10 mV s^{-1} in O$_2$-saturated 0.5 M H$_2$SO$_4$ solution with *iR* correction.
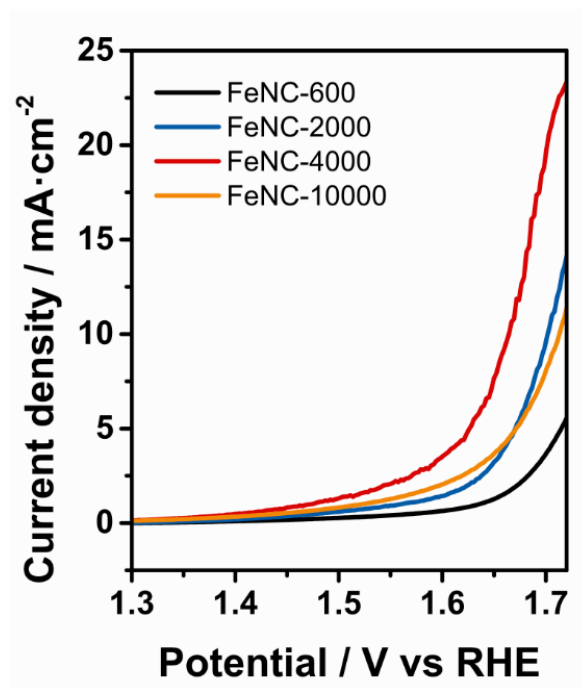
Table 3.7. Comparison of non-platinum group ORR catalysts in acid electrolyte.

Catalyst	Half-wave potential (V vs RHE)	Electrolyte	Kinetic current density ($mA·cm^{-2}$)	reference
SA-Fe/NG	0.8	0.5 M H_2SO_4	15.6 at 0.75 V	Proc. Natl. Acad. Sci. U. S. A., 2018, 115, 6626
FeSAs/NPS-HC	0.791	0.5 M H_2SO_4	18.8 at 0.85 V	Nat. Commun., 2018, 9, 5422
Fe_2–N–C	0.78	0.5 M H_2SO_4	2.89 at 0.8 V	Chem, 2019, 5, 2865
C-FeZIF-1.44-950	0.78	0.1 M $HClO_4$		Adv. Energy Mater., 2019, 9, 1802856
Fe/SNC	0.77	0.5 M H_2SO_4	~25 at 0.73 V	Angew. Chem., Int. Ed., 2017, 56, 13800
Pt_1–N/BP	0.76	0.1 M $HClO_4$		Nat. Commun., 2017, 8, 15938
A-CoPt-NC	~0.75	0.1 M $HClO_4$		J. Am. Chem. Soc., 2018, 140, 10757
FeNC-4000	0.784	0.5 M H_2SO_4	22.9 at 0.75 V 3.05 at 0.8 V	This study

nitrite anion is assured, the reduction charge of nitrosyl moiety bonded with the Fe^{3+} can be used to quantify the number of $Fe-N_x$ sites.[10] The stripping charge from the nitrite stripping experiment is increased from FeNC-600 to FeNC-10000, as shown in Figure 3.12c and 3.17, and Table 3.8. It is attributed to the extended space for the $Fe-N_x$ site with an increasing KB amount compared to the Fe-N complex during synthesis. Therefore, FeNC-600 and FeNC-2000 possess a low density of $Fe-N_x$ site and high amount of Fe@C, which leads to the significant effect of Fe@C than $Fe-N_x$ site in electrochemical characterization. On the other hand, FeNC-4000 consists of high density of $Fe-N_x$ site and Fe nanoparticles coated with thin carbon layer, while FeNC-10000 has high density of $Fe-N_x$ site and low Fe content. This result is consistent with the result from EXAFS data, which confirms the controlled active sites in FeNCs as designed.

The difference in the electrocatalytic properties between FeNCs is examined using H_2O_2, as shown in Figure 3.18a. The high PRR activities are required for ORR catalysts to convert the intermediate, HO_2^- (the dominant form of H_2O_2 in high pH), to the targeted product, OH^-, and prevent the degradation of catalysts. The PRR activities measured in Ar-saturated 0.1 M KOH solution with 10 mM H_2O_2 are notably high in FeNC-2000 and FeNC-4000, the Fe@C contained samples. It corresponds to the research that Fe@C stabilizes the intermediate and promotes the reduction of intermediate into OH^-.[6] Moreover, the PRR activity of FeNC-4000 is higher than that of FeNC-2000 with more Fe content, which indicates that the appropriate ratio of Fe@C and $Fe-N_x$ sites also leads to effective PRR. In the RRDE studies with the reduced catalyst loading ($100\ \mu g \cdot cm^{-2}$) (Figure 3.18b), the peroxide yields of each sample were calculated to investigate the production of intermediate. Since the consecutive reduction of O_2 ($O_2 \rightarrow HO_2^- \rightarrow OH^-$) is hard due to low catalyst loading, a small amount of peroxide produced from the samples with the mixed active sites is ascribed to efficient 4 electron ORR and the stabilization effect of

125
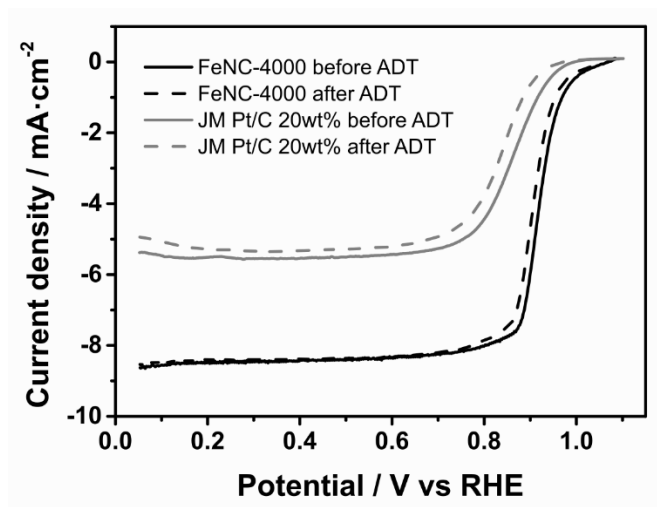
Figure 3.16. Linear sweep voltammogram curves of FeNC-4000 and JM Pt/C 20 wt% in 0.1 M KOH before and after ADTs.
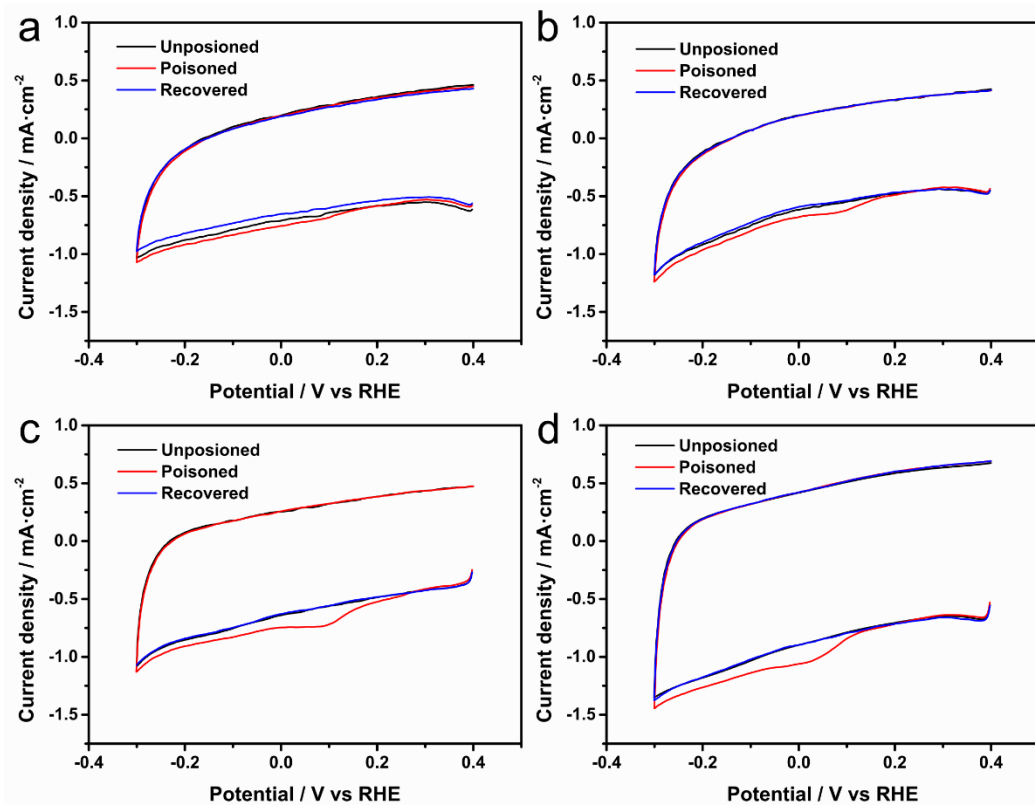
Figure 3.17. Cyclic voltammogram curves in the nitrite reductive stripping region before, during and after nitrite adsorption for (a) FeNC-600, (b) FeNC-2000, (c) FeNC-4000, and (d) FeNC-10000.

127

Table 3.8. Parameters of Fe-N denisty calculated from the nitrite stripping experiment.

Sample	Nitrite stripping charge / C g^{-1}	Site density / μmol g^{-1}	Fe-N weight in catalyst from nitrite stipping / wt%
FeNC-600	2.60	5.39	0.0302
FeNC-2000	3.78	7.83	0.0438
FeNC-4000	6.30	13.1	0.0731
FeNC-10000	6.72	13.9	0.0779
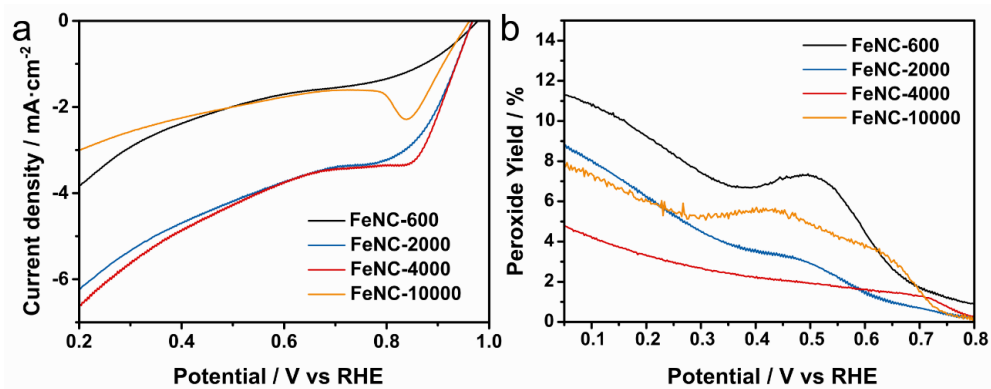
Figure 3.18. (a) Linear sweep voltammogram curves of FeNCs in 0.1 M KOH with 10 mM H_2O_2. (b) Peroxide yields of FeNCs with a loading of 100 $\mu g \cdot cm^{-2}$ ascertained from RRDE ring currents in 0.1 M KOH.

129

Fe@C. Therefore, the excellent ORR performance of the sample with the mixed active sites is attributed to the predominant ORR via the $4e^-$ pathway and the efficient PRR activities to produce more product from the intermediate.

The electrochemical performance and the Fe status of FeNCs are summarized in Figure 3.12c. Increasing the amount of KB decreases the Fe content in FeNCs, leading to a decrease in Fe@C content. It results in decreasing the size of Fe nanoparticles and the thickness of carbon coating. Moreover, the density of the Fe-N_x site is increased with the decrease of Fe content. Therefore, the FeNCs with high Fe content, FeNC-600 and FeNC-2000, are considered as consisting of predominantly Fe@C. In particular, despite the higher Fe content of FeNC-600, FeNC-2000 exhibits higher ORR activity, which is the effect of smaller Fe nanoparticles and a thinner carbon coating layer on Fe@C. The higher ORR activity of FeNC-4000 than that of FeNC-2000 is contributed to a larger number of Fe-N_x site. On the other hand, FeNC-10000 possesses the lowest Fe content but the highest Fe-N_x content, exhibiting decent ORR activity. Therefore, FeNC-4000 exhibits the synergetic effect of high Fe-N_x site density comparable to FeNC-10000 and high content of Fe@C with the thinnest carbon layer. The amount of Fe content in FeNC-4000 is not too high to create large Fe particles and hence generate excessive carbon shell layers, but enough to stabilize the intermediate during ORR. Hence, the appropriate ratio of Fe@C/Fe-N_x leads to the outstanding ORR activity of FeNC-4000.

Single-cell tests of AEMFCs with FeNC-4000 as cathode catalysts are employed to prove its viability to the practical applications. In Figure 3.12d, the maximum power density of AEMFCs for FeNC-4000 with a loading of 0.5 mg·cm^{-2} is 526 mW·cm^{-2} under 1.5 bar backpressure, which is the most excellent performance in AEMFCs using the non-precious metal catalysts and the commercial membrane (Table 3.9). In particular, it is notable that the high performance of FeNC-4000 is

achieved using lower catalyst loading compared to other reports, attributed to excellent intrinsic activity (Figure 3.12f). AEMFCs for FeNC-4000 with different loadings were also performed, indicating that the optimum loading is 0.5-1.0 mg·cm^{-2} due to enough active sites and facile mass transfer (Figure 3.19 and 3.20). The AEMFC performance using FeNC-4000 exceeds that of commercial platinum catalysts even with the same loading weight (Figure 3.21a). In the Nyquist plot at the current density of 0.1 mA·cm^{-2} (Figure 3.21b), AEMFC with FeNC-4000 shows lower ohmic resistance than those of platinum catalysts, resulting from thinner catalyst layer of FeNC-4000 as shown in Figure 3.22. Since the charge-transfer resistance correlates the intrinsic catalytic activity, the lower charge-transfer resistance of FeNC-4000 compared to the platinum catalyst corresponds to its high ORR activity in the half-cell experiment.

As the other practical application where ORR is crucial, Zn-air batteries with FeNC-4000 and platinum catalysts were constructed. In Figure 3.12e, the maximum power density of primary Zn-air battery with FeNC-4000 is 231 mW·cm^{-2}, while that of platinum catalysts is 180 mW·cm^{-2}, when the same amount of catalysts were loaded. The Nyquist plot obtained at a constant voltage of 1.1 V (Figure 3.23) exhibits lower charge-transfer resistance of FeNC-4000 than that of platinum, ascribed to the better intrinsic catalytic activity of FeNC-4000.

4.3.3. *in situ* XAFS analysis

The change of structure and oxidation state on Fe-based site during electrochemical operation are investigated by performing *in situ* XAFS analysis. The XAFS spectra were obtained when the constant voltage was applied to the FeNCs electrode in 0.1 M KOH solution, and the applied voltages were determined by using the ORR curves of the catalysts. In Figure 3.24a, the white line of XANES spectra for FeNC-4000 increases its intensity, and the main edge shifts to higher energies as
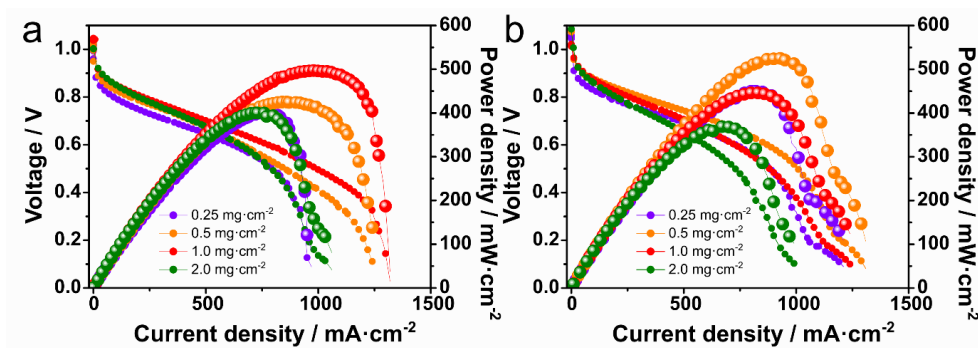
Figure 3.19. Polarization curves of AEMFCs prepared with different catalyst loadings of FeNC-4000 (a) at ambient pressure and (b) at 1.5 bar backpressure under humidified H_2/O_2 atmosphere. The ionomer content in cathode was 40 wt%, and 60 wt% Pt/C was used as anode catalyst with a loading of 0.5 $mg_{Pt} \cdot cm^{-2}$.
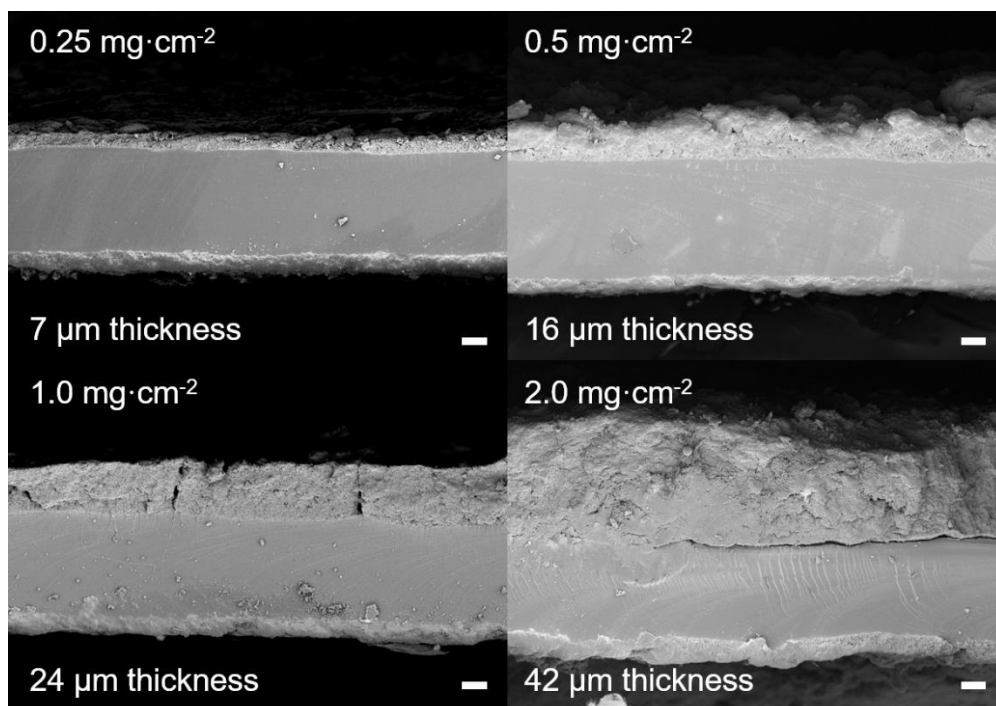
Figure 3.20. FE-SEM images of cross-sections of MEAs with different catalyst loadings of FeNC-4000. The scale bar is 10 μm.
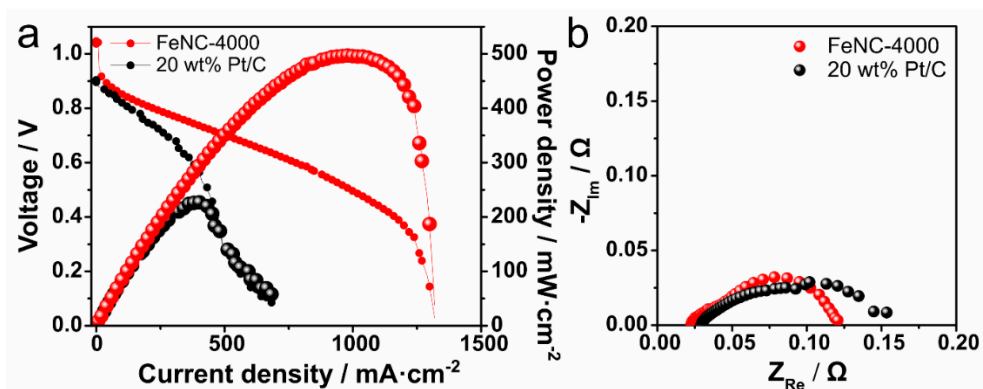
Figure 3.21. (a) Polarization curves and (b) Nyquist plots obtained at constant current density of 0.1 mA cm^{-2} of AEMFCs prepared with FeNC-4000 and 20 wt % Pt/C as cathode catalyst under humidified H$_2$/O$_2$ atmosphere. The catalyst loading was 1.0 mg$_{FeNC-4000/Pt}$ cm^{-2} and 60 wt% Pt/C was used as anode catalyst with a loading of 0.5 mg$_{Pt}$·cm^{-2}.
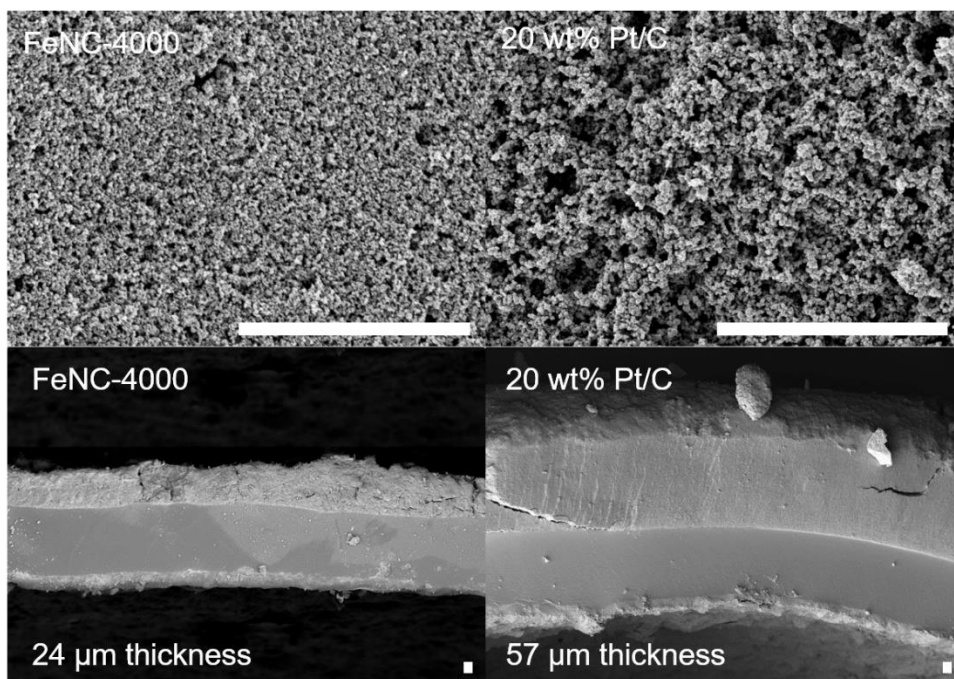
Figure 3.22. FE-SEM images of cross-sections of MEAs with FeNC-4000 and 20 wt% Pt/C. The catalyst loading was 1.0 mg cm^{-2}. The scale bar was 5 μm.
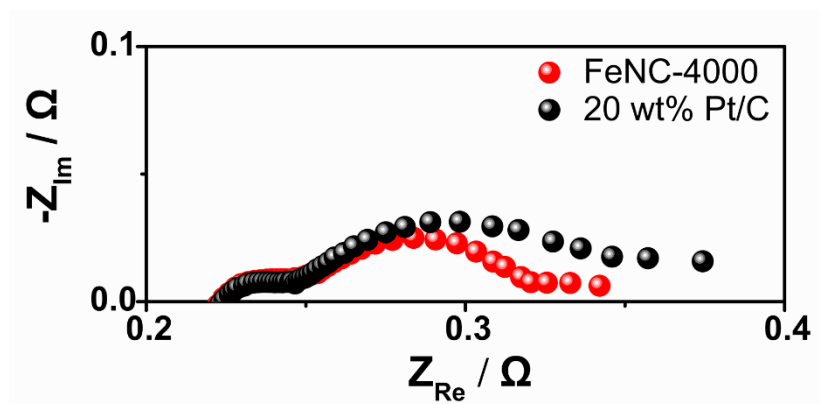
Figure 3.23. Nyquist plots of primary Zn-air batteries with FeNC-4000 and 20 wt% Pt/C obtained at constant voltage of 1.1 V.
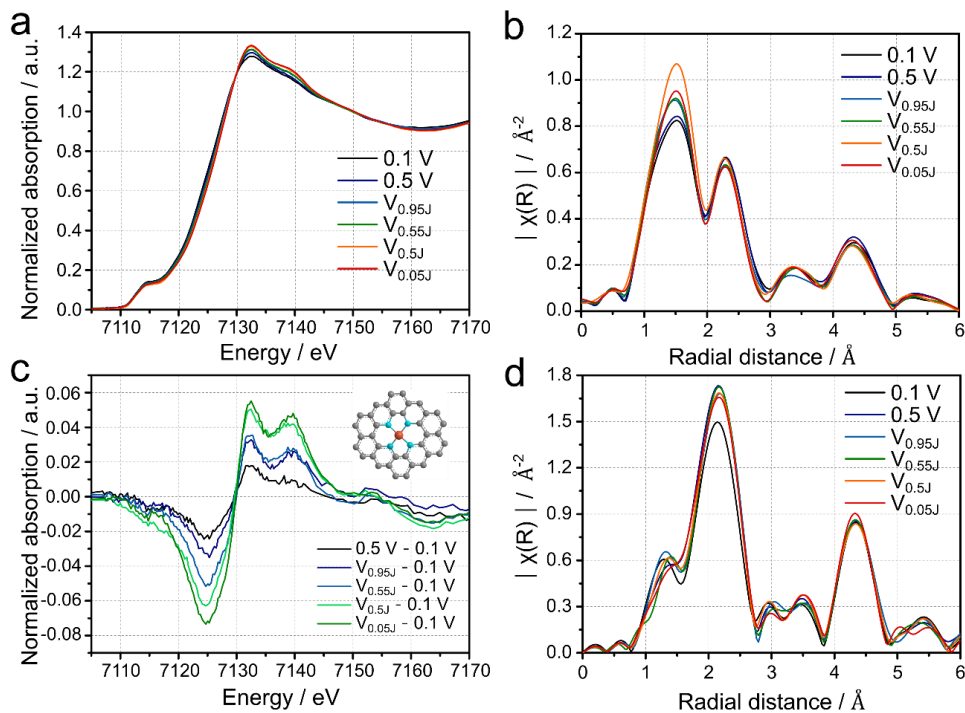
Figure 3.24. a) *in situ* XANE, b) corresponding FT-EXAFS, and c) △μ-XANES spectra of FeNC-4000. a) *in situ* FT-EXAFS spectra of FeNC-2000. (J : limiting current)

the applied voltage increases, which is indicative of $Fe^{2+/3+}$ redox reaction during ORR.[29] In the corresponding FT-EXAFS spectra (Figure 3.24b), the potential increase leads to the enhanced intensity of the peak for Fe-N bonding at 1.5 Å, which represents the oxygen adsorption on the $Fe-N_x$ site, that is, the existence of OH_{ad}-Fe-N_x bonding.[29,30] The peak for Fe-Fe bonding at 2.2 Å remains constant as the voltage increases suggesting that ORR on Fe@C does not change in the Fe-Fe bonding nature and hence that Fe element in Fe@C does not adsorb oxygen reactant, as reported[6]

As shown in Figure 3.24c, the surface-sensitive $\triangle\mu$ technique is employed to probe the oxygen adsorption onto the $Fe-N_x$ site without the influence of the Fe-Fe signal by subtracting the spectrum at 0.1 V from the spectrum at each voltage.[30] The $\triangle\mu$-XANES spectra from the experiment can be compared to the theoretical ones regarding their shape and energy position to deduce their structure.[31] The $\triangle\mu$-XANES spectra of FeNC-4000 accord with the previously reported Fe-N-C electrocatalysts with $Fe-N_4$ sites.[25, 32] It is also similar to the simulation with the theoretical model of $Fe-N_4-C_y$ (y=8,10), which proves that the $Fe-N_x$ moiety in FeNC-4000 consists of $Fe-N_4$ site.[25, 31] The relative OH_{ad} coverage calculated from dividing $\triangle\mu$ amplitude for the given voltage into $\triangle\mu$ amplitude for 0.1 V in the negative dip that indicates the charge transfer between metal and OH_{ad} (Figure 3.25).[32,33] The OH_{ad} coverage as a function of potential correlates with the ORR curve of FeNC-4000, which implies that the substantial amount of current density is originated from the $Fe-N_4$ site.

The change of the distance within Fe-N bonding (R_{Fe-N}) is detected during the potential increase, based on the shape and the location of the peak between FT-EXAFS spectra at 0.1 V and $V_{0.05J}$. The longer R_{Fe-N} at low potential and the shorter R_{Fe-N} at high potential represent the shifting of Fe from out-of-plane to in-plane through the potential increase. According to the recent findings, these Fe shifting
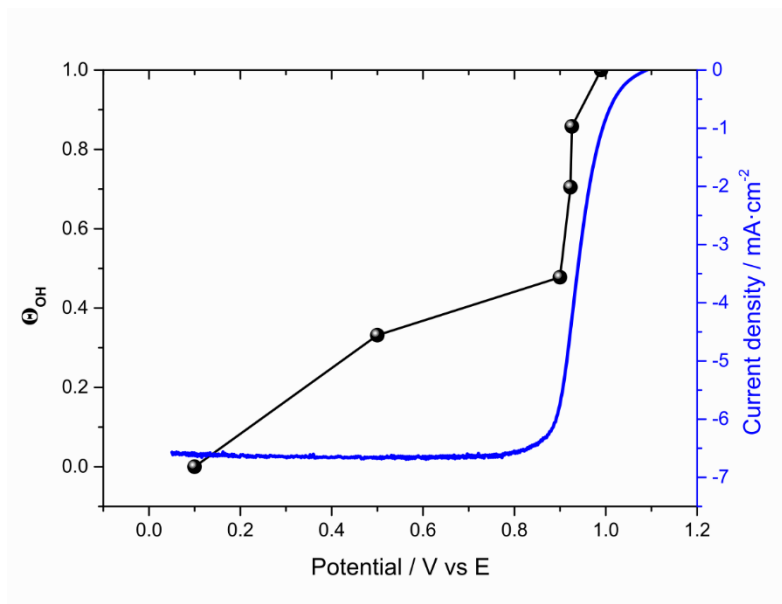
Figure 3.25. The oxygen coverage from △μ-XANES spectra and linear sweep voltammogram curves of FeNC-4000 in 0.1 M KOH.

phenomena with the potential change indicate that the Fe-N$_4$ site in FeNC-4000 corresponds to a distorted Fe-N$_4$ site designated as D1.[32] These Fe-N$_x$ sites promote the O$_2$ adsorption due to partially-filled d$_z{}^2$ electrons of Fe and lower Fe-O binding energy of in-plane O$_{ad}$-Fe-N$_4$ site at high potential, contrary to other typical Fe-N$_x$ sites, D2, that has fully-filled d$_z{}^2$ electrons of Fe and higher Fe-O binding energy of out-of-plane O$_{ad}$-Fe-N$_4$ site at high potential.[33] Moreover, the long R$_{Fe-N}$ increases the electron density of Fe due to the reduced Fe-to-N back-donation, which leads to the high turnover frequency of Fe-N$_4$.[34] The high turnover frequency and high Fe$^{2+/3+}$ redox potential from low Fe-O binding energy of the Fe-N$_4$ site lead to the excellent activity of FeNC-4000.

Contrary to those of FeNC-4000, *in situ* XAFS data of FeNC-2000 exhibit the different characterization regarding the movement of Fe while applying potential, as shown in Figure 3.24d. The intensity of peaks associated with both Fe-N and Fe-Fe bonding does not notably change despite the increase of potential. It indicates that Fe$^{2+/3+}$ redox reaction on the Fe-N$_4$ site rarely occurs, and FeNC-2000 primarily undergoes ORR on Fe@C, contrary to FeNC-4000.[6] The less density of the Fe-N$_x$ site results in the lower activity of FeNC-2000 compared to FeNC-4000 despite the more Fe content of FeNC-2000. Therefore, it is essential to regulate the formation of Fe@C until the efficient ORR on the Fe-N$_4$ site exhibits.

3.4. Conclusions

The Fe@C/Fe-N_x-controlled FeNC catalysts are synthesized by pyrosynthesis in a fast and large-scale method. In samples with low KB amount such as FeNC-600 and FeNC-2000, Fe@C and the excessive graphitized carbon is predominantly synthesized. On the other hand, samples with a high KB amount exhibit a high site density of Fe-N_x. Therefore, by controlling the weight ratio between the Fe-N complex and carbon, the amount and condition of Fe@C and Fe-N_x site are notably controlled. In the ORR activities of FeNCs, FeNC-4000 exhibits extremely high activity, including a half-wave potential of 0.941 V and the kinetic current density at 0.85 V of 358 mA·cm^{-2}. The excellent ORR activity of FeNC-4000 is ascribed to the synergetic effect of the small particle size and thin carbon layer of Fe@C and a high amount of Fe-N_x sites. As the cathode materials for AEMFCs and Zn-air batteries, FeNC-4000 exhibits excellent performance, such as the maximum power density of 526 mW·cm^{-2} and 231 mW·cm^{-2}, better than commercial platinum catalysts and the previously reported non-precious metal catalysts. In *in situ* XAFS analysis, FeNC-4000 shows the structural change of Fe bonded with N due to the oxygen adsorption, which indicates the catalytic-active Fe-N_4 site in FeNC-4000.

3.5. References

1. A. A. Gewirth, J. A. Varnell and A. M. DiAscro, Nonprecious Metal Catalysts for Oxygen Reduction in Heterogeneous Aqueous Systems, *Chem Rev* 2018, **118**, 2313-2339.

2. U. Martinez, S. Komini Babu, E. F. Holby, H. T. Chung, X. Yin and P. Zelenay, Progress in the Development of Fe-Based PGM-Free Electrocatalysts for the Oxygen Reduction Reaction, *Adv Mater* 2019, **31**, e1806545.

3. D. Zhao, Z. Zhuang, X. Cao, C. Zhang, Q. Peng, C. Chen and Y. Li, Atomic site electrocatalysts for water splitting, oxygen reduction and selective oxidation, *Chem Soc Rev* 2020.

4. S. H. Lee, J. Kim, D. Y. Chung, J. M. Yoo, H. S. Lee, M. J. Kim, B. S. Mun, S. G. Kwon, Y. E. Sung and T. Hyeon, Design Principle of Fe-N-C Electrocatalysts: How to Optimize Multimodal Porous Structures?, *J Am Chem Soc* 2019, **141**, 2035-2045.

5. S. J. Kim, J. Mahmood, C. Kim, G. F. Han, S. W. Kim, S. M. Jung, G. Zhu, J. J. De Yoreo, G. Kim and J. B. Baek, Defect-Free Encapsulation of Fe(0) in 2D Fused Organic Networks as a Durable Oxygen Reduction Electrocatalyst, *J Am Chem Soc* 2018, **140**, 1737-1742.

6. K. Strickland, E. Miner, Q. Jia, U. Tylus, N. Ramaswamy, W. Liang, M. T. Sougrati, F. Jaouen and S. Mukerjee, Highly active oxygen reduction non-platinum group metal electrocatalyst without direct metal-nitrogen coordination, *Nat Commun* 2015, **6**, 7343.

7. W. J. Jiang, L. Gu, L. Li, Y. Zhang, X. Zhang, L. J. Zhang, J. Q. Wang, J. S. Hu, Z. Wei and L. J. Wan, Understanding the High Activity of Fe-N-C

Electrocatalysts in Oxygen Reduction: Fe/Fe3C Nanoparticles Boost the Activity of Fe-N(x), *J Am Chem Soc* 2016, **138**, 3570-3578.

8. J. H. Kim, Y. J. Sa, H. Y. Jeong and S. H. Joo, Roles of Fe-Nx and Fe-Fe3C@C Species in Fe-N/C Electrocatalysts for Oxygen Reduction Reaction, *ACS Appl Mater Interfaces* 2017, **9**, 9567-9575.

9. J. Gim, V. Mathew, J. Lim, J. Song, S. Baek, J. Kang, D. Ahn, S. J. Song, H. Yoon and J. Kim, Pyro-synthesis of functional nanocrystals, *Sci Rep* 2012, **2**, 946.

10. D. Malko, A. Kucernak and T. Lopes, In situ electrochemical quantification of active sites in Fe-N/C non-precious metal catalysts, *Nat Commun* 2016, **7**, 13285.

11. I. K. Herrmann, R. N. Grass, D. Mazunin and W. J. Stark, Synthesis and Covalent Surface Functionalization of Nonoxidic Iron Core−Shell Nanomagnets, *Chemistry of Materials* 2009, **21**, 3275-3281.

12. T.-C. Lin, G. Seshadri and J. A. Kelber, A consistent method for quantitative XPS peak analysis of thin oxide films on clean polycrystalline iron surfaces, *Applied Surface Science* 1997, **119**, 83-92.

13. J. Park, J. Joo, S. G. Kwon, Y. Jang and T. Hyeon, Synthesis of monodisperse spherical nanocrystals, *Angew Chem Int Ed Engl* 2007, **46**, 4630-4660.

14. K. Artyushkova, B. Kiefer, B. Halevi, A. Knop-Gericke, R. Schlogl and P. Atanassov, Density functional theory calculations of XPS binding energy shift for nitrogen-containing graphene-like structures, *Chem Commun (Camb)* 2013, **49**, 2539-2541.

15.   H. Zhang, S. Hwang, M. Wang, Z. Feng, S. Karakalos, L. Luo, Z. Qiao, X. Xie, C. Wang, D. Su, Y. Shao and G. Wu, Single Atomic Iron Catalysts for Oxygen Reduction in Acidic Media: Particle Size Control and Thermal Activation, *J Am Chem Soc* 2017, **139**, 14143-14149.

16.   A. Sakamoto, STUDY OF FURNACE ATMOSPHERE FOR VACUUM-INERT GAS PARTIAL-PRESSURE BRAZING, *Welding Journal* 1991, **70**, S311-S320.

17.   H. Goesmann and C. Feldmann, Nanoparticulate functional materials, *Angew Chem Int Ed Engl* 2010, **49**, 1362-1395.

18.   H. T. Chung, D. A. Cullen, D. Higgins, B. T. Sneed, E. F. Holby, K. L. More and P. Zelenay, Direct atomic-level insight into the active sites of a high-performance PGM-free ORR catalyst, *Science* 2017, **357**, 479-484.

19.   J. Meng, S. Li and J. Niu, Crystallite Structure Characteristics and Its Influence on Methane Adsorption for Different Rank Coals, *ACS Omega* 2019, **4**, 20762-20772.

20.   F. Ding, A. Rosén, E. E. B. Campbell, L. K. L. Falk and K. Bolton, Graphitic Encapsulation of Catalyst Particles in Carbon Nanotube Production, *The Journal of Physical Chemistry B* 2006, **110**, 7666-7670.

21.   J. Deng, L. Yu, D. Deng, X. Chen, F. Yang and X. Bao, Highly active reduction of oxygen on a FeCo alloy catalyst encapsulated in pod-like carbon nanotubes with fewer walls, *Journal of Materials Chemistry A* 2013, **1**, 14868.

22.   A. Sadezky, H. Muckenhuber, H. Grothe, R. Niessner and U. Pöschl, Raman microspectroscopy of soot and related carbonaceous materials: Spectral analysis and structural information, *Carbon* 2005, **43**, 1731-1742.

23. X. Chen, J. Xiao, J. Wang, D. Deng, Y. Hu, J. Zhou, L. Yu, T. Heine, X. Pan and X. Bao, Visualizing electronic interactions between iron and carbon by X-ray chemical imaging and spectroscopy, *Chem Sci* 2015, **6**, 3262-3267.

24. N. M. Santhosh, G. Filipič, E. Kovacevic, A. Jagodar, J. Berndt, T. Strunskus, H. Kondo, M. Hori, E. Tatarova and U. Cvelbar, N-Graphene Nanowalls via Plasma Nitrogen Incorporation and Substitution: The Experimental Evidence, *Nano-Micro Letters* 2020, **12**.

25. Q. Jia, N. Ramaswamy, U. Tylus, K. Strickland, J. Li, A. Serov, K. Artyushkova, P. Atanassov, J. Anibal, C. Gumeci, S. C. Barton, M.-T. Sougrati, F. Jaouen, B. Halevi and S. Mukerjee, Spectroscopic insights into the nature of active sites in iron–nitrogen–carbon electrocatalysts for oxygen reduction in acid, *Nano Energy* 2016, **29**, 65-82.

26. A. Zitolo, V. Goellner, V. Armel, M. T. Sougrati, T. Mineva, L. Stievano, E. Fonda and F. Jaouen, Identification of catalytic sites for oxygen reduction in iron- and nitrogen-doped graphene materials, *Nat Mater* 2015, **14**, 937-942.

27. C. H. Choi, W. S. Choi, O. Kasian, A. K. Mechler, M. T. Sougrati, S. Bruller, K. Strickland, Q. Jia, S. Mukerjee, K. J. J. Mayrhofer and F. Jaouen, Unraveling the Nature of Sites Active toward Hydrogen Peroxide Reduction in Fe-N-C Catalysts, *Angew Chem Int Ed Engl* 2017, **56**, 8809-8812.

28. X. Wan, X. Liu, Y. Li, R. Yu, L. Zheng, W. Yan, H. Wang, M. Xu and J. Shui, Fe–N–C electrocatalyst with dense active sites and efficient mass transport for high-performance proton exchange membrane fuel cells, *Nature Catalysis* 2019, **2**, 259-268.

29.   M. Xiao, J. Zhu, L. Ma, Z. Jin, J. Ge, X. Deng, Y. Hou, Q. He, J. Li, Q. Jia, S. Mukerjee, R. Yang, Z. Jiang, D. Su, C. Liu and W. Xing, Microporous Framework Induced Synthesis of Single-Atom Dispersed Fe-N-C Acidic ORR Catalyst and Its in Situ Reduced Fe-N4 Active Site Identification Revealed by X-ray Absorption Spectroscopy, *ACS Catalysis* 2018, **8**, 2824-2832.

30.   U. Tylus, Q. Jia, K. Strickland, N. Ramaswamy, A. Serov, P. Atanassov and S. Mukerjee, Elucidating Oxygen Reduction Active Sites in Pyrolyzed Metal-Nitrogen Coordinated Non-Precious-Metal Electrocatalyst Systems, *J Phys Chem C Nanomater Interfaces* 2014, **118**, 8999-9008.

31.   N. Ramaswamy, U. Tylus, Q. Jia and S. Mukerjee, Activity descriptor identification for oxygen reduction on nonprecious electrocatalysts: linking surface science to coordination chemistry, *J Am Chem Soc* 2013, **135**, 15443-15449.

32.   J. Li, S. Ghoshal, W. Liang, M.-T. Sougrati, F. Jaouen, B. Halevi, S. McKinney, G. McCool, C. Ma, X. Yuan, Z.-F. Ma, S. Mukerjee and Q. Jia, Structural and mechanistic basis for the high activity of Fe–N–C catalysts toward oxygen reduction, *Energy & Environmental Science* 2016, **9**, 2418-2432.

33.   Q. Jia, N. Ramaswamy, H. Hafiz, U. Tylus, K. Strickland, G. Wu, B. Barbiellini, A. Bansil, E. F. Holby, P. Zelenay and S. Mukerjee, Experimental Observation of Redox-Induced Fe–N Switching Behavior as a Determinant Role for Oxygen Reduction Activity, *ACS Nano* 2015, **9**, 12496-12505.

34.   C. Fierro, A. B. Anderson and D. A. Scherson, Electron donor-acceptor properties of porphyrins, phthalocyanines, and related ring chelates: a

molecular orbital approach, *The Journal of Physical Chemistry* 1988, **92**, 6902-6907.

국문초록

    과도한 화석 연료의 사용으로 배출되는 이산화탄소를 제한하는 현 상황에 발맞춰 연료 전지 및 금속 공기 전지를 포함한 청정 에너지 장치의 개발이 장려되고 있다. 전기 화학적 산소 환원 반응 (ORR)은 여러 친환경 에너지 변환 및 저장 시스템에서 가장 중요한 반응이다. 그러나, 이 ORR 반응이 매우 느리기 때문에 이를 해결하기 위해서 Pt 와 같은 귀금속 촉매를 사용하게 되는데, 이는 높은 비용, 희소성 및 낮은 지속성으로 인해 바람직하지 않다. 따라서, 고성능을 나타내면서도 보다 경제적인 대안 촉매를 개발하기 위해 상당한 양의 연구가 진행되어왔다. 비 귀금속 촉매는 장치로의 적용 가능성 및 높은 지속 가능성으로 인해 큰 관심을 끌었다. 비 귀금속 기반 촉매의 급속한 발전에도 불구하고 반쪽 전지와 단일 전지의 성능 간 격차는 거의 좁아지지 않았으며, 이는 에너지 장치의 대량 생산에 중요한 문제 중에 하나이다. 따라서, 본 연구는 반쪽-전지 및 단일-전지 작업 모두에서 효율적인 비-귀금속 촉매를 설계하고 합성하기 위해 진행되었다.

    1 장에서는 산소환원반응과 산소환원반응을 위한 비-귀금속 촉매에 대해 소개한다. 음이온 교환 막 연료 전지와 아연-공기 전지에 관련된 전기화학반응과 각 장치의 장단점에 대해 다루었다.

    2 장에는 기공 구조가 조절된 황과 질소가 이중 도핑 된 탄소 (SNBC)가 대나무 및 티오우레아 (thiourea)의 열분해를 통해 ORR 전기 촉매로서 제조된다. SNBC 는 메소포어 (mesopore) 비율과 효과적인 활성점의 증가로 인해 상용 Pt/C 와 비교할 때 탁월한 반파 전위 및 안정성을 나타낸다. 음이온 교환 막 연료 전지와 아연-공기 전지를 위한 양극 물질로서, SNBC 는 충분한 2 차 기공 구조를 바탕으로 기존에 보고된 탄소 기반 촉매보다 우수한 단일 전지 성능을 나타낸다. 이

연구는 바이오 매스 기반 촉매를 실제 에너지 장치에 적용할 수 있음을 보여주는데 의의가 있다.

3 장에서는 초급속연소법(pyro-synthesis)을 사용하여 철과 탄소의 비율을 조절하여 탄소 층으로 코팅된 철 나노입자 (Fe@C) 및 Fe-N$_x$ 를 갖는 철-질소-탄소 전기 촉매를 제조하였다. 탄소 함량을 증가시키면 Fe-N$_x$ 의 밀도가 증가하고 철 나노 입자의 크기 및 탄소 코팅층의 두께가 감소하여 ORR 활성이 향상된다. 또한, Fe@C 는 4-전자 ORR 을 진행할 뿐 만 아니라 중간체의 안정화 및 환원을 진행시켜 ORR 을 촉진시킨다. 따라서, Fe@C/Fe-N$_x$ 비율을 조절하면 우수한 ORR 활성을 나타내는 최적점을 얻을 수 있다. 음이온 교환 막 연료 전지와 아연-공기 전지의 양극 물질로서, FeNC 촉매는 백금 촉매 및 이전에 보고된 전이 금속 기반 촉매와 비교할 때 우수한 성능을 나타낸다. 촉매의 Fe-N$_x$ 는 실시간 XAFS 분석을 이용하여 높은 ORR 성능을 타내는 Fe-N$_4$ 구조인 것으로 입증되었다.

주요어: 산소환원반응, 전기화학촉매, 비-귀금속 촉매, 음이온 교환 막 연료전지, 아연-공기 전지.

학번: 2014-21584

List of publications (SCI)

1st or co-1st author

1. Ji Eun Park[†], <u>Mi-Ju Kim</u>[†], Myung Su Lim, Sun Young Kang, Jong Kwan Kim, Seung-Hyeon Oh, Min Her, Yong-Hun Cho, Yung-Eun Sung, Graphitic carbon nitride-carbon nanofiber as oxygen catalyst in anion-exchange membrane water electrolyzer and rechargeable metal-air cells, *Applied Catalysis B: Environmental* 2018, **237**, 140-148.

2. Aihua Jin[†], <u>Mi-Ju Kim</u>[†], Kug-Seung Lee, Seung-Ho Yu, Yung-Eun Sung, "Spindle-like Fe_7S_8/N-doped carbon nanohybrids for high-performance sodium ion battery anodes" *Nano Research* 2019, **12**, 695-700.

3. <u>Mi-Ju Kim</u>[†], Ji Eun Park[†], Sungjun Kim, Myung Su Lim, Aihua Jin, Ok-Hee Kim, Min Jeong Kim, Kug-Seung Lee, Jinsoo Kim, Seung-Soo Kim, Yong-Hun Cho, Yung-Eun Sung, Biomass-derived air cathode materials: Pore-controlled S, N-co-doped carbon for fuel cells and metal-air batteries, *ACS Catalysis* 2019, **9**, 3389-3398.

Co-author

1. Yun Sik Kang, Kwang-Hyun Choi, Docheon Ahn, Myeong Jae Lee, Jaeyoon Baik, Dong Young Chung, <u>Mi-Ju Kim</u>, Stanfield Youngwon Lee, Minhyoung Kim, Heejong Shin, Kug-Seung Lee, Yung-Eun Sung, Effect of post heat-treatment of composition-controlled PdFe nanoparticles for oxygen reduction reaction, *Journal of Power Sources* 2016, **303**, 234-242.

2. Myeong Jae Lee, Jin Soo Kang, Yun Sik Kang, Dong Young Chung, Heejong Shin, Chi-Yeong Ahn, Subin Park, <u>Mi-Ju Kim</u>, Sungjun Kim, Kug-Seung Lee, Yung-Eun Sung, Understanding the Bifunctional Effect for Removal of CO Poisoning: Blend of a Platinum Nanocatalyst and Hydrous Ruthenium Oxide as a Model System, *ACS Catalysis* 2016, **6**, 2398-2407.

3. Stanfield Youngwon Lee, Dong Young Chung, Myeong Jae Lee, Yun Sik Kang, Heejong Shin, <u>Mi-Ju Kim</u>, Christopher W. Bielawski, Yung-Eun Sung, Charting the Outer Helmholtz Plane and the Role of Nitrogen Doping in the Oxygen Reduction Reaction Conducted in Alkaline Media Using Nonprecious Metal Catalysts, *The Journal of Physical Chemistry C* 2016, **120**, 24511-24520.

4. Yun Sik Kang, Sung Jong Yoo, Myeong Jae Lee, <u>Mi-Ju Kim</u>, Stanfield Youngwon Lee, Kug-Seung Lee, Yung-Eun Sung, Facile synthesis of platinum alloy electrocatalyst via aluminum reducing agent and the effect of post heat treatment for oxygen reduction reaction, *International Journal of Hydrogen Energy* 2016, **41**, 22952-22962.

5. Dong Young Chung, Myeong Jae Lee, Minhyoung Kim, Heejong Shin, <u>Mi-Ju Kim</u>, Ji Mun Yoo, Subin Park, Yung-Eun Sung, CO electro-oxidation reaction on Pt

nanoparticles: Understanding peak multiplicity through thiol derivative molecule adsorption, *Catalysis Today* 2017, **293-294**, 2-7.

6. Ji Eun Park, Sungjun Kim, Ok-Hee Kim, Chi-Yeong Ahn, <u>Mi-Ju Kim</u>, Sun Young Kang, Tae Il Jeon, Jae-Goo Shim, Dong Woog Lee, Ji Hyun Lee, Yong-Hun Cho, Yung-Eun Sung, Ultra-low loading of IrO_2 with an inverse-opal structure in polymer-exchange membrane water electrolysis, *Nano Energy* 2019, **58**, 158-166.

7. Aihua Jin, Seung-Ho Yu, Jae-Hyuk Park, Seok Mun Kang, <u>Mi-Ju Kim</u>, Tae-Yeol Jeon, Junyoung Mun, Yung-Eun Sung, Iron sulfides with dopamine-derived carbon coating as superior performance anodes for sodium-ion batteries, *Nano Research* 2019, **12**, 2609-2613.